博士論文

Study on the cavity optomagnonics
（共振器オプトマグノニクスの研究）

長田　有登

Dissertation

Study on the Cavity Optomagnonics

Supervisor: Associate Prof. Koji Usami

Department of Applied Physics
School of Engineering
The University of Tokyo
37-147084   Alto OSADA

Submitted in February, 2017

ABSTRACT

Enhancement of interaction between light and matter has been intensely studied using optical cavities, in which the light field is build up more than thousands of times. For example, an atom inside a microwave or optical Fabry-Perot resonator is controlled by the cavity photons in a quantum regime, which flourished as a cavity quantum electrodynamics [1, 2]. By using a solid-state artificial atom, the dispersive readout of a quantum bit can be implemented using a resonator [3]. High-quality optical resonators have also enabled researchers to manipulate mechanical motions of an object involved in them, which is the activity called the cavity optomechanics [4]. These have enabled coherent control over internal states of atoms and vibration quanta of mechanical oscillator, leading to the realization of material-based quantum information and communication technologies. Here we introduce another object, macroscopic spin excitation or magnon, as an object to be optically controlled. Since the realization of the strong coupling between a superconducting qubit and a uniform magnon [5], the optical control of the magnon is also of certain interest in the scope of the construction of the quantum network.

In general, the interaction between light and magnon in a material is weak due to the fact that the interaction is mediated by the spin-orbit interaction of electrons in a material. Therefore, the relatively strong electromagnetic field is required to observe the interaction. For instance, the magnon-induced Brillouin scattering has been studied using ultrashort, intense optical pulses [6, 7]. As an alternative way to enhance the magnon-light interaction, we propose to use an optical cavity. In particular, optical whispering gallery modes (WGMs) hosted in an axially symmetric sample is used, which have favorable features of a high quality factor and a small mode

volume. Study on the Brillouin scattering of light in the WGMs by magnons, which we call cavity optomagnonics, is a new system involving light and magnon, and will serve as a new platform for chiral photonics, opto-spintronics and opto-magnonics.

We implement such a system by a sphere made of single-crystal yttrium iron garnet (YIG) which is a ferrimagnetic insulator transparent for 1.5 μm-wavelength light. The magnetostatic modes in a YIG sphere, the Walker modes, are well known as being long-lived. On the other hand, the WGMs in a ferromagnetic sphere have not been observed. The WGMs in a YIG sphere with diameter of around 1 mm are for the first time observed in this study. The Brillouin scattering of WGM light by the uniform magnon mode, the Kittel mode, is revealed to show rich behaviors such as the Stokes/anti-Stokes scattering asymmetry and the nonreciprocity. These behaviors are explained by the unique polarization property of WGMs. The Brillouin scattering is further investigated by varying the applied magnetic field, where we found the strong modification of the scattering strength owing to the densities of states of the WGMs. The Brillouin scatterings by the general, non-uniform Walker modes are also observed, and show nontrivial behavior due to the coupling among other Walker modes. A theoretical treatment of the Brillouin scatterings involving WGMs and some families of the Walker modes is developed and compared with the experiments. We find that in the cavity optomagnonics, the spin and orbital angular momentum conservation are the key features.

We now elaborate on the details of the research mentioned above. First, the WGMs in a YIG sphere are investigated. The experimental apparatuses for coupling light into WGMs in a YIG sphere via a tapered optical nanofiber, as well as a silicon prism are designed and constructed. The former shows a large coupling but also some difficulty in determining the polarization coupled to WGM. The latter is inferior in terms of the coupling to WGMs, however, the ambiguity of the coupled polarization is removed. The observed spectra for two different polarizations exhibit the intrinsic frequency shift due to the geometrical birefringence. The observed frequency shift and the free spectral range are in agreement with the theoretical prediction. In addition, from the theoretical perspective, we analyze the polarization of WGMs which depends on the position and the circulation direction. Orbital angular momenta of the WGMs are also considered, which, together with the polarization properties, are revealed to

be crucial in studying the Brillouin scattering.

Next, we examine the Walker modes in a YIG sphere by sending microwaves to a loop coil near the sphere and measure the reflected power. Walker-mode frequencies depending on the static magnetic field strength are observed for the cases of the relatively homogeneous and inhomogeneous magnetic fields applied respectively by cylindrical and ring-shaped magnets. It is found that even in the case of the inhomogeneous magnetic field with ring-shaped magnets, several observed Walker modes can be identified in comparison to the case of the homogeneous field produced by the cylindrical magnets. For the analysis of the Brillouin scattering, the orbital angular momenta of Walker modes, which is to be conserved together with those of WGMs, are important but have not explicitly given so far. We extracted them from the well-known expressions of the transverse magnetization distributions of the Walker modes.

We then study the Brillouin scattering of WGMs by Walker mode. We first focus on the Kittel mode, the uniform magnon mode which does not possess orbital angular momentum. In the Brillouin scattering of WGM by the Kittel mode, the pronounced nonreciprocity and the Stokes/anti-Stokes scattering asymmetry are observed and interpreted in terms of the spin and orbital angular momentum conservation. The variation of the scattering strength is observed by changing the Kittel-mode frequency using an electromagnetic coil and the maximum is found when the density of states of the WGM fully supports the scattered light.

With these series of experiments, a theory of the Brillouin scattering of light in WGMs by Walker modes including the Kittel mode is constructed. According to the theoretical framework, the general, non-uniform Walker modes show different behavior in the scattering process. The differences arise from the finite orbital angular momentum of the Walker mode. We attempt to experimentally observe the difference, but in general, the observed behavior does not simply agree with the theory. This is probably due to the coupling among various Walker modes. For a specific Walker mode, the nonreciprocal nature of the Brillouin scattering is present but significantly different from the one by the Kittel mode. This is, however, qualitatively consistent with the theory we developed.

In conclusion, we investigated the system of cavity optomagnonics, where the

Brillouin scattering interconnects the WGMs and Walker modes hosted inside a YIG sphere. We developed a theory of the Brillouin scattering involving WGMs and Walker modes, which imposes spin and orbital angular momentum conservation on the system. For the Kittel mode, the nonreciprocity, the Stokes/anti-Stokes asymmetry and the scattering strength depending on the magnetic field were observed as consequences of the angular momentum conservation and the presence of the optical WGM resonances. For higher-order Walker modes, the coupling among Walker modes makes the behavior so rich that the theory cannot be simply applied, whereas the mode seemingly not so much affected by others shows qualitatively consistent behavior with the theory. For the latter, the orbital angular momentum conservation is observed.

Brillouin scattering by the higher-order Walker modes will be further investigated aiming at enhancing the Brillouin scattering of light in WGMs. Among other modes the surface spin wave modes are expected to have stronger light-magnon interaction due to smaller mode volume, which may lead to the quantum-level, optical control of the magnon. The optical resonator and the ferromagnetic magnon are new for spintronics and quantum optics community, respectively. Our work will be a nexus between quantum optics and spintronics and open up a new testbed for the research such as the chiral photonics, opto-spintronics and optomagnonics.

Contents

Chapter 1

Introduction

1.1 Light and magnetisms: from Faraday effect to optomagnonics

In the middle of 19th century, the age that light had not been recognized as being electromagnetic wave, Faraday discovered the rotation of the polarization of light passing through the magnetized medium and the angle of rotation gets large as the applied magnetic field increases. This celebrated Faraday effect was one of the earliest smoking gun implying the fact that light is an electromagnetic phenomenon, which was later suggested by Maxwell. Faraday effect is revealed to be a member of the magneto-optical effect where the optical linear or circular birefringence takes place in the transmission or reflection from a magnetized sample. Practical applications of the magneto-optical effects take place in the late 20th, in the forms of optical isolators, MO disks and magneto-optical microscopes.

Today, the research involving light and magnetism still offers an active field in condensed matter physics. The matured experimental techniques of producing ultrashort, intense optical pulses has become one of the mightiest tool for the investigation of the fast dynamics of electronic states in a material. It also enables researchers to temporally resolve the dynamics of the magnetization in ferro- or antiferromagnetic materials. Along this line, researchers realized the observation of the time evolution of the ferromagnetic magnons [6]. Creation and annihilation of the antiferromagnetic magnons are also shown to be feasible using properly chosen optical polarizations [7].

These are referred to as the "optomagnonics". In the Ref. [9], the quasi-equilibrium Bose-Einstein condensate of magnons are created by microwaves and observed by the Brillouin light scattering. In spintronics, where information is carried by joule-heating-free spin current, it is known that the spin current and the ferromagnetic magnon can be transformed from one to another. Regarding this, the development of the optomagnonics makes well-developed optical techniques added in for the manipulation of the spin degree of freedom.

Despite these efforts, optomagnonics suffers from the weak interaction between light and magnon, which arises from the fact that the interaction is mediated by the spin-orbit coupling of electrons in a material. One of the possible solutions is the use of an optical resonator, where light field is built up in a confined region. In the next Section we review the light-matter interaction in an optical resonator.

1.2 Object in a resonator: from atoms to mechanical oscillators

Most of the studies mentioned in the previous Section relies on the presence of laser. The invention of laser [11, 12] is indeed based on the technique of surrounding a gain medium by an optical resonator or an optical cavity, in which the light field is built up and interacts with the gain medium. Enhancement of light-matter interaction by the use of an optical resonator already took place there. In the search for the strong nonlinear optical effects such as the second harmonic generation [13], fabrication of a resonator incorporating a nonlinear optical crystal has been successful. This can also be regarded as the early form of the system employing the cavity-enhancement of the light-matter interaction.

An extreme form of such a kind of attempt is the system of cavity quantum electrodynamics (QED) starting from the end of the 20th century, where atoms inside a resonator interact with the field in a strong coupling regime [1, 2]. This system boosted the investigation and control of an atom and a photon in the quantum regime and opened up the possibility of realizing the quantum computation. Driven by the success of the cavity QED experiments, some systems involving solid-state artificial atoms are studied such as the one with optical photons and a semiconductor quantum

dot. The strong coupling between an exciton in the quantum dot and a photon in a photonic crystal cavity was recently achieved [14]. The growth of the technology of a superconducting quantum bit operating with microwaves [15] is also remarkable. A system involving microwave photons and the superconducting quantum bit is called the circuit QED [16].

There have also been growing interest of extending the objects to control by the resonator. The target has been extended from atoms to macroscopic object, a vibration of a mechanical oscillator. The mechanical motions are either coupled to an optical or a microwave resonator, which are respectively referred to as cavity opto- and electromechanics [17]. These have been explored and the cooling the mechanical motion down to the ground state [18, 19] has been achieved.

In the research activities of the condensed matter science, however, optical resonators are not so much added in despite their potential abilities. As mentioned in the end of the previous Section, the weakness of the interaction between light and magnon is an issue; the issue that can be addressed by utilizing the optical resonator. This is our motivation to investigate *cavity optomagnonics*, where light-magnon interaction is enhanced with an optical cavity.

1.3 Cavity optomagnonics using a ferromagnetic sphere

Here we describe the detailed implementation of the system of cavity optomagnonics and expected behavior of the system under consideration, and briefly summarize the achievements of this dissertation. For the implementation of cavity optomagnonics, two things must be specified: material and geometry of a sample, and what kind of optical resonator we use. The material we use is single crystal yttrium iron garnet (YIG, $Y_3Fe_5O_{12}$). This material is a ferromagnetic insulator and transparent for 1.5 μm-wavelength light, hence suitable for the investigation of the light-magnon interaction. The geometry of the sample is a sphere. One benefit of the spherical sample is that the frequencies and the spatial profiles of the magnetostatic modes can be obtained in analytical forms. Moreover, the magneto static modes in a sphere are known to be long-lived because the effect of demagnetization is cancelled. Another benefit is that the dielectric sphere has optical resonances in itself, called the whispering gallery modes (WGMs). This indeed answers the question of what kind of resonator we use.

Therefore, our system involved both the magnetostatic modes and the WGMs supported in a YIG sphere. When they interact, Brillouin scattering takes place by exchanging energy and angular momentum between them, while the total energy and total angular momentum are conserved. Note that the magnetostatic modes are the "macroscopic" spin excitations. Therefore, not only the spin angular momentum conservation but the orbital one is expected to restrict the relevant process of the Brillouin scattering. Neither of these two constraints exists in cavity optomechanical systems. These unique features of the cavity optomagnonical system may provide a new perspective in designing chiral photonics and opto-spintronic devices.

1.4   Contents of the dissertation

This Chapter has introduced some basic ideas related to the cavity optomagnonics. In the following Chapters we proceed to the observations of the fundamental and important features of the WGMs, the Walker modes and the Brillouin scattering of light in WGM by the Walker modes. Chapter 2 describes the basic properties of the WGMs. Theoretical descriptions are given first. The spin and orbital angular momenta of WGMs are analyzed in great detail. The experimental observation of the WGMs in a YIG sphere follows. The analysis of the orbital angular momentum and the experimental observation of the Walker modes are given in Chapter 3. In Chapter 4, the theoretical framework for the description of the Brillouin scattering of light in the WGMs by the Walker modes is developed. The observation of the Brillouin scattering by the Kittel mode and by the non-uniform Walker modes are reported in Chapters 5 and 6, respectively Chapter 7 concludes this dissertation and gives outlooks.

Chapter 2

Whispering gallery mode in a yttrium iron garnet sphere

In this Chapter, we analyze some properties of the whispering gallery modes (WGMs), especially for a dielectric sphere and a spheroid which have analytical solutions. In the most of previous experiments such as the optomechanics and the frequency-comb generation experiments the polarization properties of WGMs are not essential. As we shall see in Chapter 4, however, the polarization should be crucial when the inelastic scattering is triggered by the spin degree of freedom in the material. In order for this to be clear, the full vectorial treatment of the WGM is indispensable in our analyses. The latter half of this Chapter is devoted to the experimental observation of the WGMs in YIG spheres.

2.1 Full vectorial treatment of WGMs

2.1.1 Vector Helmholtz equation and analytical solutions

First of all, we review the full vectorial nature of the WGMs and then analyze their properties of the polarization states relevant for the configuration of with which the Brillouin scattering can be observed. The starting point is a vector Helmholtz equation

$$\Delta \boldsymbol{E} - \frac{\epsilon}{c^2} \frac{\partial^2}{\partial t^2} \boldsymbol{E} = \boldsymbol{0}, \tag{2.1}$$

where $\boldsymbol{E}$ is the electric field, ϵ the dielectric constant and c the speed of light. Here, for brevity, the dielectric constant in this equation only includes the scalar component,

since the tensor permittivity such as the optical activity is sufficiently small compared to it. The magnetic field $\boldsymbol{B}$ also satisfies this equation. Let us assume that the electric field possesses well-defined frequency ω. Then the electric field can be written as $\boldsymbol{E}(\boldsymbol{r}, t) = \boldsymbol{E}(\boldsymbol{r})e^{i\omega t}$ and the Eq. (2.1) reads $\Delta\boldsymbol{E} + k_n^2\boldsymbol{E} = \boldsymbol{0}$ with the wavevector defined by $k_n = \sqrt{\epsilon}\omega/c = n\omega/c$, where n represents the refractive index.

The vector solution $\boldsymbol{J}$ of the equation Eq. (2.1) is not easily obtained from the vector equation itself, and to make it easy, it is known to be good to introduce the source function ψ which gives $\boldsymbol{J}$ by the relation $\boldsymbol{J} = \nabla\times(\boldsymbol{c}\psi) = -\boldsymbol{c}\times\nabla\psi$ [20]. We can immediately see that ψ also satisfies the same type of equation as the one $\boldsymbol{J}$ obeys:

$$\Delta\psi + k_n^2\psi = 0. \tag{2.2}$$

Now the equation to be solved for deriving the vector solution has turned into a familiar problem of solving the scalar Helmholtz equation. Given one solution $\boldsymbol{J}$ of the vector equation[1], another independent solution can be obtained by $\boldsymbol{K} = (1/k)\nabla\times\boldsymbol{J}$. These solutions $\boldsymbol{J}$ and $\boldsymbol{K}$ form the basis of the vector solutions. These two basis vectors are interpreted as those for the electric and magnetic fields: when one corresponds to the electric field, the other to the magnetic field.

The solution of the scalar Helmholtz equation is well-known:

$$\psi = e^{im\phi}P_l^m(\cos\theta)z_l(kr) \tag{2.3}$$

where $P_l^m(x)$ is the associated Legendre function of the first kind and $z_l(x)$ represents the spherical Bessel function $j_l(x)$ inside and the spherical Hankel function $h_l^{(2)}(x)$ outside the sphere. Here appear two mode indices l and m. The mode's order l is approximately the optical length of the circumference divided by the wavelength, and modes with $l \gg 1$ is called the WGMs. The azimuthal index m ($-l \leq m \leq l$) is related to the number of field maxima along θ-direction. The fundamental WGM ($l = m$) has a single maximum and generally WGMs exhibit $l - m + 1$ maxima in θ-direction.

Since we have the solution of the scalar Helmholtz equation, the solutions $\boldsymbol{J}$ and

---

[1]It is known that as the constant vector $\boldsymbol{c}$, the position vector $\boldsymbol{r}$ is used for the solution in the spherical coordinates.
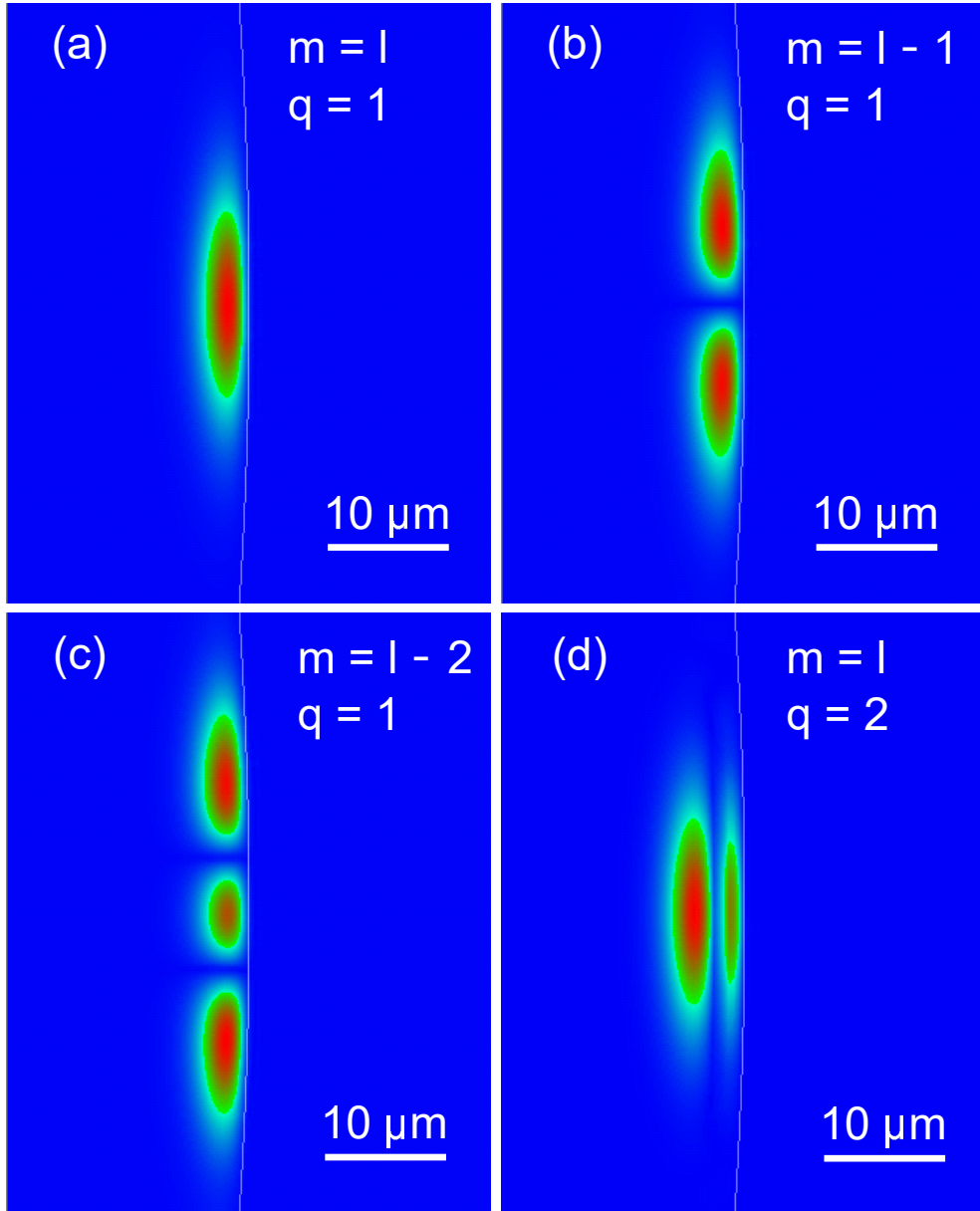
Figure 2.1: Cross-sectional profiles of the WGMs. Figures (a), (b) and (c) are those for the case $m = l$, $m = l-1$ and $m = l-2$, respectively with $q = 1$. Figure (d) shows the mode profile of the $l = m$ and $q = 2$ case. These mode profiles are calculated by the finite element method [21, 22]
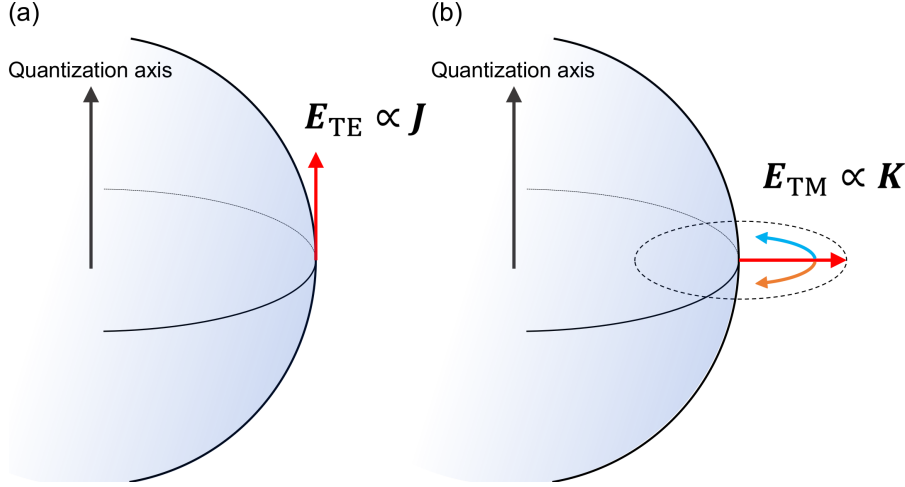
Figure 2.2: Schematic picture of the two independent polarizations (a) the TE and (b) the TM modes. The WGM light runs in the equatorial plane.

$\boldsymbol{K}$ for the vector Helmholtz equation can be calculated as

$$\boldsymbol{J}_{lm} = \frac{-m}{\sin\theta}e^{im\phi}P_l^m(\cos\theta)z_l(kr)\boldsymbol{e}_\theta + ie^{im\phi}\frac{dP_l^m(\cos\theta)}{d\theta}z_l(kr)\boldsymbol{e}_\phi \qquad (2.4)$$

$$\boldsymbol{K}_{lm} = \frac{z_l(kr)}{kr}e^{im\phi}\left[l(l+1)\right]P_l^m(\cos\theta)\boldsymbol{e}_r,$$
$$+ e^{im\phi}\frac{dP_l^m(\cos\theta)}{d\theta}\frac{1}{kr}\frac{d[krz_l(kr)]}{d(kr)}\boldsymbol{e}_\theta + ime^{im\phi}\frac{P_l^m(\cos\theta)}{\sin\theta}\frac{1}{kr}\frac{d[krz_l(kr)]}{d(kr)}\boldsymbol{e}_\phi,$$
$$(2.5)$$

using Eq. (2.3). Here the $\boldsymbol{e}_r$, $\boldsymbol{e}_\theta$ and $\boldsymbol{e}_\phi$ are the basis vectors of spherical coordinates. In Figs. 2.1(a), (b) and (c) the cross-sections of the WGMs in $r\theta$-plane for a few modes are shown. These mode profiles are calculated by the finite element method [21, 22]. As can be seen from above, $\boldsymbol{J}$ is always perpendicular to the vector $\boldsymbol{r}$. Thus $\boldsymbol{J}$ is identified as being proportional to the electric field of the transverse electric (TE) mode while $\boldsymbol{K}$ to that of the transverse magnetic (TM) mode.

Let us focus on the r- and ϕ-components of the fields expressed by Eqs. (2.4) and (2.5), and consider the polarization of the TE and the TM modes with the quantization axis perpendicular to the plane of the WGM orbit (see Fig. 2.2). First, the TE mode proportional to Eq. (2.4) has its polarization mostly in the direction of the quantization axis, from which we conclude that the TE mode can be considered as being π polarized. On the other hand, the TM mode, which can be expressed by Eq. (2.5),

has more complicated nature. We limit the consideration on the fundamental WGM here and the case

$$\frac{\mathrm{d}[krz_l(kr)]}{\mathrm{d}(kr)} > 0,\tag{2.6}$$

which will be discussed later in Secs. 2.2 and 4.2 together with the opposite sign of the left-hand-side. The key point is the factor im in the third term. The factor $i = e^{i(\pi/2)}$ tells us that the electric field rotates in the plane of the WGM orbit. Furthermore, the factor m equals to $+l$ for the clockwise (CW) and $-l$ for the counter-clockwise (CCW) WGM, so that the circulation direction of CW or CCW directly corresponds to the σ^- or σ^+ polarization.

2.1.2 Characteristic equations and asymptotic solutions

Indeed, in addition to the mode indices l and m, one more mode index q labels WGMs, which emerges from the boundary conditions, or the characteristic equations

$$\chi\frac{\mathrm{d}[\rho j_l(\rho)]/\mathrm{d}\rho}{j_l(\rho)} = \frac{\mathrm{d}[\rho h_l^{(2)}(\rho)]/\mathrm{d}\rho}{h_l^{(2)}(\rho)}.\tag{2.7}$$

Here χ is 1 for the TE and $1/n^2$ for the TM mode, and $\rho = k_0 r$ with the wavevector in a vacuum k_0. According to the asymptotic expansion in the large-resonator-diameter limit [23, 24, 25], the frequencies of WGMs in ellipsoidal resonators are given by the following relation:

$$nka = l - \alpha_q\left(\frac{l}{2}\right)^{\frac{1}{3}} + \frac{2p(a-b)}{2b} - \frac{\chi n}{\sqrt{n^2-1}} + \frac{3\alpha_q^2}{20}\left(\frac{l}{2}\right)^{-\frac{1}{3}}$$
$$- \frac{\alpha_q}{12}\left[\frac{2p(a^3-b^3)+a^3}{b^3} + \frac{2n\chi(2\chi^2-3n^2)}{(n^2-1)^{3/2}}\right]\left(\frac{l}{2}\right)^{-\frac{2}{3}} + \mathcal{O}\left(\frac{1}{l}\right)\tag{2.8}$$

where a and b are the major and minor radii of the ellipsoid, $p = l - |m|$, α_q are the negative zeros of Airy function of order q, and q is the positive integer which labels the WGM together with l and m and equal to the number of field maxima in the radial direction. The WGM of $l = m$ and $q = 2$ is shown in Fig. 2.1(d). The resonant frequencies calculated from the asymptotic expression (2.8) are shown in the Fig. 2.3.

Geometrical birefringence

The characteristic equation (2.7) is, as it is, different for the TE and the TM modes. This means that these two have neither the same effective refractive index, nor the
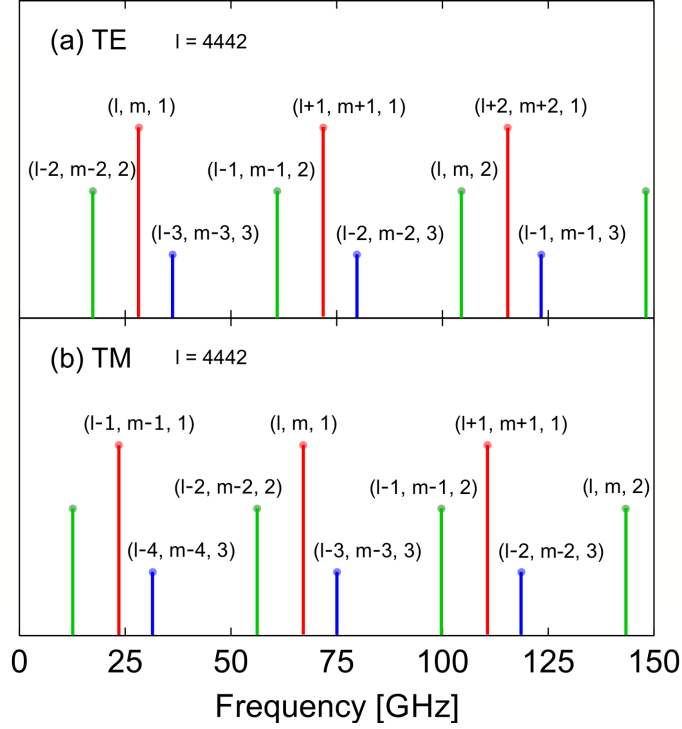
Figure 2.3: Calculated positions of the WGM resonances for modes (l, m, q) up to $q = 3$. Sphere diameter of 1000 μm, and the refractive index of $n_r = 2.19$ are used in the calculation. The horizontal axis shows the frequency detuning from $193\,580$ GHz. The vertical lengths of the lines can be arbitrarily drawn. Here they are the longest for the modes with $q = 1$ and the modes with $q > 1$ have shorter length in an increasing order of q.

resonant frequencies. The frequency difference between TE and TM WGMs is of great importance, since the magnon-induced Brillouin scattering is thought to involve both of them. For the same mode indices, the frequency difference between the TE and the TM WGMs is estimated using Eq. (2.8) to be

$$\frac{(\Omega_{\text{TM}} - \Omega_{\text{TE}})}{2\pi} = \frac{c}{\pi n_r D} \sqrt{1 - \frac{1}{n_r^2}}, \tag{2.9}$$

where D being the diameter of the resonator and $n_r = 2.19$ the refractive index. The frequency difference $(\Omega_{\text{TM}} - \Omega_{\text{TE}})/2\pi$ with Ω_{TE} and Ω_{TM} representing the respective resonant frequencies is plotted as a function of the sphere diameter in Fig. 2.4.

Figure 2.4: Calculated frequency difference of the TE and the TM WGM resonances for some cases.

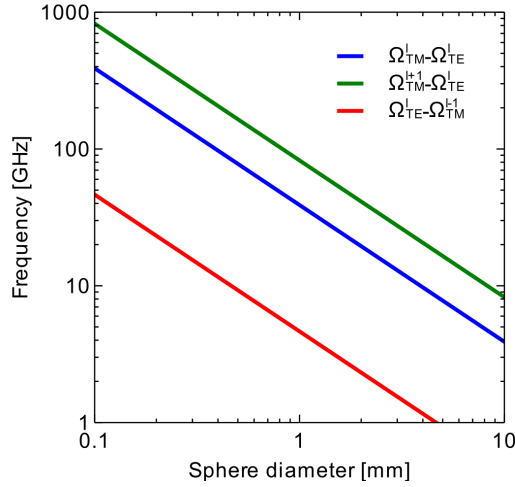**Quality factor**

Along with the resonant frequency, there is another important quantity characterizing WGMs, that is, the quality factor. For a harmonic oscillation, the quality factor Q is given by the ratio of the resonant frequency to the full-width-half-maximum (FWHM) of the Lorentzian lineshape. Its inverse $1/Q$ quantifies the loss which is well modeled by the sum of the possible forms of losses[2]. The possible contributions to the loss $1/Q_{\mathrm{WGM}}$ of WGM are thought to be the radiation into free space ($1/Q_{\mathrm{rad}}$, radiation loss), the absorption in a material ($1/Q_{\mathrm{abs}}$) and the scattering caused by the surface roughness ($1/Q_{\mathrm{s}}$) and the contamination ($1/Q_{\mathrm{c}}$):

$$\frac{1}{Q_{\mathrm{WGM}}} = \frac{1}{Q_{\mathrm{rad}}} + \frac{1}{Q_{\mathrm{abs}}} + \frac{1}{Q_{\mathrm{s}}} + \frac{1}{Q_{\mathrm{c}}}.$$

Among these, the radiation loss usually give negligible contribution to a sufficiently large resonator ($> 100 \times$ wavelength). In the case of frequently used materials such as fused silica and CaF_2, the material absorption is so small that the dominant contribution is usually thought to be the surface roughness and the contamination. However, in the case of the YIG resonator, the absorption coefficient of 0.03 cm^{-1} [26]

---

[2]We do not assume here the existence of the cascaded processes, where the total amount of loss is related to the sum of the lifetimes of each process.

gives the maximum quality factor of about 3×10^6 if limited by the absorption, while the surface scattering caused by the finely polished surface gives the maximum Q of more than the order of 10^8.

2.2 Orbital angular momentum of WGM light

Let us now investigate more about WGM, especially in the perspective of what degree of freedom WGM light has and possibly exchange with other particles, such as the gaseous atoms or the elementary excitations in solids. As seen in the previous section, WGM light has unique polarization nature, that is, it has the spin degree of freedom in the direction perpendicular to the plane of the orbit. Moreover, if we look at the inner region of the TM WGM, the direction of the spin depends on the circulation direction of the WGM. These properties can be seen from the time-evolution of the electric field at a fixed point in WGMs. At this point, it is natural to think about the spatial texture of the electric field, which seems to give information about the *orbital angular momentum of light* [27], especially of the WGM light.

We rewrite the electric fields of the TE and the TM WGMs [Eqs. (2.4) and (2.5)] below to see what happens. For simplicity, we put the coefficients as

$$E_{lm,\theta}^{(\text{TE})} = \frac{-m}{\sin\theta}e^{im\phi}P_l^m(\cos\theta)z_l(kr)$$

$$E_{lm,\phi}^{(\text{TE})} = e^{im\phi}\frac{dP_l^m(\cos\theta)}{d\theta}z_l(kr)$$

$$E_{lm,r}^{(\text{TM})} = \frac{z_l(kr)}{kr}e^{im\phi}\left[l(l+1)\right]P_l^m(\cos\theta)$$

$$E_{lm,\theta}^{(\text{TM})} = e^{im\phi}\frac{dP_l^m(\cos\theta)}{d\theta}\frac{1}{kr}\frac{d[krz_l(kr)]}{d(kr)}$$

$$E_{lm,\phi}^{(\text{TM})} = me^{im\phi}\frac{P_l^m(\cos\theta)}{\sin\theta}\frac{1}{kr}\frac{d[krz_l(kr)]}{d(kr)}$$

to get the TE and TM electric fields

$$\boldsymbol{E}_{lm}^{(\text{TE})} = E_{lm,\theta}^{(\text{TE})}\boldsymbol{e}_\theta + iE_{lm,\phi}^{(\text{TE})}\boldsymbol{e}_\phi,$$

$$\boldsymbol{E}_{lm}^{(\text{TM})} = E_{lm,r}^{(\text{TM})}\boldsymbol{e}_r + E_{lm,\theta}^{(\text{TM})}\boldsymbol{e}_\theta + iE_{lm,\phi}^{(\text{TM})}\boldsymbol{e}_\phi.$$

These expressions can be further simplified by noting that the function $P_l^m(\cos\theta)$ is relatively slowly varying with the variable θ in the vicinity of the equator ($\theta = \pi/2$), thus allowing us to put $E_{lm,\phi}^{(\text{TE})} = E_{lm,\theta}^{(\text{TM})} = 0$. Furthermore, we are interested in the
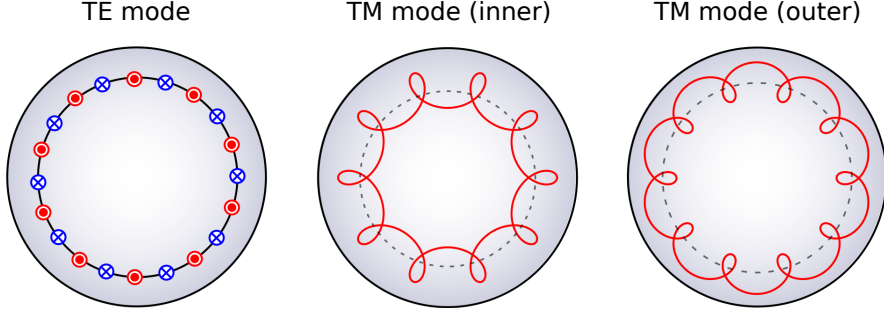
Figure 2.5: Schematic pictures of the instantaneous direction of electric fields for TE and TM modes. Both have the azimuthal mode indices $l = m = 10$ in the polar coordinates. Note that in the case of TM-mode, the hypotrochoid (red line) represents the trajectory of the arrowhead of the electric field vector and this is the case for the inner region of the WGM. In the case of the outer region of the WGM, the trajectory becomes the epitrochoid.

circularly polarized components of the fields, so that the analysis below proceeds with the simplification $E_{lm,r}^{(\text{TM})} = E_{lm,\phi}^{(\text{TM})} \stackrel{\text{def}}{=} E_{lm}^{(\text{TM})}$ (and we denote the TE component as $E_{lm,\theta}^{(\text{TE})} \stackrel{\text{def}}{=} E_{lm}^{(\text{TE})}$). Of course this is not true everywhere in the WGM profile. The realistic distributions of the polarizations of the TM mode will be considered later in this Section. Finally, we have simple expressions of the electric fields of the TE and the TM WGMs as followings:

$$\boldsymbol{E}_{lm}^{(\text{TE})} = E_{lm}^{(\text{TE})} \boldsymbol{e}_\theta,$$
$$\boldsymbol{E}_{lm}^{(\text{TM})} = E_{lm}^{(\text{TM})} (\boldsymbol{e}_r + i\boldsymbol{e}_\phi).$$

So far we are not quite conscious of the circulation direction of the WGM. In order to reverse the circulation direction, we only have to replace every m in the expression by $-m$ ($m > 0$). Explicitly writing the dependence on the circulation direction, we can write the fields as

$$\boldsymbol{E}_{lm}^{(\text{TE})} = \pm E_{lm}^{(\text{TE})} e^{\pm im\phi} \boldsymbol{e}_\theta, \tag{2.10}$$
$$\boldsymbol{E}_{lm}^{(\text{TM})} = E_{lm}^{(\text{TM})} e^{\pm im\phi} (\boldsymbol{e}_r \pm i\boldsymbol{e}_\phi), \tag{2.11}$$

with the upper and the lower signs are respectively for the case of the CW and CCW WGMs being considered. Here the ϕ-dependent exponential factors are shown

13

explicitly. Indeed, these exponential factor are responsible for the orbital angular momentum of the WGM light, as can be expected[3]. To gain deeper insight, it would be useful to switch to Cartesian coordinates from spherical coordinates. By the coordinate transformation, we see that

$$\boldsymbol{e}_\theta = -\boldsymbol{e}_z$$
$$\boldsymbol{e}_r \pm i\boldsymbol{e}_\phi = e^{\mp i\phi}(\boldsymbol{e}_x \pm i\boldsymbol{e}_y)$$

and Eqs. (2.10) and (2.11) become

$$\boldsymbol{E}_{lm}^{(\mathrm{TE})} = \mp E_{lm}^{(\mathrm{TE})} e^{\pm im\phi} \boldsymbol{e}_z, \tag{2.12}$$

$$\boldsymbol{E}_{lm}^{(\mathrm{TM})} = E_{lm}^{(\mathrm{TM})} e^{\pm i(m-1)\phi}(\boldsymbol{e}_x \pm i\boldsymbol{e}_y). \tag{2.13}$$

The important point in the above expression is the variation of the exponential factors. Though in the TE mode the exponent is unchanged, in the TM mode it turns out to be $m-1$. What this means is clear. Since the texture made by the electric field vector is counter-rotating with respect to the orbit of the WGM light, the total number of the rotations of the texture (or the phase) reduces by 1.[4] In Fig. 2.5, we schematically show the instantaneous directions of the electric fields of the TE and TM modes. Both have the same mode indices in the polar coordinates and one can see that the total phase rotation seen in the Cartesian coordinates is $2\pi \times 9$ rad for the TM mode, whereas $2\pi \times 10$ rad for the TE mode.

Polarization distribution of the TM WGM

Above consideration applies when $\mathrm{d}[krz_l(kr)]/\mathrm{d}(kr) > 0$ holds as assumed in Eq. (2.6), however, the TM WGMs also show $\mathrm{d}[krz_l(kr)]/\mathrm{d}(kr) < 0$ in the outer region inside the sphere. In order to avoid messing up our mind, we present here only the polarization distribution of the TM WGM in the case of CW orbit and the detailed descriptions are postponed, which we will revisit in Sec. 4.2.

Suppose that the electric field at some position is given as $\boldsymbol{E} = E_x \boldsymbol{e}_x + iE_y \boldsymbol{e}_y$ with unequal coefficients $E_x > E_y$, which is the case for the TM WGM. When the

---

[3]The rigorous, meaningful definition of the orbital angular momentum of light is still under discussion [28, 29]. We simply admit the exponent of the exponential factor divided by $i\phi$ as the orbital angular momentum of the mode.

[4]This is analogous to the difference between the sidereal day and the apparent sidereal day.
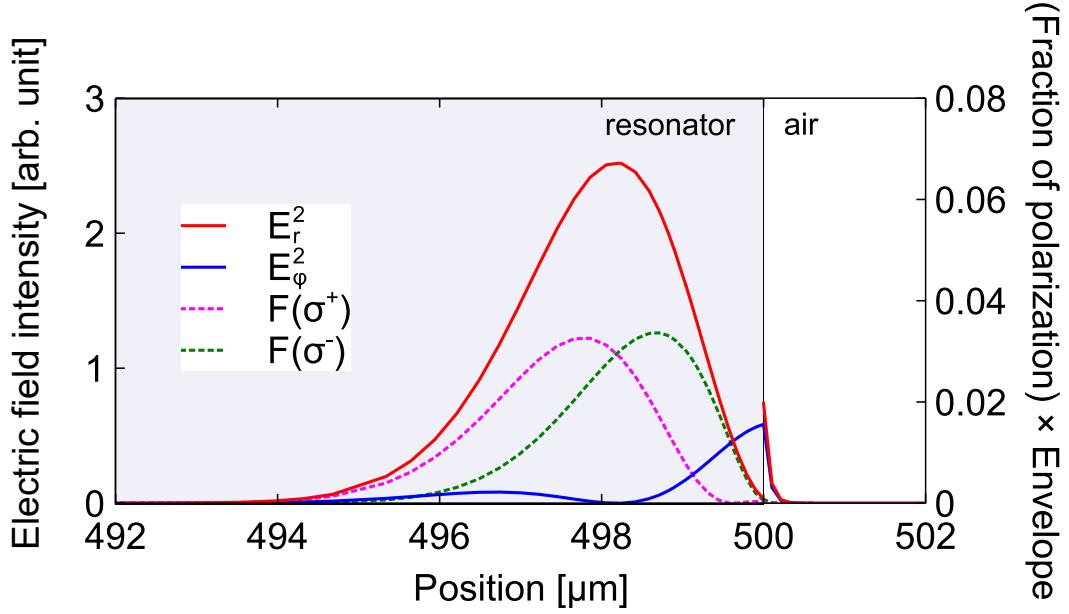
Figure 2.6: Calculated intensity distributions of the radial (red solid) and azimuthal (blue solid) components of the electric field with $F(\sigma^{\pm}) = |\boldsymbol{E}(\boldsymbol{r})|^2 f(\sigma^{\pm})$ (magenta and green dotted lines, see main text) being plotted in an arbitrary unit.

quantization axis is directing along z-axis, we rewrite this as

$$E_x \boldsymbol{e}_x + i E_y \boldsymbol{e}_y = \frac{E_x + E_y}{\sqrt{2}} \boldsymbol{e}_+ + \frac{E_x - E_y}{\sqrt{2}} \boldsymbol{e}_-$$

$$= E^+ \boldsymbol{e}_+ + E^- \boldsymbol{e}_-$$

where $\boldsymbol{e}_{\pm} = (\boldsymbol{e}_x \pm i\boldsymbol{e}_y)/\sqrt{2}$ denote the basis vectors of the circular polarizations. The fraction of the intensity of each polarization component is thus calculated to be

$$f(\sigma^{\pm}) = \frac{(E^{\pm})^2}{(E^+)^2 + (E^-)^2} = \frac{(E_x \pm E_y)^2}{2(E_x^2 + E_y^2)},$$

with σ^+ (σ^-) being the circular polarization of the spin $+1$ (-1).

The electric field of the TM WGM is exactly the form described above, and with the spatial distribution of the polarization components we can estimate $f(\sigma^{\pm})$. The calculated distributions of the radial (E_r) and azimuthal (E_{ϕ}) components of the electric field of the WGM are obtained by FreeFEM++ [21, 22], with the resonator diameter of 1 mm, refractive index of $n_r = 2.19$ and the resonant wavelength of

15

around 1550 nm. In Fig. 2.6, the intensity distributions of the radial and azimuthal components E_r^2 (red solid) and E_ϕ^2 (blue solid) are shown. The intensity distributions of the two circular polarizations are also plotted in the figure, which are defined by $F(\sigma^\pm) = |\boldsymbol{E}(\boldsymbol{r})|^2 f(\sigma^\pm)$ (magenta and green dotted curves). This provide us information of where each polarization component sit in the intensity profile of the WGM. As we can see from the figure, the distributions of the two polarization states does not coincide. This phenomenon is attributed to the spin-orbit coupling of photon, which has been recently recognized as the intrinsic property of Maxwell equations by analyzing the topological properties of photons in terms of the Berry curvature and the spin Hall effect of light [30, 31, 32, 33, 34].

2.3 Coupling to WGMs in a YIG sphere

There are several techniques to couple to the WGMs. We mainly use the coupling via a prism and a tapered optical nanofiber. Every coupling technique have one thing in common that the evanescent wave appearing in the dielectric interface is utilized. This is simply because the WGM is strongly confined inside the dielectrics by the multiple total internal reflections and the efficient way of getting access to WGM is to make an overlap with the evanescent region of the WGMs.

To achieve an efficient coupling, we should note two things. One is the spatial-mode matching and the other is the wavevector matching. The former is crucial because the size of the spatial structure of the WGM is small comparable to the wavelength. The latter is also important and usually the material with much or less larger refractive index compared to the resonator material is used for the coupling. Another important factor is the quality factor of the WGM. If it is too low, the signal of the WGM will be too small to be distinguished from the background noise.

2.3.1 Prism coupling

When the light propagates from the material with high refractive index to that with low index, the total internal reflection occurs if the incident angle exceeds the critical angle. The evanescent wave accompanied to the total internal reflection is used for the coupling to the WGM. We describe below the basic formulae and derive the condition
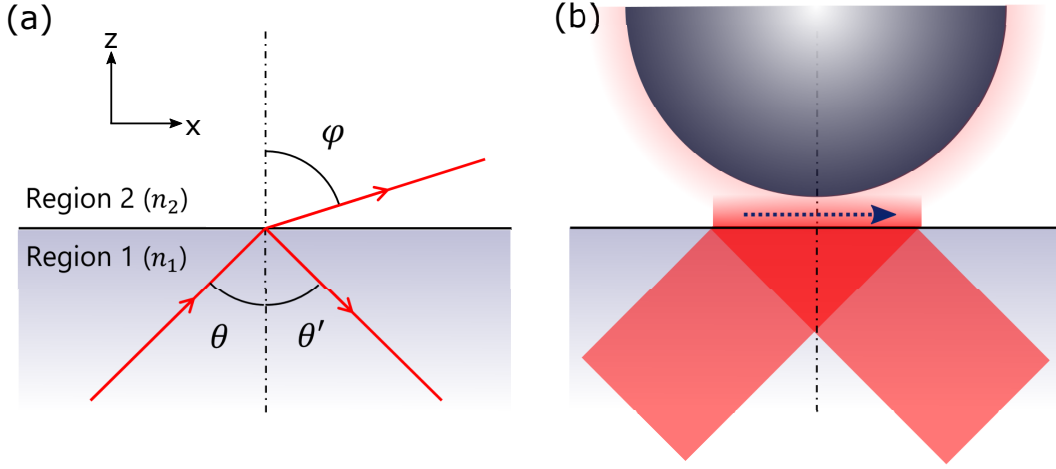
16

Figure 2.7: (a) Reflection and refraction at the dielectric interface. (b) Evanescent field and a WGM resonator.

of the wavevector matching.

First we consider the situation depicted in Fig. 2.7(a). Light is propagating in the xz-plane and incident to the boundary of region 1 and 2 with refractive index n_1 and n_2, respectively. We suppose $n_1 > n_2$ here. The angles of incident (θ), reflected (θ') and refracted (φ) beams are related by

$$\theta = \theta', \qquad n_1 \sin\theta = n_2 \sin\varphi.$$

As the incident angle θ gets larger, one meets a situation that the corresponding angle φ has no real-valued solution. The critical angle θ_c is given by

$$\sin\theta_c = \frac{1}{n_{12}} = \frac{n_2}{n_1}$$

and when $\theta > \theta_c$, the total internal reflection takes place. In this case, the purely imaginary value of the angle φ can be considered in the region 2, which is equivalent to the consideration of the purely imaginary wavevector. Such an angle φ satisfies $\cos\varphi = -\sqrt{1 - \sin^2\varphi} = -i\sqrt{n_{12}^2 \sin^2\theta - 1}$. With this, the electric field in the region 2 becomes

$$E = A e^{-i n_1 k_0 x \sin\theta} e^{-n_2 k_0 z \sqrt{n_{12}^2 \sin^2\theta - 1}}$$

where k_0 is the wavevector in a vacuum. Note that the electric field has a tail that rapidly falls off in the region 2, which is called the evanescent field. In addition, the

17

evanescent field effectively propagates along x axis with the wavevector $n_1 k_0 \sin \theta$. We want this effective wavevector to be the same as that of the WGM light (see Fig. 2.7(b)). The wavevector-matching condition thus revealed to be

$$n_1 k_0 \sin \theta = n_r k_0$$
$$\Longleftrightarrow \sin \theta = \frac{n_r}{n_1}. \tag{2.14}$$

Therefore, the angle satisfying the wavevector-matching condition reads $\theta = \arccos{(n_r/n_1)}$. One might be aware of the fact that this angle is just the same as the critical angle with $n_2 = n_r$. Therefore, if we can prepare a prism with the refractive index properly larger than the WGM resonator, in principle we can match the wavevectors of the two evanescent fields.

As for the spatial-mode matching, it would be not easy to get a good overlap. This is because the WGM is strongly confined around the perimeter of the resonator. We can roughly estimate the size of the WGM via its mode volume [38]

$$V_{\text{eff}} \simeq \frac{\left(\int \boldsymbol{E}^2 \mathrm{d}\boldsymbol{r} \right)^2}{\int \boldsymbol{E}^2 \boldsymbol{E}^2 \mathrm{d}\boldsymbol{r}}$$
$$\simeq 3.4 \pi^{\frac{3}{2}} \left(\frac{\lambda}{2\pi n_r} \right)^3 l^{\frac{11}{6}} \sqrt{l - |m| + 1}.$$

For simplicity we assume the shape of the WGM as a torus of major and minor radii being a and b, respectively, and consider the fundamental mode $l = |m|$. The diameter of the sphere we use is around 1 mm and corresponding mode's order l is about 4400. Using the volume of the torus $\pi b^2 \times 2\pi a$, the minor diameter of the torus can be estimated to be around 4 μm. The actual shape of the WGM is, of course, not an ideal torus but rather the one with an prolate cross-section in $r\theta$ plane. Therefore the width of the distribution along r axis become very close to the diffraction limit, while the one along θ axis is rather large.

We saw in Fig. 2.1 and roughly estimated just above that the cross-sectional size of the WGM is less than 10 μm. In order to get a good spatial-mode matching through a prism, one has to focus the incident beam down to the order of 10 μm or less, which is not so easy. We prepare an incident beam with a moderate diameter, which is benefitcial in terms of the feasibility of day-to-day experiment and the stability of the coupling. Another benefit of using a prism is that whether the TE or the TM mode is
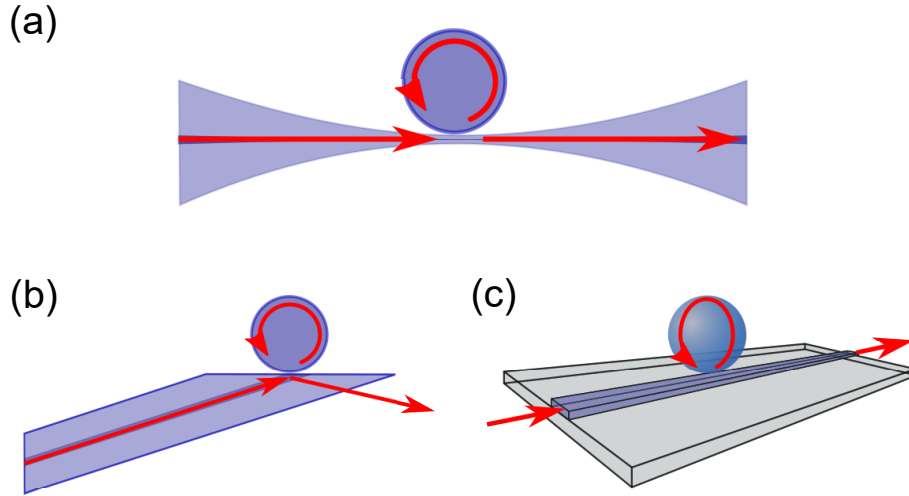
Figure 2.8: Various coupling methods to WGMs. (a) A tapered optical nanofiber. (b) An angle-polished fiber tip. (c) A dielectric waveguide.

coupled is unambiguously determined by the input linear polarization, from which we can acquire some crucial information about the magnon-induced Brillouin scattering.

2.3.2 Other coupling schemes

The prism coupling is seemingly the most handy setup because it is rigid and robust against the contamination. The experiments with a prism can take place in an environment without any vacuum. However, in some cases still there are merits using some other coupling schemes in spite of the vulnerability against the contamination, especially regarding the large spatial-mode coupling. Below we list some alternatives for such a purpose.

Tapered optical nanofiber [Fig. 2.8(a)]

Since the experiments on the optical whispering gallery mode resonator has been successful with the silica microsphere, microtoroid and other morphologies [36, 37], the coupling via the tapered optical nanofiber has been a very commonly used, matured technique. The tapered optical nanofiber is made by pulling the bare optical fiber during it is heated up, and the diameter of the thinnest part is reduced down to a few hundreds of nanometers. The evanescent wave appears at the tapered region whose

diameter is sufficiently small, and can be used for the coupling to the WGMs. The tapered optical nanofiber can confine light mode in a near-diffraction limit in the tapered region and offers a nice way to achieve large spatial-mode matching, whereas it is extremely fragile against forces and contaminations. Since the surface quality of the silica is known to be degraded possibly by the humidity [39], the use of a vacuum chamber provides an ideal protection of the nanofiber.

Angle-polished fiber [Fig. 2.8(b)]

By the angled polishing of the optical fiber, one can get a situation that the light going out of the fiber is totally internally reflected at the surface. The confinement of the optical mode is inferior in this case to that of the tapered optical nanofiber, however, the angle-polished fiber have some advantage in its robustness and handiness.

Dielectric waveguide [Fig. 2.8(c)]

The dielectric optical waveguide technique can be the most efficient way to couple to the resonator with high refractive index. Its advantage is not limited to this, but that one can design the waveguide dimensions at will. Furthermore, the waveguide is in most case put on a low-index substrate, so that it is very rigid in contrast to the tapered optical nanofiber.

2.4 Observation of WGMs in a YIG sphere

2.4.1 Experimental setup

The important points of the experiment for observing the WGMs in a YIG sphere are (i) the coupling scheme we adopt and (ii) how the YIG sphere is supported. There is nothing to say about the importance of the first, and of the second, it should be noted that the glue which holds the sphere on the rod can affect or break the symmetry of WGMs in a sphere. And of course, if the glue touches the WGM even in the evanescent region, we would not observe any WGMs due to the huge losses induced by the glue. Below, we describe our experimental setup in detail.

First, we adopt the prism coupling for the clarity of the input polarization and for the relatively easy experimental requirements, that is, the experiment can be operated
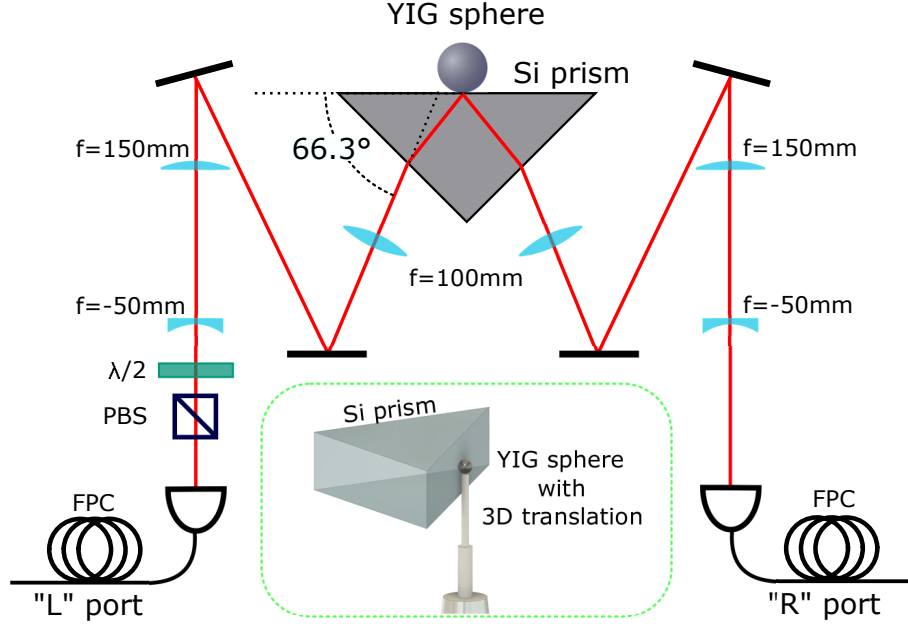
20

Figure 2.9: Schematic representation of the experimental setup of the optics. The polarization of the input 1550 nm-wavelength laser is defined through a fiber polarization controller (FPC), a polarization beam splitter (PBS) and a half-wave plate ("$\lambda/2$"). The laser beam is first expanded by a pair of lenses to the diameter of around 5 mm and then focused toward a YIG sphere put on the surface of a silicon prism. The inset shows the schematic view of how the sphere with a rod is placed.

at normal atmosphere. As the material for the prism, single-crystal silicon is selected because of its high refractive index of about 3.6 for the telecommunication wavelength. This allows the effective wavevector of the evanescent wave to be matched with that of the WGM with proper incident angle to the prism.

Our sample, the YIG sphere from Ferrisphere inc., is mounted on an alumina rod by the glue. For a 1mm-diameter sphere the glued part looks sufficiently far from the periphery where the WGM runs around. Therefore in the most experiment in this thesis a YIG sphere with the diameter D of around 1mm is used. In order to observe WGMs in the mounted YIG sphere, the configuration of the prism and the sphere with the rod should be like in the inset of Fig. 2.9. The free spectral range (FSR) of the WGM is then calculated to be FSR $\simeq c/\pi n_r D = 43$ GHz, so that for the spectroscopic purpose, it is desirable to sweep the laser frequency by at least 100 GHz

in a few seconds. The reason for the requirement of such a short sweep time is that it saves a great amount of time to find and optimize the alignment for the coupling to WGMs. The laser source we use (Santec, TSL-510, model C) has an ability of the sweep range over 100 nm $\simeq$ 10 THz with the maximum sweep speed of 100 nm/s and is suitable for our measurement. The frequency sweep can be continuously done and the linewidth of the laser is at most 10 MHz, therefore the frequency resolution is also sufficient since the maximum, absorption limited quality factor 10^6 of WGM indicates the minimum linewidth of sub-hundred MHz.

The whole optical setup is shown schematically in Fig. 2.9. The laser light from the laser source first passes through a fiber polarization controller (FPC) so that the transmission after the polarization beam splitter (PBS) becomes maximal. The collimated laser beam of diameter $\sim$ 1 mm is first expanded by a pair of plano-concave and plano-convex lenses, and then focused toward the surface of a prism. The beam diameter at the surface of the prism is ideally about 10 μm. The angle between the incident beam and the surface of the one on which YIG is laid is calculated by Eq. (2.14) to be 66.3 degree.

The input polarization to the WGM resonator is determined by the half-wave plate (indicated in the figure by "$\lambda/2$"), where the horizontal linear polarization[5] and vertical one[6] couple respectively to the TE and the TM WGMs. The WGM spectra are observed by monitoring the power of the totally internally reflected beam during the laser frequency is swept.

2.4.2 Observation of WGMs in a YIG sphere

By the setup and the procedure described above, we are ready to observe the WGMs. In reality, we must first softly lay YIG sphere on the surface of the prism and by carefully moving the sphere along the surface with the three-dimensional translation stage, we must search for the position of the light till the WGMs are found. Once we get the periodic, but not background-like dips in the signal of the optical power, the normalization by the background signal allows us to get the WGM spectra like those shown in Fig. 2.10.

---

[5]linear polarization parallel to the sheet
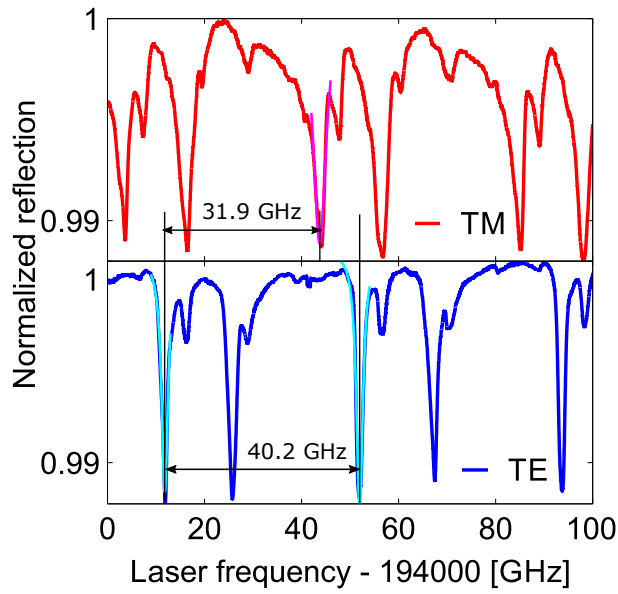
[6]linear polarization normal to the sheet

Figure 2.10: Observed WGM spectra of the TM (red) and the TE (blue) modes in the 1mm-diameter YIG sphere. Magenta and cyan curves are the Lorentzian fittings to the modes.
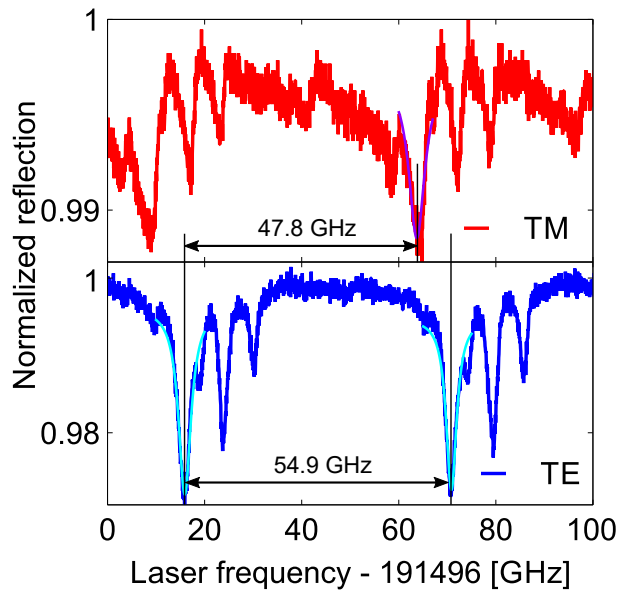

Figure 2.11: Observed WGM spectra of the TM (red) and the TE (blue) modes in the 0.75 mm-diameter YIG sphere. Purple and cyan curves are the Lorentzian fittings to the modes.
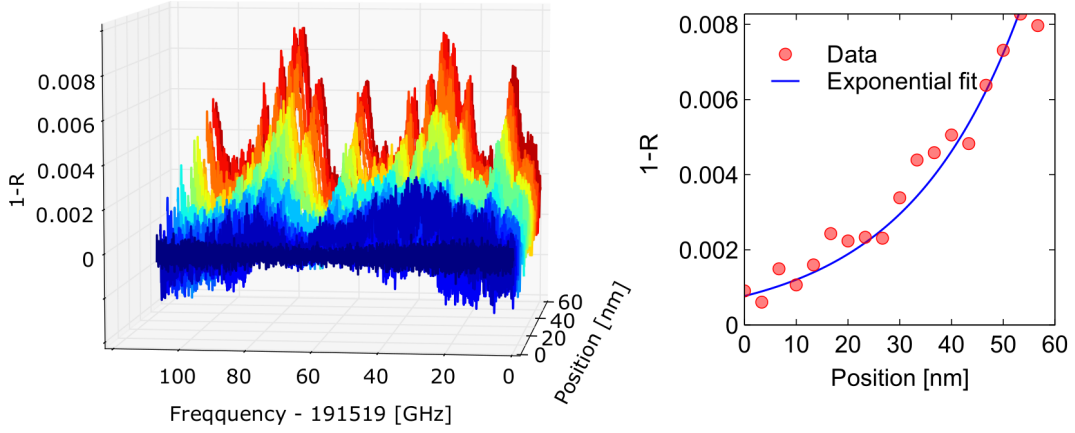
Figure 2.12: Observed WGM spectra of TE modes with variable positions perpendicular to the prism surface. The left panel shows the whole spectra of the fraction of the reflected optical power R subtracted from 1. The right panel shows the peak height of one of the WGMs versus the position. The blue curve is the exponential fit to the data for the estimation of the characteristic distance that the signal of the WGMs can be observed.

The spectra shown in Fig. 2.10 are taken for the 1mm-diameter YIG sphere, with red and blue plots representing the TM and the TE modes, respectively. Some modes are fitted by Lorentzian functions, which are shown by a magenta curve for the TM mode, and cyan ones for the TE modes. We can extract the positions of the apparent resonances and the full-width-half-maximum (FWHM) of the spectrum of a single mode.

Let us first look at the resonance positions, especially in terms of the FSR and the effect of the geometrical birefringence. The FSR of 40.2 GHz is evaluated from the results of the fittings for the two TE WGMs (cyan curves). On the other hand, the geometric birefringence in the whispering gallery resonator results in the frequency difference between TE and TM modes with the same indices, which is evaluated to be 31.9 GHz with the additional fitting of the TM resonance. Indeed, we cannot know the mode indices directly from the spectra, so that we check the consistency. Experimentally obtained values does not seem to contradict the theoretical prediction of 43.6 GHz and 38.8 GHz, respectively, in terms of the relative positions of the

resonances. [7]

Other spectra for the 750 μm-diameter YIG sphere are given in Fig. 2.11, with the same colors of the data and curves as in Fig. 2.10, except for the use of purple instead of magenta for visibility. By all the same procedure, we can get the FSR and the frequency difference between the TE and the TM WGMs as 54.9 GHz and 47.8 GHz for each one, which again do not violate the theory that says 58.1 GHz and 51.8 GHz.

We also investigate the variation of the depth of the dips with respect to the position along the normal direction to the surface of the prism. As discussed in the Sec. 2.3.1, the evanescent field in the total internal reflection appears in a very short lengthscale $\sim$ 100 nm from the surface. We construct an piezoelectric element into the translation stage and obtained the resolution of motion sufficiently below such a lengthscale. In the left panel in the Fig. 2.12 we plot the depth of the dips $1 - R$, R is the normalized reflection, as a function of the position. At the position of 0 nm the sphere is sufficiently far from the prism's surface and the spectrum there is used for the normalization. The increment of the position means the approach to the prism's surface. As the sphere goes closer to the surface, we can see the growing peaks of WGMs, and at around 55 nm they stop, which implies that the sphere is in contact to the surface. On the right in Fig. 2.12, the behavior of the highest peak is plotted and fitted by an exponential function $e(x) = A' \exp\left[(x - x0)/L\right]$, where x_0, A' and L are constants. Although we can see from the data directly, the lengthscale L, which allows us to see WGMs without the contact to the prism's surface, is evaluated to be 22.3 nm. We, for the stable coupling to the WGMs, have worked and will work with the YIG sphere touching on the surface of the prism.

Next, let us analyze the WGM resonance in terms of its spectral width. The FWHM of an observed mode generally consists of the contributions not only from the intrinsic loss of the WGM, but also from the coupling to the "environment", that is, the photon stream coupled to the WGM. We need some math to separate these two contributions. In order to do this, we consider the system of a prism-coupled WGM

---

[7]Non-negligible discrepancy between the experimentally observed effect of the geometrical birefringence and the one deduced from the theory is accounted for possibly by magnetic linear birefringence or Cotton-Mouton effect, which causes the difference of the refractive indices being on the order of 10^{-5} [40]. Such amount of difference of the refractive indices is reasonable for explaining the observed discrepancy between the theory and the experiment.
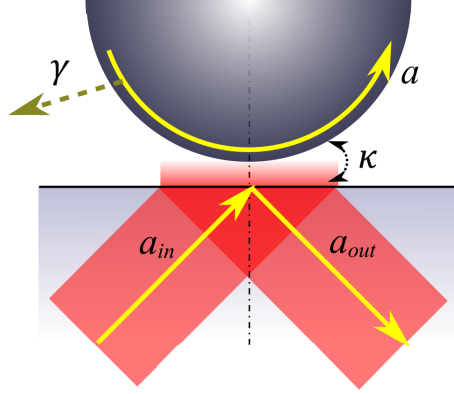
Figure 2.13: Schematic representation of the model of the prism-coupled WGM. See the main text for the definitions of the variables.

with the use of the Heisenberg's equation of motion for the bosonic operators a and $a^\dagger$, which represent the annihilation and the creation of WGM photon, respectively. The system is depicted in Fig. 2.13. The WGM is supposed to experience the intrinsic loss of the rate γ and external coupling by the traveling wave field with the rate κ. The external wave field is also expressed by the bosonic operators a_{in} for the input and a_{out} for the output fields. Given the Hamiltonian of WGM photon $\hbar\omega_{\text{res}}a^\dagger a$, where the resonant frequency of the WGM is denoted by ω_{res}, and the operators in the Heisenberg picture, the equation of motion of the operator a reads [41]

$$\frac{\mathrm{d}a}{\mathrm{d}t} = \left(i\Delta - \frac{\gamma + \kappa}{2}\right)a + \sqrt{\kappa}a_{\text{in}}. \tag{2.15}$$

Here we switched to the rotating frame with the input-field frequency ω and the detuning $\Delta = \omega - \omega_{\text{res}}$ is introduced. We also have a relation between input and output field, so-called the input-output relation

$$a_{\text{in}} + a_{\text{out}} = \sqrt{\kappa}a. \tag{2.16}$$

Now we are seeking the stationary solution of Eq. (2.15), which can be immediately obtained by realizing that the left hand side equals to zero. We denote the input (output) photon flux $a_{\text{in}}^\dagger a_{\text{in}}$ ($a_{\text{out}}^\dagger a_{\text{out}}$) by n_{in} (n_{out}) and the number of photons in the
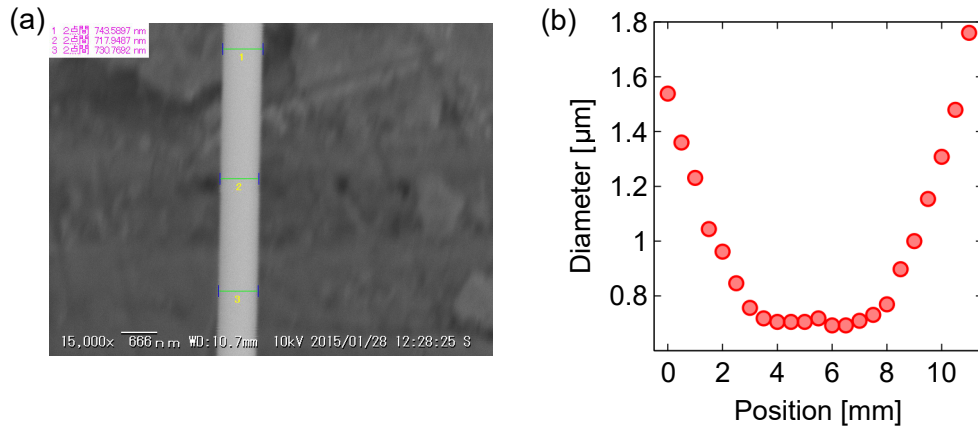
Figure 2.14: (a) A scanning electron microscope image of the thinnest region of the nanofiber. (b) Thickness of a nanofiber depending on the position along the fiber.
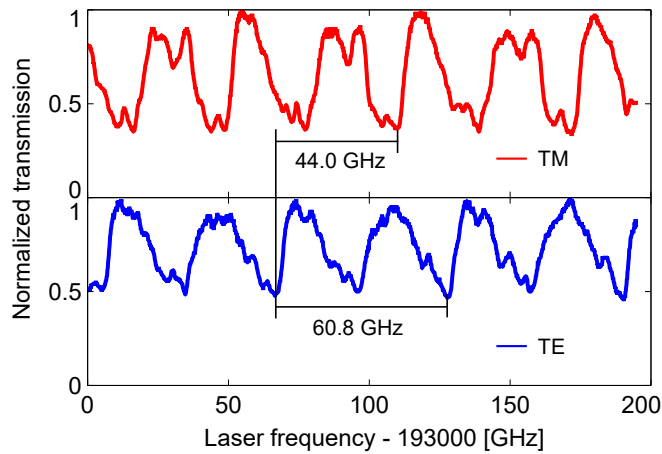

Figure 2.15: Spectra of the WGMs coupled via the tapered optical nanofiber. The numbers indicated in the figure are the FSR and the frequency difference between TM and TE resonances estimated from the spectra.

WGM by n_cav. Then the stationary solution results in the following relations:

$$n_\text{cav} = \frac{\kappa}{\Delta^2 + \left(\frac{\gamma+\kappa}{2}\right)^2} n_\text{in}, \tag{2.17}$$

$$\frac{n_\text{out}}{n_\text{in}} = \frac{\Delta^2 + \left(\frac{\gamma-\kappa}{2}\right)^2}{\Delta^2 + \left(\frac{\gamma+\kappa}{2}\right)^2}$$

$$= 1 - \frac{\gamma\kappa}{\Delta^2 + \left(\frac{\gamma+\kappa}{2}\right)^2}. \tag{2.18}$$

Equation (2.18) gives the reflection spectrum of the Lorentzian lineshape, and its FWHM and depth are given respectively by $\gamma + \kappa$ and $4\gamma\kappa/(\gamma + \kappa)^2$. Therefore, in our case of interest, we can derive intrinsic and extrinsic loss rates γ and κ from the width and depth of the resonance in the normalized spectrum. For instance, let us now look at one of the TE resonances observed in the bottom left of Fig. 2.10. The fitting says its FWHM is 1.608 GHz and depth of the dip is 0.01163, from which we can extract $\gamma = 1.605$ GHz and $\kappa = 3$ MHz. Note that, however, here we assume the weak coupling regime, i.e., $\kappa < \gamma$ in obtaining these values. This assumption is verified experimentally by Fig. 2.12, since till the contact to the prism surface the system does not reach at critical coupling regime, where $\gamma = \kappa$.

All the way here, we can say that the intrinsic quality factor is 1.2×10^5 for the mode under consideration. If the quality of the YIG crystal is good enough, the absorption-limited quality factor is expected to be on the order of 10^6, still an order of magnitude larger than the one we get. Then, is there any possibility that the quality of the crystal is bad to degrade the quality factor? This seems to be not the case, because just after our work, a YIG sphere is polished and the quality factor improves up to 6×10^5 in the Ref. [42]. Their work clearly showed that the quality factor of WGM in YIG is for now dominated by the surface roughness, which seems also true for our case.

2.5   Observation of WGMs via tapered optical nanofiber

Thanks to the collaboration with Hakuta lab., the University of Electro-Communication, we can also test the tapered optical nanofiber to observe WGMs in a YIG sphere. The image shown in Fig. 2.14(a) is a scanning electron microscope image of the thinnest part of the tapered region. The diameter of the thinnest part of the nanofiber can

be examined by taking images at various positions and the results are plotted in Fig. 2.14(b). From this plot, the waist diameter of the nanofiber is evaluated to be around 700 μm, sufficiently thin to be utilized for the evanescent coupling to the WGMs.

By putting the YIG sphere on the nanofiber and monitoring the transmitted light intensity, the WGM can be observed as dips at some laser frequencies, similarly to the case using the prism. Figure 2.15 presents the obtained spectra of the WGMs for the two polarizations indicated in the figure. Overall, the obtained spectra consist of a number of resonance dips overlapping with each other. The fractional depths of the dips are deeper (reaching at 60 %) than those observed via the prism (around 1%), which implies that by using a nanofiber we can get the larger coupling to the WGMs, as expected. Given the diameter of the sphere being 0.75 mm, the FSR and the frequency difference between the TM and the TE WGMs are expected to be 58.1 GHz and 51.8 GHz, respectively. From the experimentally observed spectra, these are estimated to be 61 GHz and 44 GHz, as indicated in the figure. The latter deviates from the expectation. The estimation of the quality factor by fitting seems to be not feasible in this case, because of the dense spectra.

Chapter 3

Walker modes in a YIG sphere

Magnetism has been one of the most intensely studied topics in the material science, and even now researchers in condensed matter physics search for the novel magnetic state and their exotic excitations. In this chapter we introduce one of the most fundamental excitations in a ferromagnetic material, that is, the magnetostatic magnon modes. In particular, Walker modes refer to the ones in a spheroidal sample. In the scope of the interaction with WGM light, we review the basic aspects and analyze the orbital angular momenta of the Walker modes.

3.1 Walker modes

The magnetostatic magnon modes, or the Walker modes, have been addressed in early times in 1950's [43, 44, 45] for the special material geometry of spheroids, for which the analytical solutions are available [43, 45]. Here we consider the case of the spherical geometry.

3.1.1 Distribution of transverse magnetization

When magnons are excited in a ferromagnet, its magnetization precesses about the applied magnetic field. Below we describe how to obtain the distribution of the transverse component, or the precessing part, of the magnetization. The magnetostatics of the magnetization can be described by the Maxwell's equations

$$\nabla \cdot \boldsymbol{B} = 0, \quad \nabla \times \boldsymbol{H} = \boldsymbol{0}.$$

31

Mode index (n, m)	Transverse magnetization M_x, M_y
(m, m)	$M_x \sim (x + iy)^{m-1}$
	$M_y \sim i(x + iy)^{m-1}$
$(m+1, m)$	$M_x \sim z(x + iy)^{m-1}$
	$M_y \sim iz(x + iy)^{m-1}$
$(m+2, m)$	$M_x \sim \left[A_2 z^2 - B_2(x^2 + y^2) - C_2 \right] m(x + iy)^{m-1}$
	$\qquad - D_2(x + iy)^m (\kappa x - i\nu y)$
	$M_y \sim \left[A_2 z^2 - B_2(x^2 + y^2) - C_2 \right] im(x + iy)^{m-1}$
	$\qquad - D_2(x + iy)^m (i\nu x + \kappa y)$

Table 3.1: Analytical expressions of the distributions of the transverse magnetization for some mode families [45]. $m \geq 1$ for (m, m) and $(m+1, m)$ mode and $m \geq 0$ for others.

Here $\boldsymbol{H} = (H_x, H_y, H_i)$ is the magnetic field inside the material and $\boldsymbol{B} = \boldsymbol{H} + 4\pi \boldsymbol{M}$ (see footnote[1] for the unit) with the magnetization $\boldsymbol{M} = (M_x, M_y, M_S)$. The static magnetic field of strength H_0 is supposed to be applied in z-direction and $H_i = H_0 - 4\pi M_S$ regarding the demagnetization. Here $4\pi M_S = 1780$ G is the saturation magnetization. The dynamics of the magnetization oscillation can be described by the Landau-Lifshitz equation

$$\frac{\partial \boldsymbol{M}}{\partial t} = \gamma \boldsymbol{M} \times \boldsymbol{H}$$

with the gyromagnetic ratio $\gamma = 2\pi \times 2.8$ MHz/G.

Combining the Maxwell's equations and the Landau-Lifshitz equation, and introducing the magnetic potential by $\boldsymbol{H} = \nabla \psi_m$, one can obtain the Walker equation to be solved as

$$(1 + \kappa)\left(\frac{\partial^2 \psi_m}{\partial x^2} + \frac{\partial^2 \psi_m}{\partial y^2} \right) + \frac{\partial^2 \psi_m}{\partial z^2} = 0.$$

Here $\kappa = \Omega_H / (\Omega_H^2 - \Omega^2)$ is introduced with $\Omega_H = H_i / 4\pi M_S$ and $\Omega = \omega / 4\pi \gamma M_S$. The solutions can be labeled by indices (n, m, s), where the index m in the middle

[1]Here we use the CGS units in accordance with the majority of the literature. In the experimental part, however, we express the magnetic field strength in SI unit, namely in the unit of T. For reference, 1 T is equivalent to 10000 G.
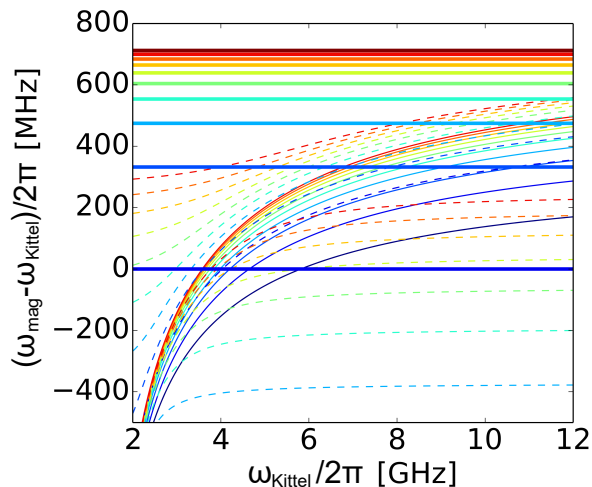
Figure 3.1: Frequencies of the Walker modes ω_{mag} with that of the $(1,1,0)$ mode (Kittel mode) as a reference ($\omega_{\mathrm{Kittel}} = 0$). Thick solid, thin solid and thin dashed lines represent respectively the $(n,m,s) = (m,m,0)$, the $(n,m,s) = (m+2,m,0)$ and the $(n,m,s) = (m+2,m,1)$ modes. The colors indicate the increasing number m in blue to red order.

represents the azimuthal profile of the mode and the difference of the first and the second indices $n-m$ is related to the mode profile along the polar angle. The third index s arises from the resonance equation where the $s = 0, 1, \cdots, s_{\mathrm{max}}$ are assigned for its solutions with the maximum number of solutions $s_{\mathrm{max}} + 1$. The resonance equation will be considered in Sec. 3.1.2. The radial profile depends on both the difference $n-m$ and the index s. In Ref. [45], a number of solutions are obtained. Several transverse magnetization distributions derived from the Walker equation are listed in Table 3.1. The quantity $\nu = \Omega/(\Omega_H^2 - \Omega^2)$ is also used in the table. The lowest-order Walker mode is that with mode index $(n,m) = (1,1)$, which has the uniform distribution of the transverse magnetization. This is, in particular, called the Kittel mode.
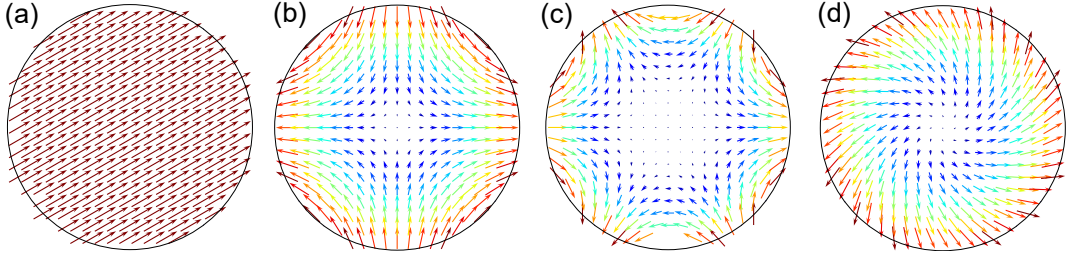
33

Figure 3.2: The transverse magnetization distributions for (a) $(1,1,0)$, (b) $(2,2,0)$, (c) $(3,3,0)$ and (d) $(2,0,0)$ Walker modes.

3.1.2 Resonant frequency

Once the solutions of the Walker equation is obtained, one can consider the boundary condition [45]:

$$n + 1 + \xi_0 \frac{(P_n^m(\xi_0))'}{P_n^m(\xi_0)} \pm m\nu = 0.$$

This condition, also called the characteristic equation, is also analyzed in Refs. [43, 45] to give the resonant frequencies. A number of mode frequencies are plotted with respect to the applied magnetic field in Fig. 3.1. When the characteristic equation has multiple solutions, those modes are additionally labeled by the non-negative integers indicating the order of the solution. The modes $(n, m) = (m, m)$ and $(m + 1, m)$ are the special cases where the characteristic equations are the first-order algebraic equation with only one solution, that is, $s = 0$. For instance, the Kittel mode is labeled by $(1, 1, 0)$. One thing to note is that the (m, m)-mode family all have the linear dependence of the frequencies on the magnetic field strength, and in particular the Kittel mode has its frequency written by $\omega_{\text{Kittel}} = \gamma H_0$.

YIG, the material of our interest, is known for its narrow ferromagnetic resonance linewidth. The Kittel mode in a YIG sphere has the linewidth of about a few MHz, which results in the quality factor of more than 10^3. The dominant loss of the Walker modes at room temperature is considered to be the coupling to acoustic phonons. The behavior of the linewidth in the low temperature region is investigated in the Ref. [46] and it is revealed that the coupling to two level systems dominates the loss.

3.2 Orbital angular momentum of Walker mode

So far we have both the distributions of the transverse magnetization and the resonant frequencies. Transverse magnetization distributions in several cases are shown in Fig. 3.2. As we can see, there appear many kinds of textures of the transverse magnetizations. When a field possesses such a phase structure, the non-zero momentum is associated with the field. In the present case, Walker modes are revealed to be endowed with the orbital angular momenta, which are well-defined by the axial symmetry of the YIG sphere.

According to the recent theoretical analysis on the linear and the angular momenta exhibited by the magnetic structures [47], the orbital angular momentum of magnons can be calculated by $-\boldsymbol{r} \times \nabla \Phi$ with the instantaneous angle of the local magnetization $\Phi = -\arctan\left(\mathrm{Re}[M_y]/\mathrm{Re}[M_x]\right)$. Let us see the examples of the $(1,1,0)$ and the $(2,2,0)$ Walker modes. First, the Kittel mode has a uniform transverse magnetization, namely $\Phi_{(1,1,0)} = \mathrm{const}$. Therefore its derivative vanishes and so does the orbital angular momentum. The $(2,2,0)$ mode has the transverse magnetization distribution of the form $M_x \sim x + iy = \sqrt{x^2 + y^2}e^{i\phi}$ and $M_y \sim i(x+iy) = i\sqrt{x^2+y^2}e^{i\phi}$, from which we see that $\Phi_{(2,2,0)} = \phi$. As a result, the orbital angular momentum is calculated to be $+1$. Another example is the $(2,0,0)$ mode, whose transverse magnetization is written by $M_x \sim x - iy = \sqrt{x^2+y^2}e^{-i\phi}$ and $M_y \sim i(x-iy) = i\sqrt{x^2+y^2}e^{-i\phi}$. Here we assume $\kappa = \nu$ in the Table 3.1, namely the magnons are resonantly excited. This mode has the orbital angular momentum of -1.

3.3 Quantization of magnetization oscillation

So far we treated the magnetization oscillation as a classical phenomenon. Here, for the later use, we consider the quantized form of the magnetization oscillation, or magnon. To begin with, we introduce the spin density operator, which is the sum of the local spins over the all relevant lattice sites in the crystal. Suppose that the Pauli matrices $\boldsymbol{\sigma_j}$ at site $\boldsymbol{j}$ are given so that they satisfy the commutation relation

$$\left[\sigma_{\boldsymbol{j}}^{\alpha}, \sigma_{\boldsymbol{k}}^{\beta}\right] = 2i\epsilon_{\alpha\beta\gamma}\sigma_{\boldsymbol{j}}^{\gamma}\delta_{\boldsymbol{jk}}$$

where $\epsilon_{\alpha\beta\gamma}$ (α, β and γ are) is the Levi-Civita symbol and δ_{jk} the Kronecker's delta. With this the spin density operator can be written as

$$s(r) = \frac{1}{2}\sum_j \sigma_j \delta(r - j)$$

and the following commutation relation can be immediately checked:

$$\left[s_\alpha(r), s_\beta(r')\right] = i\epsilon_{\alpha\beta\gamma}s_\gamma(r)\delta(r - r').$$

Using this spin density, the magnetization is defined by

$$M(r) = g_e\mu_B s(r) = 2ms(r),$$

where $m = g_e\mu_B/2$, where g_e and μ_B are respectively the electronic g-factor and the Bohr magneton. Again with this magnetization operator we have the commutation relation

$$\left[M^+(r), M^-(r')\right] = 4mM_z(r)\delta(r - r').$$

Here we defined $M^\pm(r) = M_x(r) \pm iM_y(r)$.

With the aid of the Holstein-Primakoff transformation [48, 49]

$$M^+(r) = \sqrt{4mM}\left(1 - \frac{m}{M}b^\dagger(r)b(r)\right)^{\frac{1}{2}}b(r),$$
$$M^-(r) = \sqrt{4mM}b^\dagger(r)\left(1 - \frac{m}{M}b^\dagger(r)b(r)\right)^{\frac{1}{2}},$$

we can approximately write the magnetizations as followings:

$$M^+(r) = \sqrt{4mM}b(r),$$
$$M^-(r) = \sqrt{4mM}b^\dagger(r),$$
$$M_z(r) = M - 2mb^\dagger(r)b(r)$$

where $M = |M|$ is assumed to be sufficiently larger than the transverse magnetization. The operator b fulfills the following relation

$$\left[b(r), b^\dagger(r')\right] = \delta(r - r'),$$

which is the manifestation of the bosonic nature of this quantum. This bosonic quantum of the magnetization oscillation is called the magnon. The operator is represented in the k-space through the Fourier transformations

$$b_{\boldsymbol{k}} = \int \mathrm{d}\boldsymbol{r} b(\boldsymbol{r}) e^{i\boldsymbol{k}\cdot\boldsymbol{r}},$$

$$b_{\boldsymbol{k}}^{\dagger} = \int \mathrm{d}\boldsymbol{r} b^{\dagger}(\boldsymbol{r}) e^{-i\boldsymbol{k}\cdot\boldsymbol{r}}.$$

These satisfy again the commutation relation $[b_{\boldsymbol{k}}, b_{\boldsymbol{k}}^{\dagger}] = \delta_{\boldsymbol{k}\boldsymbol{k}'}$. Since we are interested in the magnetostatic mode, we only consider the case $\boldsymbol{k} = \boldsymbol{0}$. We denote the magnon operator $b_{\boldsymbol{k}}$ for the magnetostatic mode simply as b. In terms of the transformed magnon operator, the magnetizations read

$$M^{+}(\boldsymbol{r}) = \sqrt{\frac{4mM}{V}} b + \mathcal{O}(\text{3rd-order terms of operators}),$$

$$M^{-}(\boldsymbol{r}) = \sqrt{\frac{4mM}{V}} b^{\dagger} + \mathcal{O}(\text{3rd-order terms of operators}),$$

$$M_z(\boldsymbol{r}) = M - \frac{2m}{V} b^{\dagger} b.$$

Here the volume of the whole sample V is present in these expressions. In the later analysis (see Sec. 4.3), we only consider the first-order terms and neglect the higher-order ones because the nonlinear effects are negligible.

3.4 Ferromagnetic resonance experiments

By now we have described the properties of the Walker modes. In this section we give a method to experimentally observe them, which is often referred to as the ferromagnetic resonance (FMR).

3.4.1 Experimental setup

In order to observe the Walker modes in the specimen, we need two things: a static magnetic field that saturates the magnetization in some direction and an oscillating magnetic field, or microwave radiation, perpendicular to the static field that resonantly excites the precession of the magnetization. Either of these two can be varied to observe the FMR, namely, the magnitude of the static magnetic flux or the frequency of the microwaves.
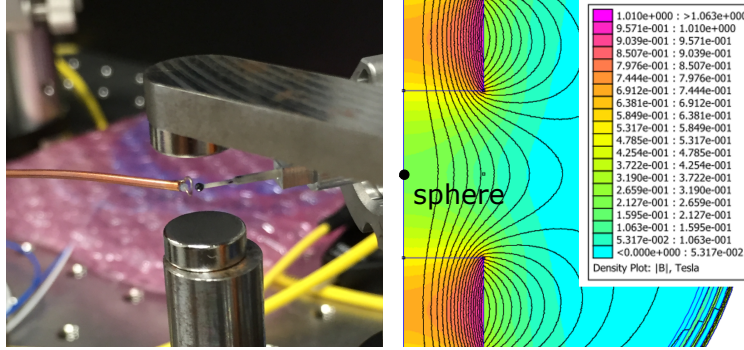
Figure 3.3: (Left panel) Picture of the FMR experiment. (Right panel) Density plot of the magnetic flux, calculated by the finite element method [50].

First, the static magnetic field applied to the YIG sphere is served by the permanent magnets. The magnetic flux generated by a pair of magnets attached to the yoke made of pure iron can be calculated by the finite element method with the freeware finite-element-method magnetics solver [50]. The result is shown in the right panel of Fig. 3.3, in which the realistic positions of cylindrical magnets (left panel of Fig. 3.3) are taken into account. The existence of the yoke is approximated by doubling the height of the magnets. Black dot indicate the position of the YIG sphere. There, the magnitude of the magnetic flux is evaluated to be 0.25 T, which will give the Kittel-mode frequency of 7 GHz. On the other side of the yoke the 500-turn electromagnetic coil is attached, enabling us to change the magnetic flux.

Secondly, we made a single-turn, micro-loop coil for the excitation of the Walker modes. The loop coil generates the magnetic field perpendicular to the plane of the loop, and this must be placed in a correct way so that the alternating field orthogonally intersects the static magnetic field. In this configuration,[2] when the frequency of the microwave sent to the loop coil is on resonance with the Walker modes, the magnetization oscillations can be driven.

3.4.2 Reflection spectrum with cylindrical magnets

With the preparation of the permanent magnets and the loop coil, all we have to do is to send microwaves to the loop coil and observe the reflected signal from it.

---

[2]Applying the microwaves in this configuration is often called the perpendicular pumping.
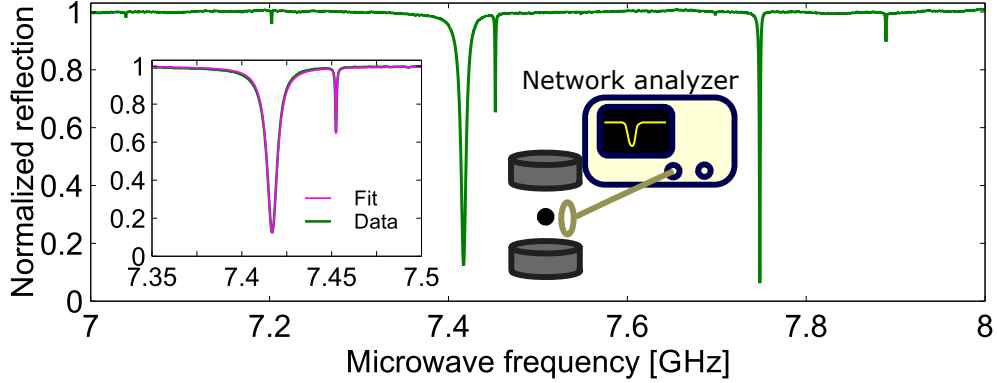
Figure 3.4: Microwave spectrum of the Walker modes in the YIG sphere with a pair of cylindrical magnets. Right inset shows the schematics of the experimental setup and the left one the result of the Lorentzian fitting.

When there is nothing absorptive around the loop coil, the impedance mismatch at the loop leads to the fully reflected signal. We use a vector network analyzer as the microwave source and the receiver, which allows us to obtain the reflection spectrum. Figure 3.4 shows the observed spectrum. First, we notice the thick and deep dip around 7.42 GHz. Since the Kittel mode is thought to have the strongest coupling to the irradiated microwaves from the loop coil, this resonance can be said to be the one resulting from the Kittel mode.[3] Other modes are higher-order magnetostatic modes whose mode indices are determined afterwards in the experiment with the variable magnetic field.

In the left inset of Fig 3.4 the resonances from the Kittel mode and another one are fitted with Lorentzian curves. For the evaluation of the intrinsic loss rate, almost the same discussion about the dynamics of the system as in the WGM case applies (see Sec. 2.4.2). Therefore we simply replace the propagating optical field and the WGM by microwave field and the Kittel mode, and the fitting results tell us that the intrinsic quality factor of the Kittel mode is 1.6×10^3. Here we again used the result of weak coupling regime, which we can confirm by changing the distance between the loop coil and the sphere.[4]

---

[3]Another dip at 7.75 GHz, which is also critically coupled, has small intrinsic loss rate. Therefore the external coupling is small.

[4]Another way to do this is to use both the amplitude and the phase of the reflected microwaves.
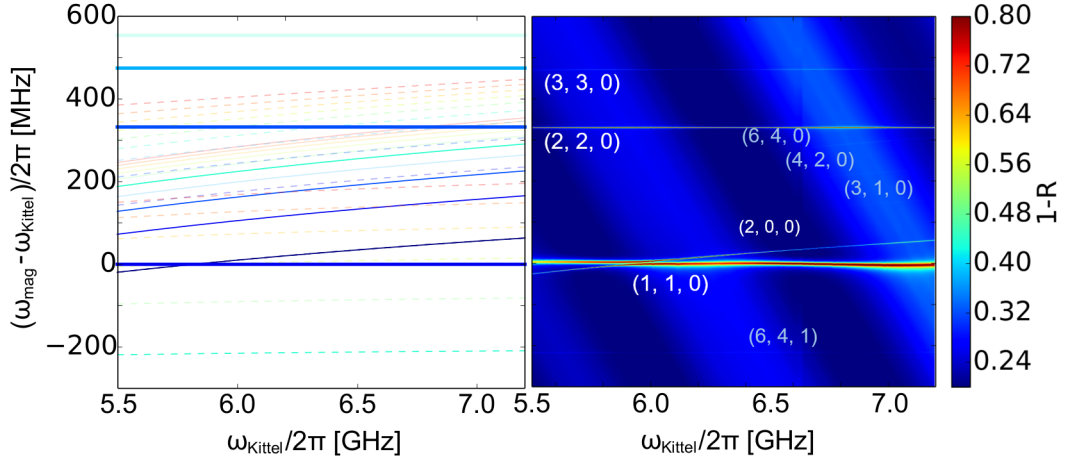
Figure 3.5: Microwave spectrum of the magnetostatic modes in the YIG sphere using a pair of cylindrical magnets with variable magnetic field. The fractional reflection subtracted from 1 is plotted.
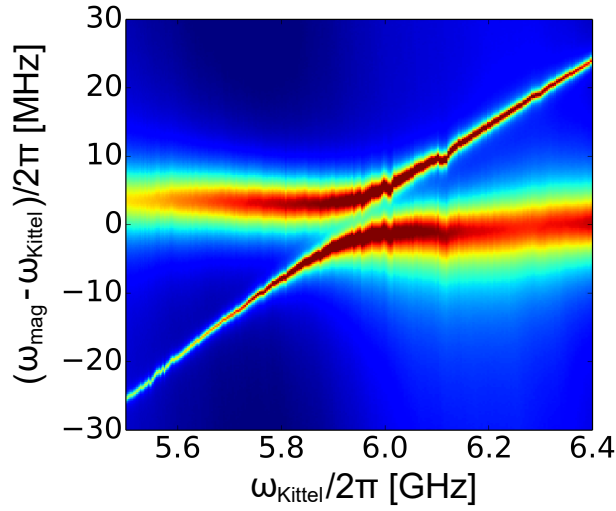

Figure 3.6: Expanded image of Fig. 3.5 around the crossing point of $(1, 1, 0)$ and $(2, 0, 0)$ modes. Color scale is the same as the original plot.

3.4.3 Identification of the Walker modes

For now we have regarded the thickest and deepest resonance as the Kittel mode. This assignment was just empirically done, however, we will be able to give some additional evidence by examining the behavior of every mode in the spectra. As we saw in Fig. 3.1, there are apparent difference among the Walker modes in the dependence of the resonance frequencies on the magnitude of the magnetic field. Roughly speaking, $(m, m, 0)$ and $(m+1, m, 0)$ modes have the linear dependence on the applied magnetic field, whereas the higher-order ones show nonlinear behaviors.

We inject current into the electromagnetic coil and change the frequencies of the Walker modes. The horizontal axis of the Fig. 3.5 is the frequency of the mode we regard as the Kittel mode. This is supposed to be the magnetic field multiplied by the gyromagnetic ratio. The common vertical axis for the left and the right panels shows the frequency difference from the Kittel mode resonance, where, of course, the mode we think as the Kittel mode always stays at zero by definition. Experimentally, we take spectra like in Fig 3.4 for each values of the injected current from $-2\,\mathrm{A}$ to $2\,\mathrm{A}$ with keeping track of the Kittel mode frequency. The collection of the reflection spectra for the various magnetic field strengths are plotted in the right panel of Fig. 3.5. There we can see several modes appear as lines and curves in this plot. For the reference, on the left the calculated frequencies of several magnetostatic modes are plotted with the same axis scales. The partially transparent curves in the left panel is not likely to be observed in the experiment, and the opaque ones show excellent match with the observed resonances and their magnetic-field dependences. From this analysis, the mode which we assumed to be the Kittel mode is evidently the one, and the higher-order modes such as $(2, 2, 0)$, $(3, 3, 0)$ and $(2, 0, 0)$ modes can be assigned with a confidence.[5]

One might notice that at around 5.9 GHz, $(2, 0, 0)$ mode intersects the Kittel mode. Figure 3.6 is the plot of the region around the crossing. We can clearly see the normal-mode splitting of the two modes.

---

[5]Some of the modes are too faint to find them immediately, though.
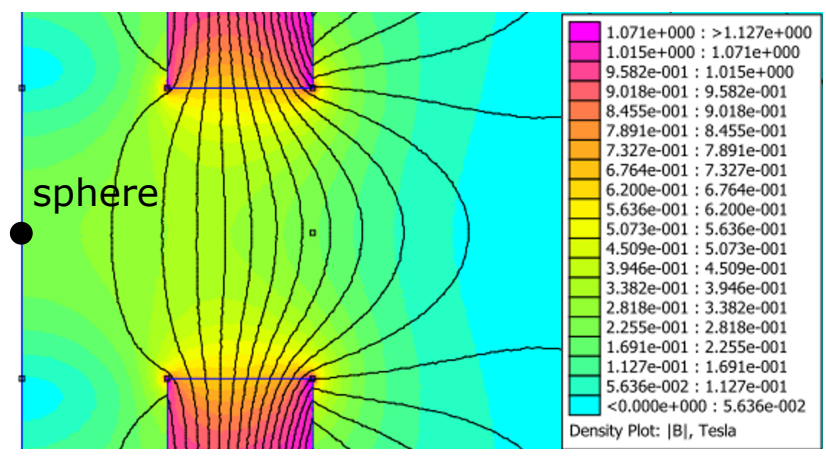
Figure 3.7: Calculated magnetic flux generated by the ring magnets with the outer and inner radius of 12 mm and 6 mm, and the thickness of 6 mm. The gap between the magnets is 6 mm.
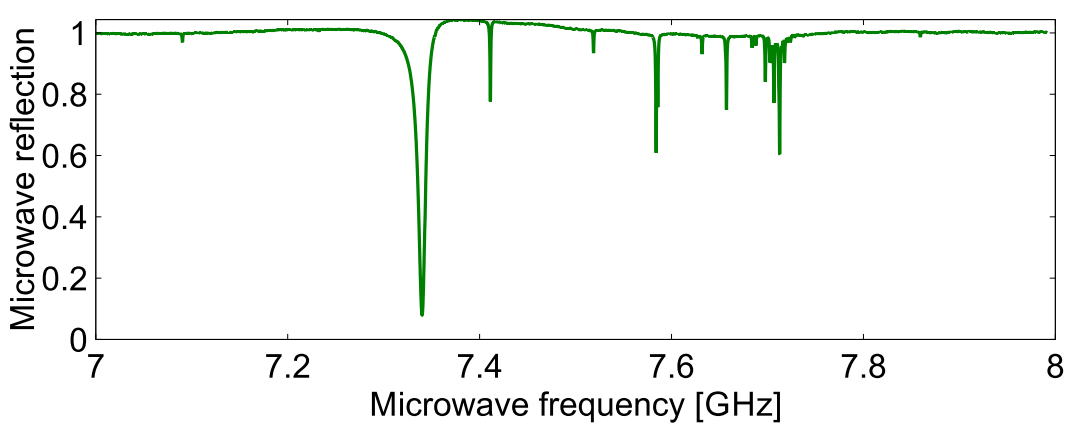
Figure 3.8: Microwave spectrum of the magnetostatic modes in the YIG sphere with a pair of ring magnets.
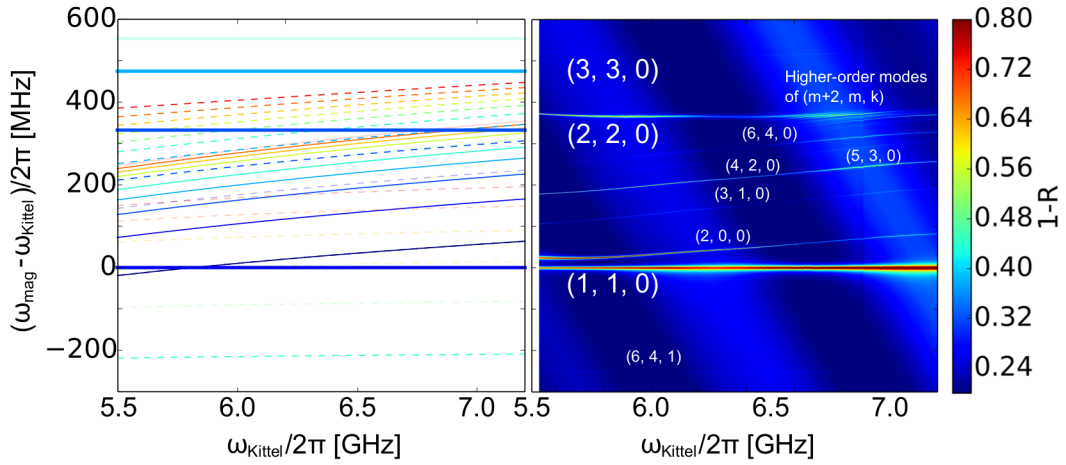
Figure 3.9: Microwave spectrum of the magnetostatic modes in the YIG sphere using a pair of ring magnets with variable magnetic field. The fractional reflection subtracted from 1 is plotted.
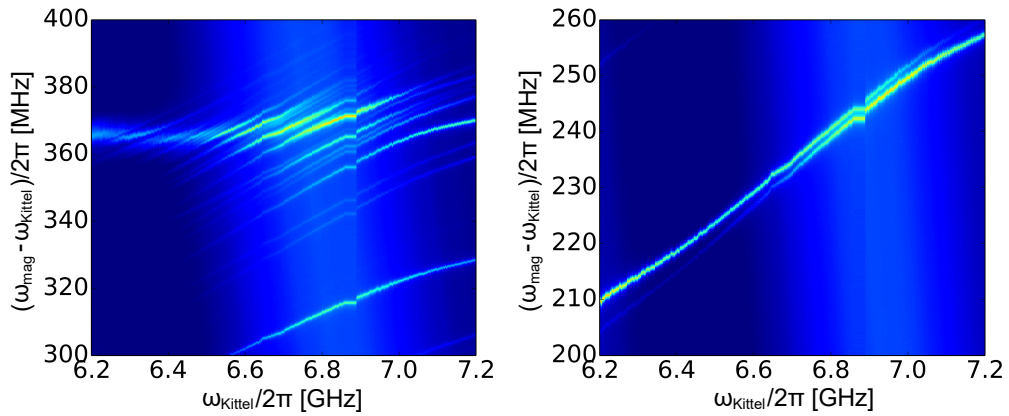
Figure 3.10: Expanded images of Fig. 3.9 around the region we can observe avoided crossings. Color scale is the same as the original plot.

3.4.4 Results with ring magnets

In order for the system of the cavity optomagnonics to be implemented, we must have the WGMs lying in the plane perpendicular to the static magnetic field, therefore the rod on which the sphere is mounted should be aligned in the same direction as that of the static magnetic field. Since the gap between the two magnets should not be large, the ring magnets are used in the Brillouin scattering experiments mentioned in the next Chapter. In prior to the microwave and optical experiments getting together, we first investigate the behavior of the magnetostatic modes with the ring magnets.

In the Fig. 3.7, the calculated magnetic field distribution is shown. In contrast to the case of the cylinder magnets shown in Fig. 3.3 (right panel), the field becomes zero at the surface of the magnets along the symmetry axis. In addition, the field inhomogeneity is slightly larger than that of the cylinder magnets. We use all the same experimental technique to observe FMR shown in Fig. 3.8. There, with the ring magnets, the number of observed resonances is larger than we found in Fig. 3.4, which seems to be due to the larger inhomogeneity of the static magnetic field and also to the slight change of the inhomogeneity of the microwave radiation from the loop coil.

The results of the dependence on the magnetic field are put in Fig. 3.9, where in the left panel the opaque Theoretical curves indicate the seemingly relevant modes in this case. Other than the increased number of the observable modes, we note two things in the spectra. One is the frequency shift of the higher-order modes and the other is that a lot of modes crosses $(2, 2, 0)$ mode at around 6.8 GHz in terms of the Kittel-mode frequency, each showing the anticrossing. We also note that the $(2, 0, 0)$ mode exhibits larger coupling with the Kittel mode to result in the observed spectrum at around 5.7 GHz. All these features are interpreted to be caused by the inhomogeneity of the static magnetic field, which seems, though it depends on the precise positioning of the sphere, inevitable to some extent with the ring magnets. The identification of each resonance in the right panel of Fig. 3.9 is done by the comparison with theoretical values in the left panel with the help of the identifications done in Fig. 3.5. The expanded plots around the regions of the anticrossings involving the $(2, 2, 0)$ (left) and the $(4, 2, 0)$ modes (right), both at around 6.7 GHz, are given in Fig. 3.10. There is a discontinuity at 6.9 GHz, which are experimental artifacts given

rise to as follows. We are changing the polarity of the injected current by simply interchanging the two connectors inserted into the power supply, and there emerges a small jump of the magnetic field. Thus these artifacts appears at the same magnetic field, i.e., at the Kittel-mode frequency.

Chapter 4

Theory of magnon-induced Brillouin scattering of light in WGM

In this Chapter we theoretically analyze the magnon-induced Brillouin scattering of light in WGMs and derive some important properties of the scattering process such as the spin and orbital angular momentum conservation. The input-output analysis with the Heisenberg's equations of motion make the densities of states of the WGMs explicitly appear in the scattering strength, that is, the microwave-to-optical photon conversion efficiency.

4.1 Optical transitions in YIG

Yttrium iron garnet is not only a good insulating ferrimagnet, but a highly transparent media for the telecommunication wavelength, too. YIG shows, moreover, large magneto-optical effects such as the Faraday effect and the Cotton-Mouton effect. These optical activities are thought to be the consequences of the strong spin-orbit coupling of the electrons inside the material. We need some details of the optical transitions involved in the magneto-optical effect for the sake of the construction of the relevant model of the magnon-induced Brillouin scattering.

The crystalline structure of YIG ($Y_3Fe_5O_{12}$) is depicted in Fig. 4.1(a) produced
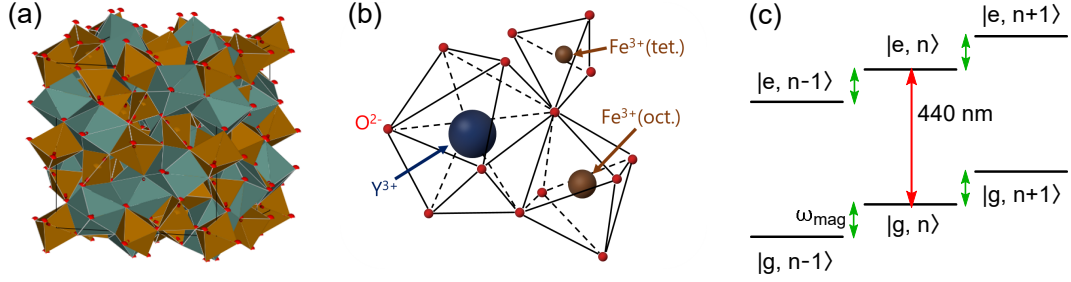
Figure 4.1: (a) Unit cell of YIG. Oxygens (red dots) form dodecahedra (green) that contains the Y^{3+} ions, and tetrahedra and octahedra (brown) containing the Fe^{3+} ions. Image is produced by VESTA [51] (b) relevant energy levels for the description of the magnon-induced Brillouin scattering, which are labeled by the electronic ground and excited states $|g\rangle$ and $|e\rangle$ with the number of magnons $|n\rangle$.

by VESTA [51]. The crystal structure belongs to the cubic space group O_h^{10}. Red dots in the figure indicate the positions of the oxygen ions. These oxygens form three kinds of polyhedra. The dodecahedral ones (green) support Y^{3+} ions inside them, and octahedral and tetrahedral ones (brown) support Fe^{3+} ions inside, which are responsible for the ferrimagnetism. Figure 4.1(b) depicts these three elements. Tremendous studies are done in the scope of explaining the optical absorption and Faraday rotation spectra of YIG [52, 53]. For now, both of the Fe^{3+} ions in the tetrahedral and the octahedral sites are considered to contribute to the magneto-optical effect. It seems that both of the crystalline field transitions and the charge transfer transitions account for the observed absorption spectrum. In terms of the Faraday rotation spectrum, Shinagawa [53] assigned the π-type charge transfer transitions to interpret the observed strength and the sign of the Faraday rotation and its dependence on the wavelength of light.

One thing in common for the interpretation of the large magneto-optical rotation in YIG is that the large spin-orbit coupling of electrons affect the excited energy levels and make σ^+- and σ^-- transitions have different strengths. More generally, we can estimate the amount of Faraday rotation by the off-diagonal elements of the permittivity tensor. The rotation angle in the transparent material is proportional to

the real part of it, which is of the form [53]

$$\sum_{m,n} \frac{(f_{mn}^+)^2 - (f_{mn}^-)^2}{(\omega_{mn}^2 - \omega^2 + \gamma_{mn}^2)^2 + (2\omega\gamma_{mn})^2}$$

where $f_{mn}^\pm$ represents the oscillator strength between the energy levels $n \to m$ for the $\sigma^\pm$ polarization, ω_{mn} the transition angular frequency, γ_{mn} the decay rate from m to n levels, and ω the angular frequency of the incident laser angular frequency. Since the absorption band of YIG is situated above 2 eV, the laser we inject, which has the energy of about $\hbar \times 200$ THz $= 0.82$ eV, is far detuned from the relevant transitions. In this situation, the detailed structure of the ground and excited manifolds can be neglected and the approximation of the transition by a two-level system is allowed. To involve magnons in the energy scheme explicitly, we just add copies of the two-level system where each is endowed with the number of magnons. These two-level systems have different energies corresponding to the number of magnons, as drawn in Fig. 4.1(c). Thus, such a ladder of energy levels is constructed as modeling the Brillouin scattering. Optical transitions can be considered with this. The difference of the transition strengths for the two circular polarizations is properly treated later in the Chapter 5.

4.2 Interaction between WGMs and Walker mode

We study the interaction between the light in WGMs and the Walker mode through the calculation of the energy $E = \int \mathcal{E}(\boldsymbol{r}, t) \mathrm{d}t \mathrm{d}V$. The condition for the integral
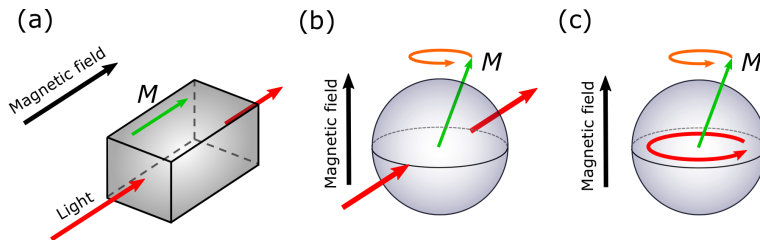

Figure 4.2: Schematic pictures of the experiments for the observation of the (a) conventional Faraday effect, (b) the magnon-induced Brillouin scattering of propagating optical mode, and (c) the magnon-induced Brillouin scattering of light in WGMs.

to be non-vanishing leads to some important properties of the Brillouin scattering including the angular momentum selection rules. First of all, we have the energy density $\mathcal{E} = \boldsymbol{E}^* \epsilon \boldsymbol{E}$, where the permittivity tensor ϵ including the Faraday effect is represented in Cartesian coordinates as [49]

$$\epsilon = \epsilon_0 \begin{pmatrix} \epsilon_r & -ifM_z & ifM_y \\ ifM_z & \epsilon_r & -ifM_x \\ -ifM_y & ifM_x & \epsilon_r \end{pmatrix}. \tag{4.1}$$

If the magnetization is directed along the x-axis and the plane-wave light also propagates along this, as in the Fig. 4.2(a), one will find the permittivity tensor is easily diagonalized in the circular polarization basis, with different indices of refraction between the two circularly polarized light.

In order to observe the magnon-induced Brillouin scattering as the Faraday effect caused by the transverse magnetization, one might have a setup like in the Fig. 4.2(b), in which the saturated magnetization in z-direction is perpendicular to the direction of the propagation of light and the transverse component of the magnetization is seen by the light. In this case, one can again get diagonalized permittivity tensor and the difference is that the static magnetization is replaced by the oscillating, transverse magnetization. Along this line, Hisatomi *et. al.* [8] observed the coherent, bidirectional microwave-light conversion.

In our case, with the plane wave replaced by the WGM light [see Fig. 4.2(c)], the situation is somewhat complicated. Fortunately we have the analytical solutions of WGMs supported by a sphere in spherical coordinates (see Chapter 2). Transformation of a set of basis vectors $\{\boldsymbol{e}_x, \boldsymbol{e}_y, \boldsymbol{e}_z\}$ into those in a polar coordinates $\{\boldsymbol{e}_r, \boldsymbol{e}_\theta, \boldsymbol{e}_\phi\}$ is done with an elementary linear algebra. Using some orthogonal matrix U, the permittivity tensor in spherical coordinates can be represented by $\epsilon_{\text{polar}} = U^{-1}\epsilon U$. Hereafter we denote ϵ_{polar} simply as ϵ. After some math we get the explicit form of the permittivity tensor as

$\epsilon =$

$$\epsilon_0 \begin{pmatrix} \epsilon_r & if(M_x \sin\phi - M_y \cos\phi) & 0 \\ -if(M_x \sin\phi - M_y \cos\phi) & \epsilon_r & -if(M_x \cos\phi + M_y \sin\phi) \\ 0 & if(M_x \cos\phi + M_y \sin\phi) & \epsilon_r \end{pmatrix},$$

$$\tag{4.2}$$

where we assumed the magnetization is saturated in z-direction and neglect it because it does not contribute to the inelastic scattering.

Now we would like to calculate the energy E with the aid of the expressions of the permittivity tensor, the TE and the TM WGMs [Eqs. (2.12) and (2.13)] and the transverse magnetization of the Walker modes (Table 3.1). The integrand or the interaction energy density is

$$
\mathcal{E} = \left(E_{l_{\mathrm{TM}}m_{\mathrm{TM}}}^{(\mathrm{TM})*} e^{\mp i m_{\mathrm{TM}}\phi} \quad 0 \quad \mp i E_{l_{\mathrm{TM}}m_{\mathrm{TM}}}^{(\mathrm{TM})*} e^{\mp i m_{\mathrm{TM}}\phi} \right) \epsilon \begin{pmatrix} 0 \\ E_{l_{\mathrm{TE}}m_{\mathrm{TE}}}^{(\mathrm{TE})} e^{\pm i m_{\mathrm{TE}}\phi} \\ 0 \end{pmatrix}
$$

$$
= \epsilon_0 \begin{pmatrix} 1 & 0 & \mp i \end{pmatrix} \begin{pmatrix} i f (M_x \sin\phi - M_y \cos\phi) \\ \epsilon_r \\ i f (M_x \cos\phi + M_y \sin\phi) \end{pmatrix} E_{\mathrm{TM}}^* E_{\mathrm{TE}} e^{\pm i(m_{\mathrm{TE}}-m_{\mathrm{TM}})\phi}
$$

$$
= i\epsilon_0 f \left(M_x \sin\phi - M_y \cos\phi \mp i M_x \cos\phi \mp i M_y \sin\phi \right) E_{\mathrm{TM}}^* E_{\mathrm{TE}} e^{\pm i(m_{\mathrm{TE}}-m_{\mathrm{TM}})\phi}
$$

$$
= \pm \epsilon_0 f \left(M_x e^{\pm i\phi} \mp i M_y e^{\pm i\phi} \right) E_{\mathrm{TM}}^* E_{\mathrm{TE}} e^{\pm i(m_{\mathrm{TE}}-m_{\mathrm{TM}})\phi}
$$

$$
= \pm \epsilon_0 f \left(M_x \mp i M_y \right) E_{\mathrm{TM}}^* E_{\mathrm{TE}} e^{\pm i(m_{\mathrm{TE}}-m_{\mathrm{TM}}+1)\phi}.
$$

Note that the upper and lower signs correspond respectively to the CW and CCW orbit of WGM. The reason we multiply the permittivity tensor by the TE and the TM mode is that the terms with two TE or two TM modes vanish. This is the consequence of the spin angular momentum conservation in the system including light and magnon. At this point, the remaining task is to insert the concrete expression of $(M_x \mp i M_y)$. Here for instance, we consider the $(m+1, m+1, 0)$ Walker mode from which one immediately see that $(M_x \mp i M_y) = M_\perp r^m e^{\pm i m\phi}$, where $M_\perp = \sqrt{M_x^2 + M_y^2}$.[1] Thus we have one of the non-vanishing terms of the energy density

$$
\mathcal{E} = \pm \epsilon_0 f r^m M_\perp E_{\mathrm{TM}}^* E_{\mathrm{TE}} e^{\pm i(m_{\mathrm{TE}}-m_{\mathrm{TM}}+m+1)\phi} e^{\pm i(\omega_{\mathrm{TE}}-\omega_{\mathrm{TM}}\pm\omega_m)t}. \tag{4.3}
$$

Note that the time dependent factor is revived in the above expression.

It is noteworthy that the variables ϕ and t are completely separated in the two exponential factors. The remaining factors are the functions of only r and θ. Therefore, when integrated over time and space, two exponential factors give two delta functions

---

[1] In the interaction with WGMs, it is justified to assume $\theta = \pi/2$ for the Walker modes.

Figure 4.3: Schematic representation of the energy levels involved in the magnon-induced Brillouin scattering. This is the case when we consider the inner part of the WGMs.

$\delta(\omega_{\mathrm{TE}} - \omega_{\mathrm{TM}} \pm \omega_m)$ and $\delta(m_{\mathrm{TE}} - m_{\mathrm{TM}} + m + 1)$. The first one leads to the energy conservation

$$\omega_{\mathrm{TE}} - \omega_{\mathrm{TM}} \pm \omega_m = 0. \tag{4.4}$$

This implies the conservation of the spin angular momentum and hence only a single optical sideband is generated in each process. The second results in the conservation of the orbital angular momentum

$$m_{\mathrm{TE}} - (m_{\mathrm{TM}} - 1) + m = 0. \tag{4.5}$$

This relation is revealed to be very crucial. We will revisit this condition later.

Since the laser is far-detuned from the electronic transition, the transition can be approximately regarded as that in the ladder of the two-level systems, as we saw in the previous Section. The relevant transitions are depicted in Fig. 4.3. Convention of the polarization should be clear from here. In the usual sense, $\sigma^{\pm}$ polarized light has ± 1 spin, and when it is absorbed by a matter, the spin ± 1 is transferred to it. In the case of magnon-induced Brillouin scattering, a single magnon excitation is equal to the *reduction* of the total spin by 1. We shall thus denote the circular polarizations associated with the magnon creation and annihilation as $\tilde{\sigma}^+ \ (= \sigma^-)$ and $\tilde{\sigma}^- \ (= \sigma^+)$,
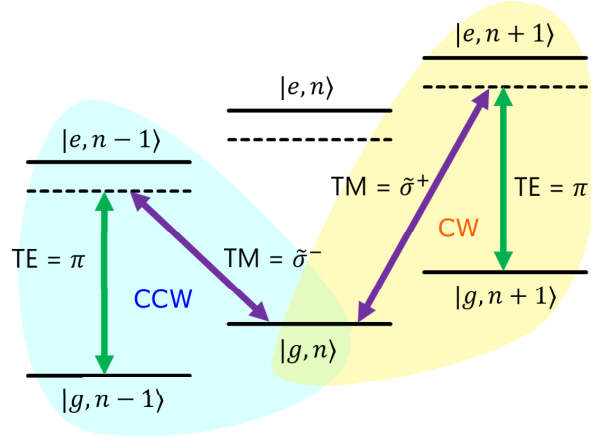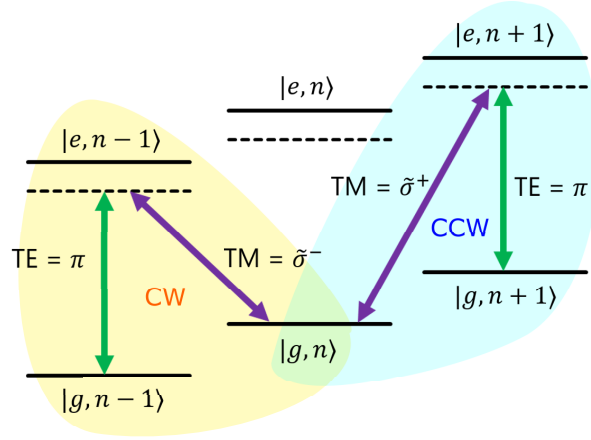
Figure 4.4: Schematic representation of the energy levels involved in the magnon-induced Brillouin scattering. This is the case when we consider the outer component of the WGMs.

respectively. With these notations, the CW and the CCW WGMs have the $\tilde{\sigma}^+$ and the $\tilde{\sigma}^-$ polarizations, respectively.

The effect of the "outer" polarization component

In Eq. (2.13), the simplification [Eq. 2.6] is made that only one circular polarization component is taken into account. However, it will be revealed later that the effect resulting from the other circular polarization component should be taken into account. This can be described by

$$\boldsymbol{E}_{lm}^{(\text{TM})} = E_{lm}^{(\text{TM})} e^{\pm im\phi} (\boldsymbol{e}_r \mp i\boldsymbol{e}_\phi) \tag{4.6}$$

$$= E_{lm}^{(\text{TM})} e^{\pm i(m-1)\phi} (\boldsymbol{e}_x \mp i\boldsymbol{e}_y). \tag{4.7}$$

Again the upper and the lower signs represent the case of the CW and the CCW orbits of WGM, respectively. In this case, the conservation of the energy and the orbital angular momentum should be modified:

$$\omega_{\text{TE}} - \omega_{\text{TM}} \mp \omega_m = 0 \tag{4.8}$$

$$m_{\text{TE}} - (m_{\text{TM}} + 1) - m = 0. \tag{4.9}$$

Note that the conditions (4.5) and (4.9) are written in terms of the mode indices, which do not coincide the orbital angular momentum for the TM WGM [see Eqs. (2.13) and

53

Quantities	Symbols
Frequencies of WGMs and magnon mode	$\Omega_{\text{TE/TM}}, \Omega_{\text{m}}$
Intrinsic decay rate of WGMs and magnon mode	$\gamma_{\text{TE/TM}}, \gamma_{\text{m}}$
Annihilation operator of WGMs	$a_{\text{TE/TM}}$
Aannihilation operator of magnon mode	b
Frequency of the fields for WGMs and magnon mode	$\omega_{\text{TE/TM}}, \omega_{\text{m}}$
External coupling to WGMs and Kittel mode	$\kappa_{\text{TE/TM}}, \kappa_{\text{m}}$
Annihilation operators of fields into/from WGM photon	$A_{\text{TE/TM}}^{(\text{in})/(\text{out})}$
Annihilation operators of fields into/from magnon mode	$B^{(\text{in})/(\text{out})}$
Intra-cavity photon number of WGMs	$n_{\text{TE/TM}}$
Photon flux into/from WGMs	$n_{\text{TE/TM}}^{(\text{in})/(\text{out})}$
Photon flux into/from magnon mode	$n_{\text{MW}}^{(\text{in})/(\text{out})}$
Interaction Hamiltonian for CW and CCW cases	$\mathcal{H}_{\text{int}}^{(\text{CW/CCW})}$
Detuning from the WGM resonance, $\Omega_{\text{TE/TM}} - \omega_{\text{TE/TM}}$	$\Delta_{\text{TE/TM}}$
Detuning from the magnon-mode resonance, $\Omega_{\text{m}} - \omega_{\text{m}}$	Δ_{m}
$\gamma_{\text{TE}} + \kappa_{\text{TE}}, \gamma_{\text{TM}} + \kappa_{\text{TM}}, \gamma_{\text{m}} + \kappa_{\text{m}}$	$\Gamma_{\text{TE}}, \Gamma_{\text{TM}}, \Gamma_{\text{m}}$
Coupling coefficient of the Brillouin scattering	g

Table 4.1: Symbols used in the model. Superscripts (in) and (out) stands for the quantities of input and output fields. Subscripts TE and TM denotes those of TE and TM WGMs.

(4.7)]. The relevant optical transitions for these cases are depicted in Fig. 4.4. For the sake of the convenience, we call this opposite polarization component, which originating in the outer part of WGMs inside the resonator, as the *outer* component, whereas the *inner* component refers to the one that comes from the inner part of WGMs considered before.

4.3 Input-output formulation of the system

4.3.1 Interaction Hamiltonian and coupling strength

The calculation given in the previous section is helpful for the understandings of the system, especially in terms of the conservation of the energy or the spin angular momentum [Eqs. (4.4) and (4.8)] and the orbital angular momentum [Eqs. (4.5) and (4.9)]. However, the treatment is still unsatisfactory in the sense that the effect of the densities of states of the WGMs are not apparent. In order to accommodate this, we now have to consider the detailed dynamics of the Walker mode and the two WGMs. The schematic picture of the whole system is depicted in Fig. 4.5. The notations for the current analysis are listed in the Table. 4.1. The way we analyze the dynamics of the fields relies on the Heisenberg's equation of motion for an operator $\mathcal{O}$

$$\frac{\mathrm{d}\mathcal{O}}{\mathrm{d}t} = \frac{i}{\hbar}\left[\mathcal{H}, \mathcal{O}\right].$$

According to the discussion in the last section, the interaction Hamiltonians read

$$\mathcal{H}_{\mathrm{int}}^{(\mathrm{CW})} = \hbar g(a_{\mathrm{TE}}a_{\mathrm{TM}}^{\dagger}b + a_{\mathrm{TE}}^{\dagger}a_{\mathrm{TM}}b^{\dagger}), \tag{4.10}$$

$$\mathcal{H}_{\mathrm{int}}^{(\mathrm{CCW})} = \hbar g(a_{\mathrm{TE}}a_{\mathrm{TM}}^{\dagger}b^{\dagger} + a_{\mathrm{TE}}^{\dagger}a_{\mathrm{TM}}b), \tag{4.11}$$

respectively for the inner polarization of the CW and the CCW WGMs. For the outer polarization, we simply exchange the right-hand-sides of the interaction Hamiltonians for the CW and the CCW cases, since the polarization of the TM mode is reversed. In the following calculations, we limit our consideration to the case of the CW WGMs for brevity.

The interaction Hamiltonian of Eq. (4.10) can also be obtained by considering the volume integration of the interaction-energy density (4.3), that is,

$$-i\epsilon_0 f M_{\perp} E_{\mathrm{TM}}^* E_{\mathrm{TE}} \tag{4.12}$$

and its complex conjugate with exponential factors not being shown. The coefficient f originates in the permittivity tensor describing the magneto-optical effect [49]. In a saturated ferromagnet the coefficient f is related to the Verdet constant $\mathcal{V}$ as $f = (2\sqrt{\epsilon_r}/k_0 M_S)\mathcal{V}$ [49] with the wavevector k_0 of the optical field in the vacuum.

The three quantities, $M_{\perp}$, E_{TM} and E_{TE}, are now translated into the operators b, a_{TM} and a_{TE} with some coefficients to give interaction terms $\hbar g a_{\mathrm{TE}}a_{\mathrm{TM}}^{\dagger}b$ and its
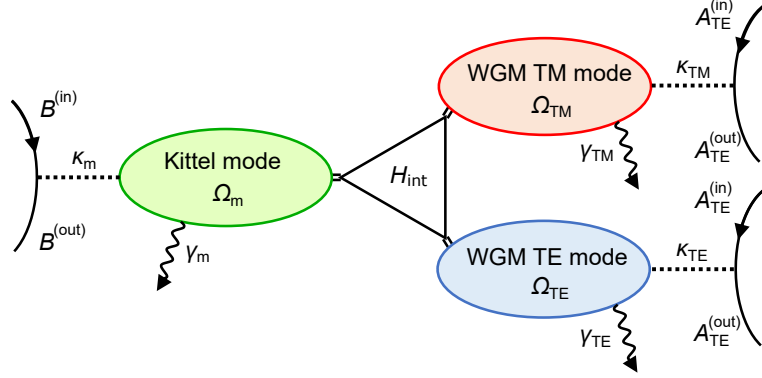
Figure 4.5: Schematic picture of the system under consideration. The two WGMs and magnon mode are interconnected by the interaction Hamiltonian. The symbols used here are listed in Table 4.1.

Hermitian conjugate. The pre-factors for the operators b, a_{TM} and a_{TE} are written respectively by $\sqrt{2g_s\mu_{\mathrm{B}}M_S/V}$, $\sqrt{\hbar\Omega_{\mathrm{TM}}/2\epsilon_0\epsilon_r V_{\mathrm{TM}}}$ and $\sqrt{\hbar\Omega_{\mathrm{TE}}/2\epsilon_0\epsilon_r V_{\mathrm{TE}}}$, where the sample volume V, the mode volumes V_{TM} and V_{TE} of TM and TE WGMs, the electronic g-factor g_s and the Bohr magneton μ_{B} are used. Suppose $\Omega_{\mathrm{TM}} \simeq \Omega_{\mathrm{TE}} \equiv \Omega$ and $V_{\mathrm{TM}} = V_{\mathrm{TE}} \equiv V_{\mathrm{WGM}}$, and the volume integration runs over the interaction region to give a factor of V_{WGM}. Thus, we get the theoretical expression $g^{(\mathrm{theory})}$ for the coupling strength

$$g^{(\mathrm{theory})} = \frac{1}{\hbar}\epsilon_0 f V_{\mathrm{WGM}} \sqrt{\frac{2g_s\mu_{\mathrm{B}}M_S}{V}} \sqrt{\frac{\hbar\Omega_{\mathrm{TM}}}{2\epsilon_0\epsilon_r V_{\mathrm{TM}}}} \sqrt{\frac{\hbar\Omega_{\mathrm{TE}}}{2\epsilon_0\epsilon_r V_{\mathrm{TE}}}} = \mathcal{V}\frac{c}{n_r}\sqrt{\frac{2}{n_{\mathrm{spin}}V}} \quad (4.13)$$

where c denotes the speed of light, n_{spin} the spin density and $n_r = \sqrt{\epsilon_r}$. In the above expression we used the relation $M_S = g_s\mu_B n_{\mathrm{spin}}$. Alternatively, with the speed of light inside the material c' and the number of spins $N_{\mathrm{spin}} = n_{\mathrm{spin}}V$ we can also write this in the suggestive form:

$$g^{(\mathrm{theory})} = \mathcal{V}c'\sqrt{\frac{2}{N_{\mathrm{spin}}}}. \quad (4.14)$$

This expression implies that the optomagnonical coupling is proportional to the Verdet constant $\mathcal{V}$ and furthermore the spin fluctuation appears in the form of $\sqrt{1/N_{\mathrm{spin}}}$, as we expect. This quantity can also be regarded as the Faraday rotation angle per unit time due to the vacuum fluctuation of the Walker mode.

56

In the case of our experiment, with the Verdet constant $\mathcal{V} = 3.77$ rad/cm, the spin density $n_{\mathrm{spin}} = 2.1 \times 10^{28}$ /m^3, the sample volume $V = (4\pi/3) \times (0.375)^3$ mm^3, and the refractive index $n_r = 2.19$, the theoretical coupling strength $g^{(\mathrm{theory})}$ is evaluated to be $2\pi \times 5.4$ Hz.

4.3.2 Steady-state solution of the equations of motion

It is not difficult to get equations of motion for the operators, because we already have the Hamiltonian of the whole system

$$\mathcal{H} = \hbar\Omega_{\mathrm{TE}}a_{\mathrm{TE}}^{\dagger}a_{\mathrm{TE}} + \hbar\Omega_{\mathrm{TM}}a_{\mathrm{TM}}^{\dagger}a_{\mathrm{TM}} + \hbar\Omega_{\mathrm{m}}b^{\dagger}b + \hbar g(a_{\mathrm{TE}}a_{\mathrm{TM}}^{\dagger}b + a_{\mathrm{TE}}^{\dagger}a_{\mathrm{TM}}b^{\dagger}) \quad (4.15)$$

which is the sum of the energy of three modes and the interaction Eq. (4.10). Suppose that the TM mode is driven by a laser with the frequency ω_{TM}. This allows us to replace a_{TM} with a classical field $\sqrt{n_{\mathrm{TM}}}e^{-i\omega_{\mathrm{TM}}t}$, where $n_{\mathrm{TM}} = n_{\mathrm{TM}}^{(\mathrm{in})}\kappa_{\mathrm{TM}}/\left[\Delta_{\mathrm{TM}}^2 + (\Gamma_{\mathrm{TM}}/2)^2\right]$ denotes the average number of photons in the TM WGM. Here we moved to a rotating frame by performing the unitary transformation

$$u(t) = \exp\left[i\omega_{\mathrm{TM}}a_{\mathrm{TM}}^{\dagger}a_{\mathrm{TM}}t + i\omega_{\mathrm{TE}}a_{\mathrm{TE}}^{\dagger}a_{\mathrm{TE}}t + i\omega_{\mathrm{m}}b^{\dagger}b\,t\right]$$

which transforms the Hamiltonian in the form

$$\begin{aligned} \mathcal{H} &= u^{\dagger}(t)\mathcal{H}u(t) \\ &= \hbar\Delta_{\mathrm{TE}}a_{\mathrm{TE}}^{\dagger}a_{\mathrm{TE}} + \hbar\Delta_{\mathrm{TM}}a_{\mathrm{TM}}^{\dagger}a_{\mathrm{TM}} + \hbar\Delta_{\mathrm{m}}b^{\dagger}b + \hbar g\sqrt{n_{\mathrm{TM}}}(a_{\mathrm{TE}}b\,e^{i\delta t} + a_{\mathrm{TE}}^{\dagger}b^{\dagger}e^{-i\delta t}). \end{aligned}$$
$$(4.16)$$

There appears the factor $e^{i\delta t}$, which imposes the frequency matching condition $\delta \equiv \omega_{\mathrm{TM}} - \omega_{\mathrm{TE}} - \omega_{\mathrm{m}} = 0$. As a result we obtain a set of equations of motion with the dissipation and the noise terms [3]:

$$\frac{\mathrm{d}a_{\mathrm{TE}}^{\dagger}}{\mathrm{d}t} = i\Delta_{\mathrm{TE}}a_{\mathrm{TE}}^{\dagger} + ig\sqrt{n_{\mathrm{TM}}}b - \frac{\Gamma_{\mathrm{TE}}}{2}a_{\mathrm{TE}}^{\dagger} - \sqrt{\kappa_{\mathrm{TE}}}A_{\mathrm{TE}}^{(\mathrm{in})}(t), \qquad (4.17)$$

$$\frac{\mathrm{d}b}{\mathrm{d}t} = -i\Delta_{\mathrm{m}}b - ig\sqrt{n_{\mathrm{TM}}}a_{\mathrm{TE}}^{\dagger} - \frac{\Gamma_{\mathrm{m}}}{2}b - \sqrt{\kappa_{\mathrm{m}}}B^{(\mathrm{in})}(t). \qquad (4.18)$$

We can adiabatically eliminate the TE WGM, assuming that Γ_{TE} is the largest value in the situation considered. Substituting the steady-state solution of Eq. (4.17) into Eq. (4.18) and neglecting the term including $A_{\mathrm{TE}}^{(\mathrm{in})}$, we obtain

$$\frac{\mathrm{d}b}{\mathrm{d}t} = -\left(i\Delta_{\mathrm{m}} + \frac{\Gamma_{\mathrm{m}}}{2}\right)b - \frac{g^2 n_{\mathrm{TM}}}{-i\Delta_{\mathrm{TE}} + (\Gamma_{\mathrm{TE}}/2)}b - \sqrt{\kappa_{\mathrm{m}}}B^{(\mathrm{in})}(t). \qquad (4.19)$$

At this stage, we consider the steady state of the Walker mode b. Then, the coupled equations can be solved thoroughly to obtain the expression of $a_{\text{TE}}^{\dagger}$ as

$$a_{\text{TE}}^{\dagger} = ig\sqrt{n_{\text{TM}}} \frac{1}{i\Delta_{\text{TE}} - (\Gamma_{\text{TE}}/2)} \frac{\sqrt{\kappa_{\text{m}}}}{i\Delta_{\text{m}} + (\Gamma_{\text{m}}/2)} B^{(\text{in})},$$

where we assume that the coupling is weak, i.e., $g^2 n_{\text{TM}} \ll \Gamma_{\text{TM}}\Gamma_{\text{m}}$. To quantify the scattered TE-mode photon flux, the input-output relation $A_{\text{TE}}^{(\text{out})} = \sqrt{\kappa_{\text{TE}}} a_{\text{TE}}$ is invoked. With this we can express the scattered photon flux as

$$n_{\text{TE}}^{(\text{out})} = g^2 \rho_{\text{TE}}(\omega_{\text{TM}} - \omega_{\text{m}})\rho_{\text{TM}}(\omega_{\text{TM}})\rho_{\text{m}}(\omega_{\text{m}})n_{\text{TM}}^{(\text{in})}(n_{\text{MW}}^{(\text{in})} + 1). \tag{4.20}$$

with the densities of states defined by

$$\rho_{\text{TE}}(\omega_{\text{TE}}) = \frac{\kappa_{\text{TE}}}{\Delta_{\text{TE}}^2 + (\Gamma_{\text{TE}}/2)^2}$$

$$\rho_{\text{TM}}(\omega_{\text{TM}}) = \frac{\kappa_{\text{TM}}}{\Delta_{\text{TM}}^2 + (\Gamma_{\text{TM}}/2)^2}$$

$$\rho_{\text{m}}(\omega_{\text{m}}) = \frac{\kappa_{\text{m}}}{\Delta_{\text{m}}^2 + (\Gamma_{\text{m}}/2)^2}.$$

Thus, considering the contribution of every WGM labeled by i in an FSR, we derive the scattering strength for the TM-mode input as $I_{\text{TM}\rightarrow\text{TE}}(\omega) \equiv \sum_i C_i \rho_{\text{TE}}^{(i)}(\omega - \omega_{\text{mag}})\rho_{\text{TM}}^{(i)}(\omega)$ with the mode indices i and coefficients C_i which include the coupling coefficients, the Kittel mode's density of state, and the input photon flux. A similar procedure in the case of the TE-mode input results in the expression of the scattered photon flux

$$n_{\text{TM}}^{(\text{out})} = g^2 \rho_{\text{TE}}(\omega_{\text{TE}})\rho_{\text{TM}}(\omega_{\text{TE}} + \omega_{\text{m}})\rho_{\text{m}}(\omega_{\text{m}})n_{\text{TE}}^{(\text{in})}n_{\text{MW}}^{(\text{in})}. \tag{4.21}$$

and the scattering strength for the TM-mode input $I_{\text{TE}\rightarrow\text{TM}}(\omega) \equiv \sum_i C_i \rho_{\text{TE}}^{(i)}(\omega)\rho_{\text{TM}}^{(i)}(\omega + \omega_{\text{mag}})$.

4.3.3   Relevant scattering process

Up to here, all of the fundamental features in considering the magnon-induced Brillouin scattering have shown up. First, the energy conservation law (4.4) or (4.8) which includes the spin angular momentum conservation is the most rigid one. If a photon with some fixed frequency is coupled to a WGM and then scattered by a magnon, the frequency of the scattered photon is determined by this condition. Next,

Case	TM-mode	Transitions	OAM conservation	m_{TM}
CW & inner	$\tilde{\sigma}^+$	Fig. 4.3	$m_{\text{TE}} - m_{\text{TM}} + m + 1 = 0$	$m_{\text{TE}} + 1$
CCW & inner	$\tilde{\sigma}^-$	Fig. 4.3	$m_{\text{TE}} - m_{\text{TM}} + m + 1 = 0$	$m_{\text{TE}} + 1$
CW & outer	$\tilde{\sigma}^-$	Fig. 4.4	$m_{\text{TE}} - m_{\text{TM}} - m - 1 = 0$	$m_{\text{TE}} - 1$
CCW & outer	$\tilde{\sigma}^+$	Fig. 4.4	$m_{\text{TE}} - m_{\text{TM}} - m - 1 = 0$	$m_{\text{TE}} - 1$

Table 4.2: Table of the behavior of Brillouin scattering in the four cases, which are listed in the "Case" column. Each case is written in the way "(CW or CCW orbit) & (inner or outer polarization component)". The second column shows the TM-mode polarization. The figures representing the relevant transitions are listed in the third column. In the fourth, the conditions of the orbital angular momenta (OAM) conservation are listed. The fifth column indicates the m_{TM} for the case of TE-mode input scattered by the $m = 0$ (Kittel-mode) magnon.

the formulae like Eqs. (4.20) and (4.21) state that the scattering strength depends on the density of states of the input and the output WGMs. Given the input WGM, the output WGM is selected by the conservation of the orbital angular momentum (4.5) or (4.9). Therefore the output WGM depends on the orbital angular momentum m of the specific Walker mode under consideration. These three, the spin angular momentum conservation, the orbital angular momentum conservation, and the cavity density of states, interplay to results in the nontrivial behaviors of the Brillouin scattering. The possible cases of the scattering process are listed in Table. 4.3.3. The Brillouin scattering strengths for the four cases in the table can be separately evaluated (see Appendix A). The contributions by the inner and the outer components should be summed for the CW or the CCW case for the analysis of the nonreciprocity.

Chapter 5

Observation of Brillouin scattering of light in WGM with a tapered nanofiber

As described in the earlier Chapters, we succeeded in observation of the WGMs and examination of the Walker modes, both hosted in the YIG sphere. In this Chapter, we investigate the magnon-induced Brillouin scattering of light in the WGMs. We limit the situation to the case that the Kittel mode, the uniform Walker mode, is involved. The tapered optical nanofiber is used for the coupling to the WGMs in the YIG sphere. The Brillouin scattering by the Kittel mode is successfully observed, associated with the Stokes/anti-Stokes scattering asymmetry and the nonreciprocity. According to the theory developed in the previous chapter, these features are interpreted successfully in terms of the spin and the orbital angular momentum conservation. The conversion efficiency from microwave to optical photon is experimentally evaluated. From this value we can extract the optomagnonical coupling constant, which is compared with the theoretical expectation. The deviation from the theory is found for the coupling constant and the possible origins are discussed.
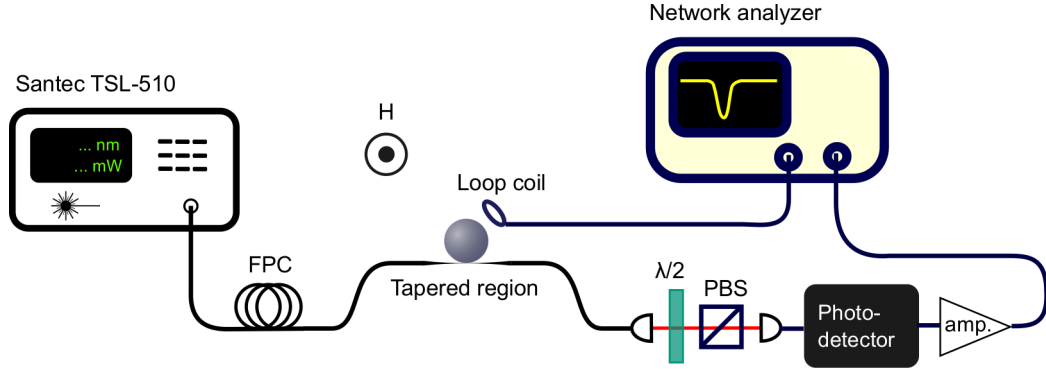
Figure 5.1: Experimental setup for the observation of the Brillouin scattering by the Kittel mode. WGMs are coupled via a tapered optical nanofiber. The scattered and the unscattered light are made interfere throughout a half-wave plate ("$\lambda/2$") and a polarization beam splitter (PBS). A network analyzer send microwaves to a loop coil and collect the signal from the high-speed photodetector.

5.1 Observation of Brillouin scattering by Kittel mode

Now we are to combine the experimental setups for the observation of the WGMs and the FMR together to see the consequences of the magnon-induced Brillouin scattering of light in the WGMs. The whole setup is depicted in the Fig. 5.1. As has been mentioned earlier in Chapter 3, we use two ring magnets to apply static magnetic field to a YIG sphere whose diameter is 0.75 μm. The Kittel-mode magnons are excited by microwaves sent from a network analyzer to a loop coil in the vicinity of the sphere. Laser light of the wavelength 1.5 μm passes through a fiber polarization controller (FPC) and go into the tapered region of a nanofiber to couple to the WGMs in the YIG sphere. The frequency of the laser is tuned on one of the WGM resonances. In the magnon-induced Brillouin scattering process, the TE (TM) WGM photon is expected to be scattered into the TM (TE) WGM and coupled back into the nanofiber. This results in the 90-degree rotation of the polarization of the scattered photon. The transmitted input photon and the scattered photon with the frequency shift by the Kittel-mode frequency interfere to exhibit the oscillation of the polarization at the Kittel-mode frequency. This polarization oscillation is transformed into the amplitude oscillation by first rotating their polarization by 45 degrees by a half-wave plate and
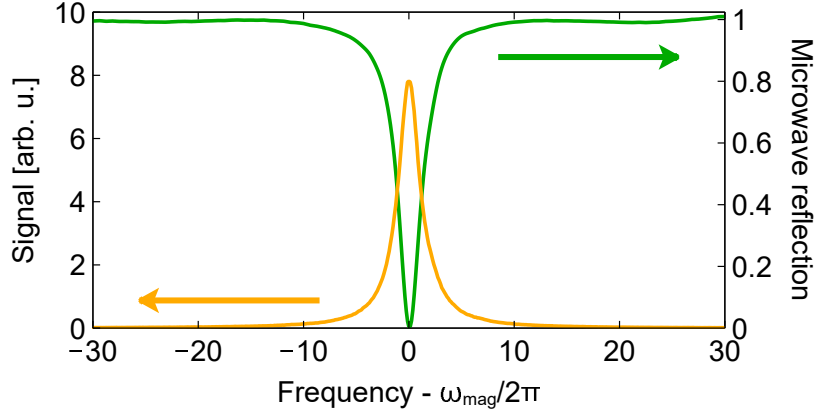
Figure 5.2: Observation of the Brillouin scattering of light in the WGM by the Kittel mode. Green and yellow curves show the normalized microwave reflection from the loop coil and the signal from the photodetector, respectively. The Kittel-mode frequency is $\omega_{\mathrm{mag}}/2\pi = 6.8$ GHz.

let them pass through a polarization beam splitter (PBS), which projects the two orthogonal polarization components from the input and the scattered beams onto the same horizontal plane. The light from the PBS impinges the high-speed photodetector and the amplitude modulation of the light at the Kittel-mode frequency is converted to the electric signal. This signal is amplified and then sent back to the other port of the network analyzer. With this configuration, as a signal of the Brillouin scattering we expect a peak at the Kittel-mode frequency with the same lineshape as the Kittel-mode.

The observed signals are shown in Fig. 5.2. The fraction of the reflected power of the microwave (FMR) is shown by the green curve and the dip corresponds to the resonance of the Kittel mode. The frequency of the Kittel mode is 6.8 GHz, in consistent with the measured magnetic field strength of 0.24 T. The signal of the optical sideband caused by the Brillouin scattering is plotted by the yellow one, which exhibits the peak at the same position as FMR with the same Lorentzian line shape. Thus, we succeeded in the observation of the Brillouin scattering of light in the WGM by the Kittel mode. In the following sections we investigate the properties of the Brillouin scattering by the Kittel mode, in order to deepen the understandings.
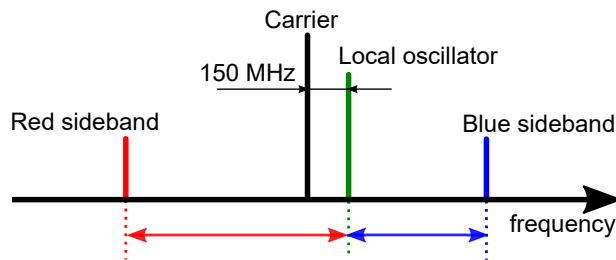
63

Figure 5.3: Schematic representation of the frequencies in the heterodyne measurement.
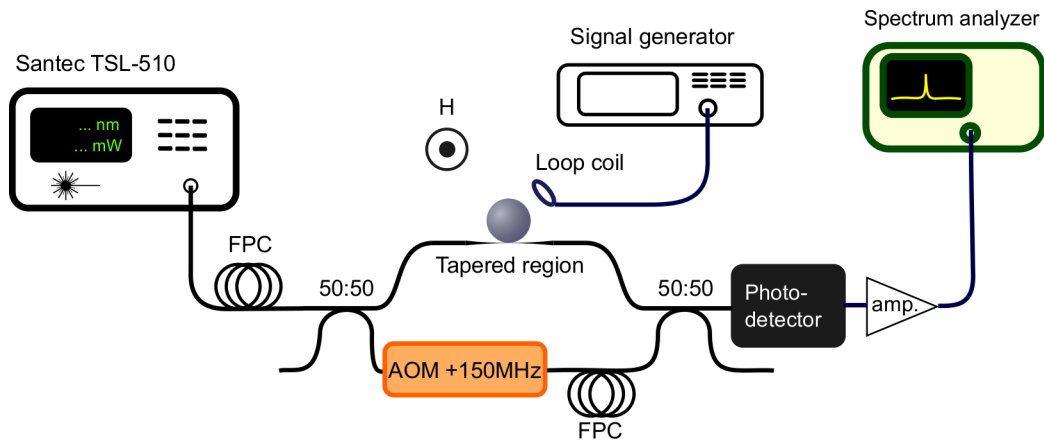

Figure 5.4: Experimental setup for the observation of the Stokes/anti-Stokes scattering asymmetry in the Brillouin scattering by the Kittel mode. The "local oscillator" light is generated by an acousto-optic modulator (AOM). The Kittel mode magnons are resonantly excited by microwaves form a signal generator and the signal of the Brillouin scattering is analyzed by a spectrum analyzer.
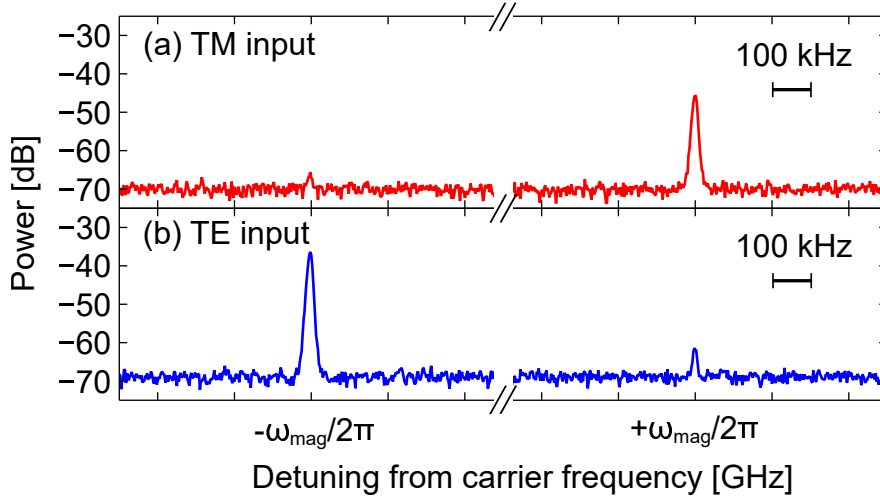
Figure 5.5: Observation of the Stokes/anti-Stokes scattering asymmetry for the cases of the two input polarizations TM (red) and TE (blue). The resolution bandwidth of the measurement is 10 kHz.

5.2 Observation of the sideband asymmetry

One of the most important picture of the Brillouin scattering process is the model of the optical transitions shown in Figs. 4.3 and 4.4. The relevant energy levels and the optical transitions imply that the spin angular momentum is conserved in the scattering processes, and should be examined. To examine this, we measure the up-converted blue sideband and the down converted red sideband separately. These are not separated in the signal in Fig. 5.2, since both of the red and the blue sidebands, with the lower and higher frequencies than the incident light by the Kittel-mode frequency, are made interfere with the incident light. To separate these two, we have to prepare a "local oscillator (LO)" laser light whose frequency is different from the one of the incident light. Then the frequency differences between the red sideband and the LO light and the blue sideband and the LO light are not equal. Therefore, the red and the blue sidebands can be separately measured in the frequency domain by letting the scattered light and the LO light interfere leading to the amplitude modulation with two different frequencies. The frequency differences resulting from such a heterodyne measurement is schematically drawn in Fig. 5.3.

The experimental implementation is shown in Fig. 5.4. The frequencies of the laser

light and microwaves from a signal generator are set to be on the resonances of the WGM and the Kittel mode, respectively. Laser light is divided by a fifty-fifty beam splitter and one of them passes through an acousto-optic modulator (AOM) with its frequency being shifted by +150 MHz to act as an LO. The polarization of the LO light is tuned so that it coincides that of the scattered light, which is perpendicular to the polarization of the input light to the WGM. The beat signal of the interference between the LO light and the scattered light is detected, amplified and sent to a spectrum analyzer. By observing the peaks at the frequencies higher and lower than the Kittel-mode frequency on the spectrum analyzer, we can extract the intensities of the signals of the red and the blue sidebands.

Experimentally observed red and blue sidebands are shown in Fig. 5.5(a) and (b), which are the results obtained for the cases of the TM (red spectra) and the TE (blue ones) WGM inputs for each. The resolution bandwidth of the measurement is 10 kHz. It can be seen that the intensities of the red and the blue sidebands, corresponding respectively to the Stokes and the anti-Stokes processes, are different by 20 dB. Another thing is that when the polarization of the incident light is changed from TM to TE, the ratio of the sideband is reversed. These features can be understood in terms of the optical transitions introduced in Figs. 4.3 and 4.4 as follows. First, focusing on the case of the TM WGM input, we experimentally had the blue sideband being superior to the red one. This situation can be possible, given the fact that the light is coupled to the CW WGM, with outer polarization case (Fig. 4.4). The inversion of the ratio of the sideband signals with the interchange of the polarizations result from the reversal of the scattering process. The interpretation of the obtained results are successfully done by such an explanation, however, one thing is missing in this context, that is, the missing contribution from the inner polarization. The explanation for this will be given in the Sec. 5.4 by taking the influence of the orbital angular momentum conservation into account.

5.3 Dependence on the laser frequency

In the previous experiments, we fixed the laser frequency on the WGM resonance. Here we sweep the frequency of the laser over the WGM spectra and see the behavior of the signal strength of the Brillouin scattering. Naive consideration leads to the
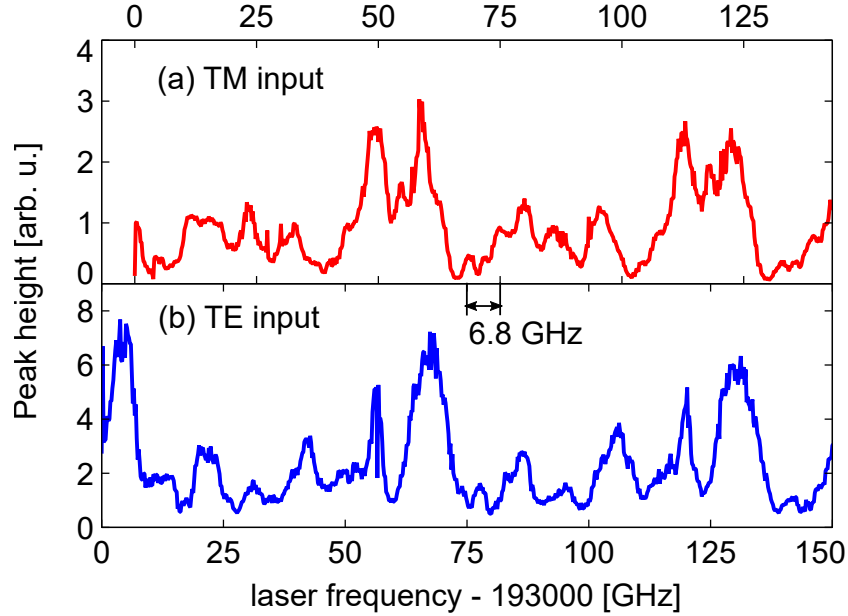
Figure 5.6: Peak height of the signal of the Brillouin scatteing vs. laser frequency for (a) TM-mode (with upper horizontal axis) and (b) TE-mode (with lower one) inputs.

notion that the scattering strength becomes simply proportional to the WGM spectra, and thus to the amount of light circulating in the WGM. However, this is not the case. It is revealed that the dependence of the scignal strength on the frequency of the input laser is closely related to the optical transitions involved in the Brillouin scattering processes.

Experimental setup is the same as in Fig. 5.1, except for that the laser frequency is not fixed here. By recording the signal heights of the optical sideband generated by the Brillouin scattering at various frequencies of the input laser, we acquire spectra of the signal height as in Fig. 5.6. The red and the blue curves represents the spectra for the TM and the TE WGM input, respectively. Note that the horizontal axes of these two spectra do not coincide, but rather that of the TM input case is shifted by 6.8 GHz, namely the Kittel-mode frequency. The correlation between the two spectra can be seen, and the correlation is deduced to be the spectral shift by the Kittel-mode frequency, but not the simple proportionality to the WGM spectra.

In Chapter 4, we have analyzed the Brillouin scattering strength in terms of the densities of states as Eqs. (4.20) and (4.21). These expressions are obtained for the
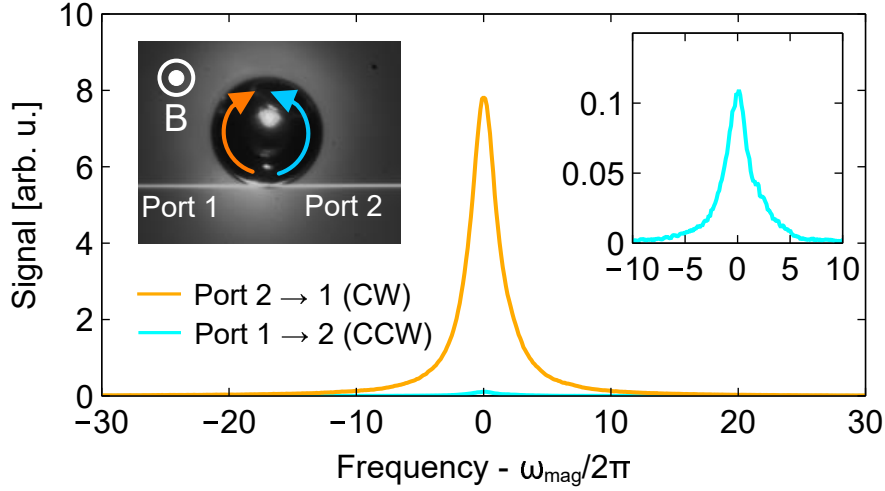
Figure 5.7: Nonreciprocal Brillouin scattering. The orange (light-blue) plot is the observed spectrum of the sideband signal for the input laser being TM-mode from Port 2 (1). The right inset shows an expanded plot of the light-blue curve. The left inset depicts the input ports and the direction of the static magnetic field.

inner polarization of WGMs, however, those for the outer polarization can be found immediately. In short, the scattering strength for the TE-mode input is proportional to $\rho_{\text{TE}}(\omega)\rho_{\text{TM}}(\omega - \omega_{\text{m}})$ and that for the TM-mode input to $\rho_{\text{TE}}(\omega + \omega_{\text{m}})\rho_{\text{TM}}(\omega)$, where ω is the frequency of the input laser. From these two factors, we observe that shifting the frequency of the one by the Kittel-mode frequency results in the other. This observation agrees well with the experimental results and is supportive of the theory developed in the last Chapter. Though the obtained spectra in Fig. 5.6 are too noisy to tell the frequency shift exactly, we will see clear feature in agreement with the theory in the next Chapter where the smaller number of the relevant WGMs can be achieved by the use of the prism coupling method.

5.4 Observation of the nonreciprocal Brillouin scattering

Magnetic field in general breaks the time-reversal symmetry, leading to the nonreciprocal phenomena. In the system under consideration, the nonreciprocity corresponds to the different behavior associated with the reversal of the WGM orbit, from CW to CCW and *vice versa*. The switching of the CW and the CCW WGMs can be done
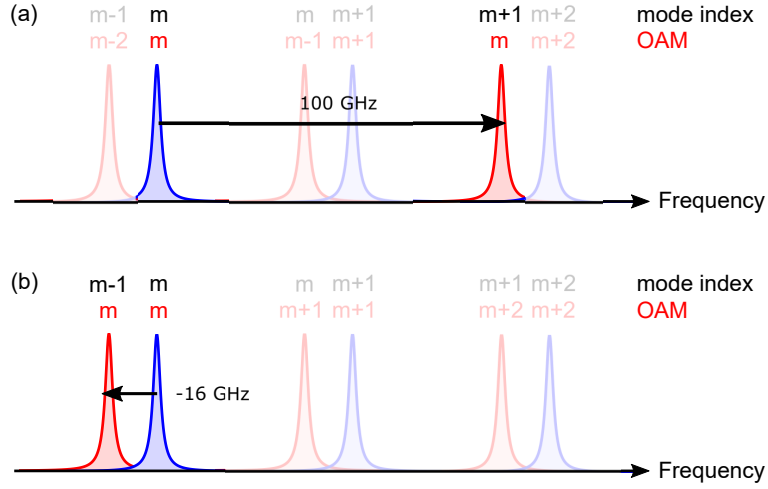
Figure 5.8: Relevant WGMs involved in the Brillouin scattering when (a) the inner and (b) the outer polarization components are considered. Here the input light is supposed to be coupled to the TE mode (blue) with the mode index m and the TM mode (red) that supports the scattered light is indicated for each case.

only by changing the connection of the optical fibers. The signals of the Brillouin scattering observed for the cases of the CW and the CCW WGMs are given in Fig. 5.7. The microscope image in the inset indicates the direction of the magnetic field and the input ports label by "1" and "2". With this setup we get the CW (CCW) WGMs coupled by injecting light from Port 2 to 1 (Port 1 to 2). From the figure we see that the signal of the Brillouin scattering of light in the CW WGM is more intense than that in the CCW WGM by two orders of magnitude. The plot in the right inset shows the magnified signal in the case of the CCW WGM alone.

The mechanism that gives this result is twofold. First, the spin angular momentum conservation is an important factor. The relevant scattering process and thus the energy of the scattered light is determined by this condition, as already supported by the sideband asymmetry and the spectral shift observed in the Secs. 5.2 and 5.3. The second is the orbital angular momentum conservation, which states a relevant WGM to which the scattered light belongs. The following discussion is mostly devoted to the description of the orbital angular momentum conservation.

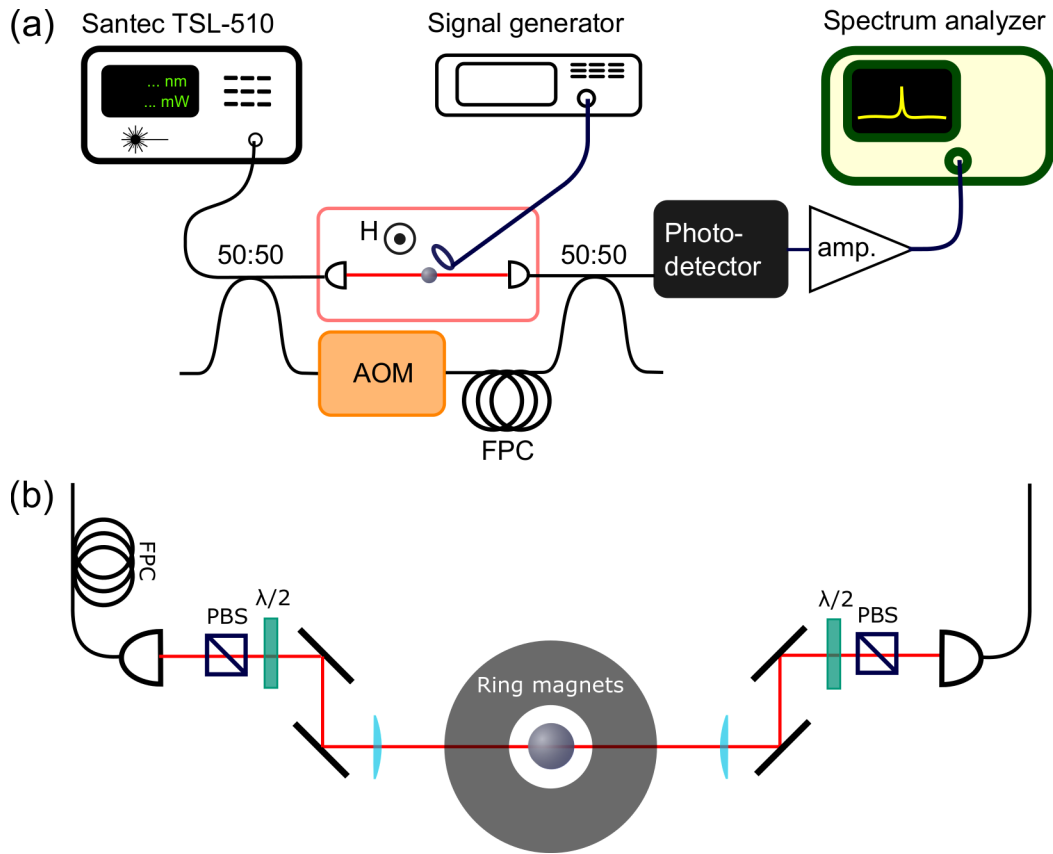As analyzed in the Chapter 2, the orbital angular momentum of a WGM with

Figure 5.9: Experimental setup of the heterodyne measurement of the Brillouin scattering with a propagating optical beam, where (a) shows the whole setup and (b) presents the detail of the part surrounded by a red box in (a). First the input 1550 nm-laser light is divided into two by a 50:50 beam splitter and one of the two is modulated by an acousto-optic modulator (AOM) to act as a local oscillator (LO). Another light beam is scattered by the Brillouin scattering and then mixed with the LO light to interfere. The Kittel mode is continuously excited by resonant microwaves sent to the loop coil from a signal generator and the signals of the optical sidebands are detected by a high-speed photodetector and a spectrum analyzer.

the mode index m should be carefully treated. We shall deal with the case of the TE-mode input, where the mode index and the orbital angular momentum coincide. In contrast, the orbital angular momentum of the TM mode depends on which region of the WGM we take into account, namely the inner or the outer region. Given that the mode index of the TM mode is m, we already saw that the inner component possesses the orbital angular momentum of $m-1$ and the outer one does that of $m+1$. The condition that the total orbital angular momentum of the system is conserved reads, in the current case with the Kittel mode, the invariance of the orbital angular momentum of the WGMs by the Brillouin scattering. Therefore, if the light in the TE mode of the index m is scattered by the Kittel mode, the light can be scattered into the inner (outer) polarization of the TM mode of the mode index $m+1$ $(m-1)$. Again note the difference between the orbital angular momenta and the mode indices of the TM WGMs.

The frequency difference between the TE(m) and TM$(m+1)$ modes, where the numbers in the parentheses denote the mode indices, is around 100 GHz, whereas the one between the TE(m) and TM$(m-1)$ modes is -16 GHz. The schematic picture of the WGM resonances are depicted in the Fig. 5.8(a) and (b), corresponding to the inner and the outer polarizations, respectively. This leads to the situation that the frequency of the scattered light, shifted by the Kittel-mode frequency, involving the outer polarization component is much closer to the relevant WGM. In contrast, the one involving the inner polarization component is far from the relevant WGM and the scattering is significantly suppressed. This is the reason for disregarding the inner polarization component as has been done in the last two Sections. When we limit the consideration on the outer polarization component, the spin angular momentum conservation tells us that the Brillouin scattering of light in the CW results in the red sideband as indeed shown in Fig. 5.5(b). As for the nonreciprocity from the Fig. 5.8(b), we see that the scattering in the CW WGM case is closer than the CCW WGM case, so that we have the stronger Brillouin scattering in the CW case, which explains the observed nonreciprocity of the Brillouin scattering in Fig. 5.7. However, this effect alone give the ratio of the signals in the CW (detuned by $16-7$ GHz) and the CCW cases (detuned by $16+7$ GHz) of only $(16+7)^2/(16-7)^2 = 6.5$. Here the estimation uses the fact the scattering strength is proportional to the inverse
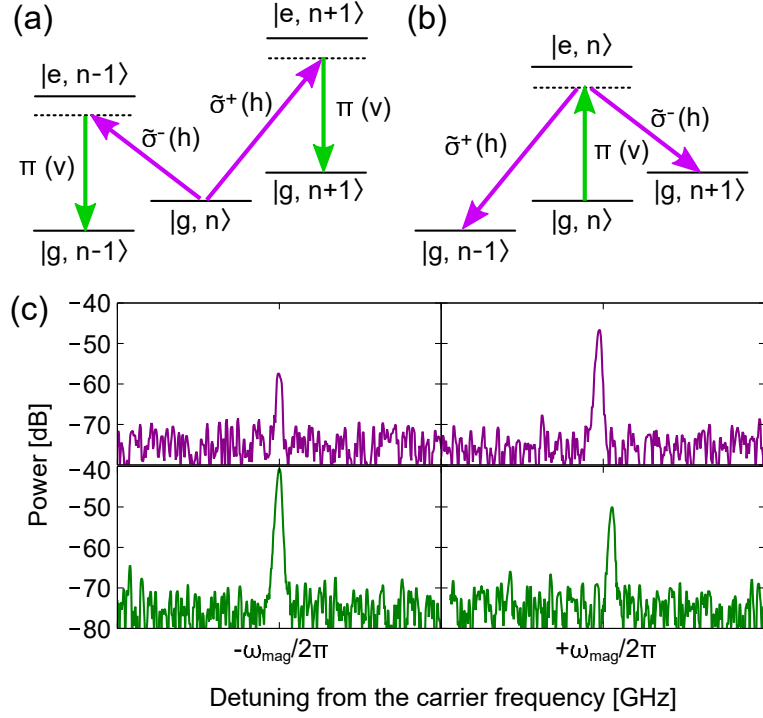
Figure 5.10: (a), (b) The relevant energy levels and optical transitions for (a) the vertical and (b) the horizontal polarization inputs. (c) Generated sideband for the horizontal (upper panels) and the vertical (lower panels) polarization inputs. The span of each plots and the resolution bandwidth are 100 kHz and 1 kHz, respectively.

square of the detuning, see Eq. (4.20) or (4.21). Further consideration is required to qualitatively explain the observed ratio of around 100 and will be discussed in the next Section.

5.5 Measurement of transition strengths for different circular polarizations

The spin and the orbital angular momentum conservation are the main factors that contributes to the nonreciprocal nature of the Brillouin scattering in this system, however, we introduce another one here, that is, the difference between transition strengths with $\tilde{\sigma}^+$- and $\tilde{\sigma}^-$-polarized light. Being aware of the fact that such a difference is the very origin of the magneto-optical effect, it seems natural to admit it. We

present a way to measure the difference of the transition strengths for the two circular polarizations by utilizing the Brillouin scattering of not the WGMs, but the propagating optical beam [8]. The experimental configuration is depicted in Fig. 5.9. The propagating optical beam impinges the sample in the direction perpendicular to the applied static magnetic field and the polarization modulation caused by the Brillouin scattering is translated into the amplitude modulation through the interference with the LO light through the acousto-optic modulator (AOM). Thus the signal is again obtained by the heterodyne measurement in order to separately evaluate the red and the blue optical sidebands.

The horizontal (h) polarization input, the linear polarization in the plane of the paper, is the polarization perpendicular to the static magnetic field and therefore the mixture of $\tilde{\sigma}^+$ and $\tilde{\sigma}^-$ polarizations with equal amounts. The generated red and blue sidebands correspond respectively to the transitions including $\tilde{\sigma}^+$ and $\tilde{\sigma}^-$ polarizations. If the input polarization is the vertical (v) polarization, the one parallel to the magnetic field and thus being π-polarized, the correspondence becomes reversed. These are depicted in Fig. 5.10(a) and (b). Therefore, by measuring the ratio of red and blue sidebands we can estimate the ratio of the strength of the transitions caused by the corresponding polarizations. The experimental results are shown in Fig. 5.10(c). The results of h-polarization input (upper panels) show the sideband asymmetry by 10 dB. From the corresponding optical transition, we can say that the transition strength of $\tilde{\sigma}^-$-polarized light is 10 dB larger than that of the $\tilde{\sigma}^+$-polarized one. The results of the v-polarization input (lower panels), the ratio of the blue and red sidebands are reversed, as expected. Thus, it is experimentally confirmed that the strength of the $\tilde{\sigma}^-$-polarized light is stronger than that of the $\tilde{\sigma}^+$-polarized one by 10 dB.

At this point, we go back to the conservation of the nonreciprocal nature of the Brillouin scattering. The outer polarization of the CW and the CCW WGMs correspond respectively to $\tilde{\sigma}^-$ and $\tilde{\sigma}^+$ polarizations. Therefore the ratio of the signals for the CW case to the CCW case now reads $(16 + 7)^2/(16 - 7)^2 \times 10 = 65$, where the first factor is the same as before and the second factor of 10 comes from the difference between the transition strengths. This agrees with the observed experimental result in Fig. 5.7.
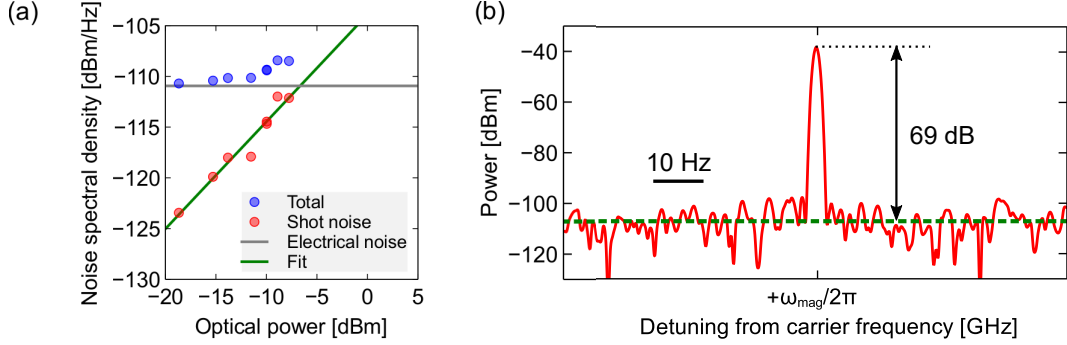
Figure 5.11: Estimation of the conversion efficiency by the measurement of the strength of the sideband signal and its ratio to the shot-noise power level. (a) Calibration of the shot noise level. Blue dots are the total noise floor and the gray horizontal line represents the electronic noise. Red ones are the calibrated shot-noise level and the green line is the linear fit for them. (b) Sideband power for the TM polarization measured by the spectrum analyzer with the resolution bandwidth of 1 Hz.

5.6 Conversion efficiency

So far we discussed about the Brillouin scattering in a qualitative manner, such as the relative strengths of the scattering processes. To close this chapter, we evaluate the absolute strength of the Brillouin scattering, which is given here as a microwave-to-optical photon conversion efficiency.

Regarding the optomagnonic system as a microwave-to-optical-photon converter, the estimation and the prospects for further improvement of the conversion efficiency are of crucial importance. To evaluate the conversion efficiency $n_{\mathrm{TE}}^{(\mathrm{out})}/n_{\mathrm{MW}}^{(\mathrm{in})}$, we focus on the peak height of the sideband obtained in the experimental setup shown in Fig. 5.4. A spectrum of the blue sideband for the TM-mode input is shown in Fig. 5.11(b) which is taken by the spectrum analyzer with the resolution bandwidth of 1 Hz. Since the experiment is done with the heterodyne measurement, the squared value of the beat note $\eta n_{\mathrm{LO}} n_s$ is observed at the spectrum analyzer where η represents the coefficient accompanied to the conversion from optical power to the voltage at the photodetector, n_{LO} the photon flux of the LO light and n_s that of the sideband signal. The noise floor observed by the spectrum analyzer is the squared value of the photon shot-noise power accompanied to the LO light, namely, $\eta(\sqrt{2n_{\mathrm{LO}}})^2 = 2\eta n_{\mathrm{LO}}$.

Therefore the signal-to-noise ratio is given in a simple form as $n_s/2$. The shot-noise level at the spectrum analyzer is calibrated separately by measuring the noise spectral density at various optical power, and the extracted photon shot noise level is shown in Fig. 5.11(a). As in Fig. 5.11(b), the signal-to-noise ratio is 69 dB, which directly tells us the generated sideband photon number of 8.1×10^6. Finally, as we know that the photon flux of the input microwaves is 2.2×10^{20} /s for 0 dBm input and microwaves are critically coupled to the Kittel mode, the conversion efficiency can be evaluated as 7×10^{-14} for the current experimental conditions.

It is then possible to evaluate the value of the optomagnonical coupling coefficient $g^{(\text{exp})}$ using Eq. (4.20). With the photon flux of the input optical field $n_{\text{TM}}^{(\text{in})} = 3 \times 10^{15}$ /s at 0.3 mW, the frequency difference between the TE and the TM WGMs 9 GHz, and typical intrinsic quality factors of WGMs 1×10^5, the coupling coefficient $g^{(\text{exp})}$ is calculated to be $2\pi \times 0.4$ Hz. Here we use the detuning $\Delta_{\text{TM}}/2\pi$ of the input laser being 3 GHz lower than $\Omega_{\text{TM}}/2\pi$, which maximizes the sideband strength in the experiment we performed. External couplings κ_{TE} and κ_{TM} are set to be 0.4 GHz for each WGMs regarding the transmission, and critical coupling for the Kittel mode, namely $\Gamma_{\text{m}} = \kappa_{\text{m}}$. The experimentally obtained value of $g^{(\text{exp})}$ is an order of magnitude smaller than the expected value $g^{(\text{theory})} = 2\pi \times 5.4$ Hz. The possible reason is the suppression of the interaction for the outer polarization components due to the effect of the resonator surface, which will be discussed again in the next Chapter. The imprecise choice of the parameters in $g^{(\text{exp})}$, such as the cavity decay rates Γ_{TE} and Γ_{TM}, may also affect.

In order to further improve the conversion efficiency, first we can change the size and shape of the WGM resonator so that the frequency difference between the TE and the TM WGMs, $\Omega_{\text{TM}} - \Omega_{\text{TE}}$ approaches the Kittel mode frequency Ω_{m}. In other words, it will be beneficial to make the frequency matching condition $\omega_{\text{TM}} - \omega_{\text{TE}} - \omega_{\text{m}} = 0$ for microwave and optical fields involved be supported by the WGMs and the Kittel mode, $\Omega_{\text{TM}} - \Omega_{\text{TE}} - \Omega_{\text{m}} = 0$. If this is done, the conversion efficiency will be 700 times larger. Second, by properly polishing and chemically processing the WGM resonator one can get a higher quality factor approaching the value limited by the optical absorption, $\sim 3 \times 10^6$ derived from the absorption coefficient $\alpha = 0.03$ /cm at room temperature [26]. This gives further improvement of the conversion efficiency by a factor of 3 500. Third,

the squared coupling coefficient g^2 is inversely proportional to the sample volume as can be seen in Eq. (4.13). Therefore, the non-spherical WGM resonator like disks and ellipsoids are of interest in this perspective. For instance, a 1 μm-thick and 2.5 mm-diameter disk, which is expected to have a frequency difference between the TE and the TM WGMs of around 10 GHz according to the finite element method [21, 22], reduces the volume by a factor of 90, and thus the conversion efficiency gains that factor. All these enhancements together with optical input power of 20 mW will give the improved conversion efficiency of 4.0×10^{-4}. With this value, the microwave-to-optical photon conversion enables various experiments, such as the optical control and readout of the quantum state of the superconducting quantum bit in the postselective way.

To reach unity photon conversion efficiency, additional ingredients should join the system. Aside from the ways described above, a possibility for improvement is the reduction of the decay rate of the Kittel mode which becomes as small as 500 kHz at 1 K [46]. Other transparent materials with a large Verdet constant may further improve the efficiency to achieve the unity efficiency.

Chapter 6

Observation of Brillouin scattering of light in WGM with a prism

The observations made in the previous Chapter mark intriguing properties of the Brillouin scattering of light in the WGMs by the uniform magnetostatic mode, the Kittel mode. Now, the basic properties of the Brillouin scattering of light in the WGMs being revealed, it will be of interest to investigate the Brillouin scattering caused by the general, nonuniform Walker modes. In this Chapter we adopt the prism coupling of the WGMs to avoid the ambiguity of the polarizations coupled to them.

6.1 Experimental setup

For the investigation of the Brillouin scattering, we have to reconsider the coupling method to the WGMs in the YIG sphere. This is because we indeed had a problem of the ambiguity in determining the polarization coupled to the WGM when using the tapered optical nanofiber. To avoid this ambiguity, we adopt the use of a prism coupling method, with which we can unambiguously tell which polarization of the WGMs is coupled. Experimental setup is depicted in Fig. 6.1. The 1.5 μm laser light passes through a fiber polarization controller (FPC) and the linear polarization is defined
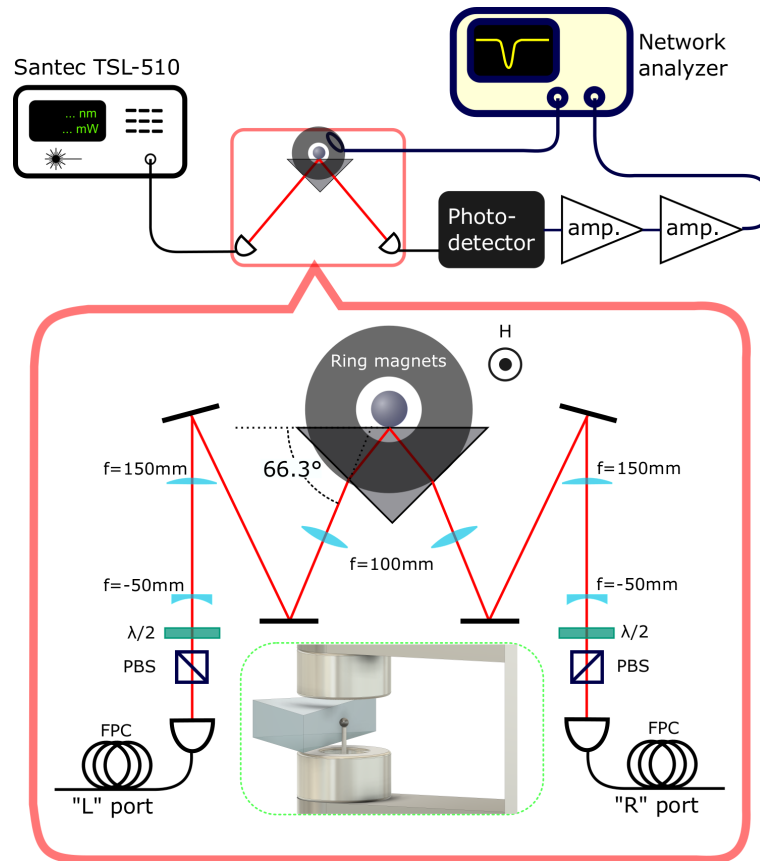
Figure 6.1: Experimental setup for the observation of the Brillouin scattering by the Kittel mode. WGMs are coupled via a prism, as shown in the red box indicating the detailed optical configuration around the YIG sphere. The inset in the green dotted box shows the schematic picture of the configuration of the prism, the YIG sphere and the magnets. The scattered and the unscattered light are made interfere with a half-wave plate ("$\lambda/2$") and a polarization beam splitter (PBS). The direction of the circulation of the WGMs is determined by which port ("L" or "R") is used as the laser input. A network analyzer send microwaves to a loop coil and collect the signal from the high-speed photodetector.
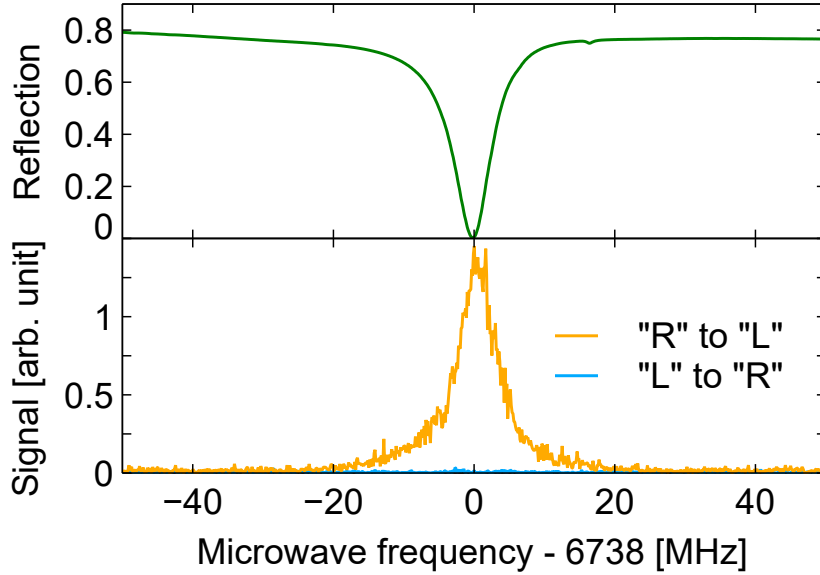
Figure 6.2: Observation of the nonreciprocity of the Brillouin scattering of WGM light by the Kittel mode. The upper and the lower panels show the microwave reflection and the signals of the Brillouin scattering, respectively. "R" to "L" ("L" to "R") indicate the case that the light comes from "R" ("L") port to "L" ("R") port. In this case the prism coupling method is used.

by a polarization beam splitter (PBS) and a half-wave plate ("$\lambda/2$"). As mentioned earlier in Chapter 2, a single-crystalline silicon prism is used as the coupling method to the WGMs in a 1 mm-diameter YIG sphere[1] and the angle of incidence to the prism should be tuned as discussed there. As has been done before, microwaves from a network analyzer excite the Walker modes. The unscattered and the scattered light after the prism interfere with each other to form the modulation of the polarization, which is transformed into the amplitude modulation through a half-wave plate and a PBS. From the construction, the freely propagating part of the optical setup is made symmetric, so that we can simply exchange the optical fibers of the input and output ports, "R" and "L" in the figure, to get access to both the CW and the CCW WGMs.

---

[1]With the diameter of 1mm, the condition $\Omega_{\mathrm{TM}} - \Omega_{\mathrm{TE}} = \Omega_{\mathrm{m}}$ can be realized with some effort. Details will be given in Sec. 6.3.2.
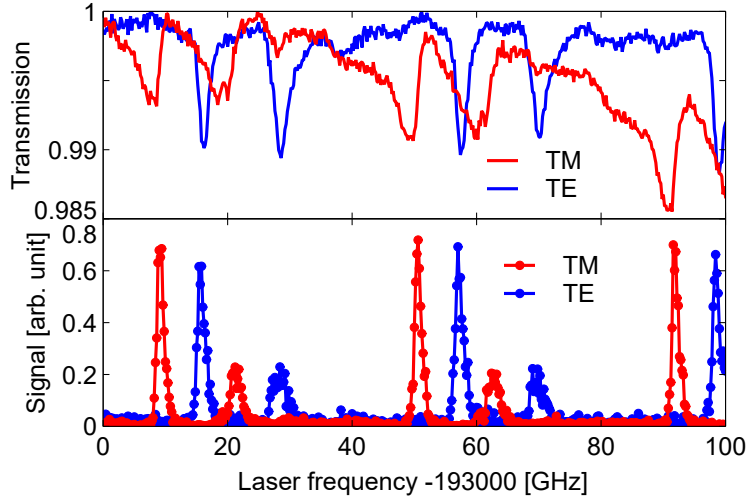
Figure 6.3: Dependence of the Brillouin scattering by the Kittel mode on the frequency of the input laser. The WGM spectra are presented in the upper panel and the signal strengths of the Brillouin scattering are plotted in the lower panel.

6.2 Brillouin scattering by the Kittel mode (revisited)

In this section, we check the nonreciprocity and the dependence on the frequency of the input laser with the prism coupling. This ensures that the nonreciprocal effect is due to the combination of the spin and the orbital angular momentum conservation and eliminates the possibility that it comes from other factors caused by the nanofiber coupling in the previous Chapter. Since we have a less number of observable WGMs using the prism, we expect that the clearer feature of the spectral shift for the two input polarizations can be observed.

As described above, the nonreciprocity of the Brillouin scattering by the Kittel mode is examined by exchanging the optical fibers connected to the "R" and "L" ports. The results are shown in Fig. 6.2, where "R" to "L" ("L" to "R") direction addresses the CW (CCW) WGM. Here we again have the signal of the Brillouin scattering in the case of the CW WGM, while we have substantially small signal in the case of the CCW WGM. Therefore we can confirm that the nonreciprocity of the Brillouin scattering is independent of the coupling method. The degraded signal-to-noise ratio in Fig. 6.2 compared to that using the nanofiber is due to the tens of times
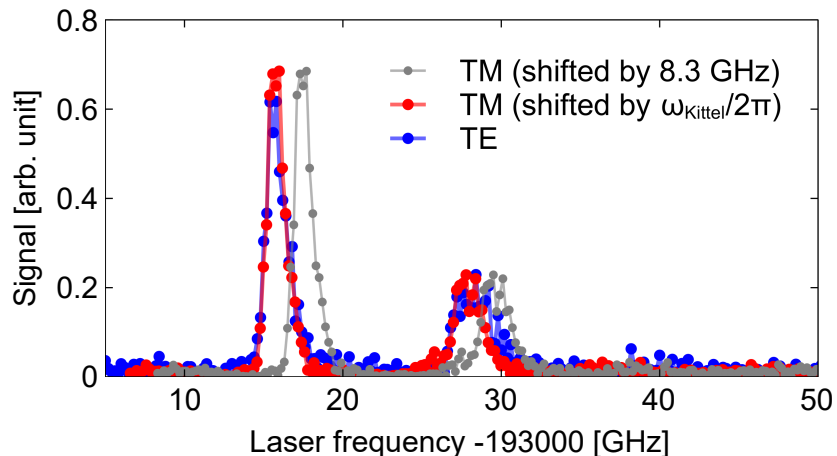
Figure 6.4: Dependence of the Brillouin scattering by the Kittel mode on the frequency of the input laser. The spectra for the TM-mode input shifted respectively by the Kittel-mode frequency $\omega_m/2\pi$ (red) and the frequency difference between the closest pair of the TE and the TM WGMs (8.3 GHz, gray), with the one for the TE-mode input are shown.

smaller coupling to the WGM with the prism.

Next we sweep the frequency of the input laser and record the signal intensities. Figure 6.3 presents the outcomes. The upper panel shows the WGM spectra for the two polarizations TM (red) and TE (blue). The lower panel shows the height of the Brillouin scattering signals for the two polarizations. We observe two major WGMs within a FSR and corresponding peaks in the signal of the Brillouin scattering. We again note that the maxima of the peaks in the lower panel do not coincide with the position of the resonances of the WGMs. The spectra of the signal for the TM mode input is shifted by the Kittel-mode frequency and plotted with that of the TE mode in Fig. 6.4. The excellent coincidence between the spectrum for the TE-mode input (blue) and the shifted one for the TM-mode input (red) can be seen. The one for the TM-mode input with the shift by 8.3 GHz (gray), the frequency difference between the closest pair of the TE and the TM WGMs, clearly shows the deviation. Thus, the clearer signature of the spectral shift is obtained in this case,
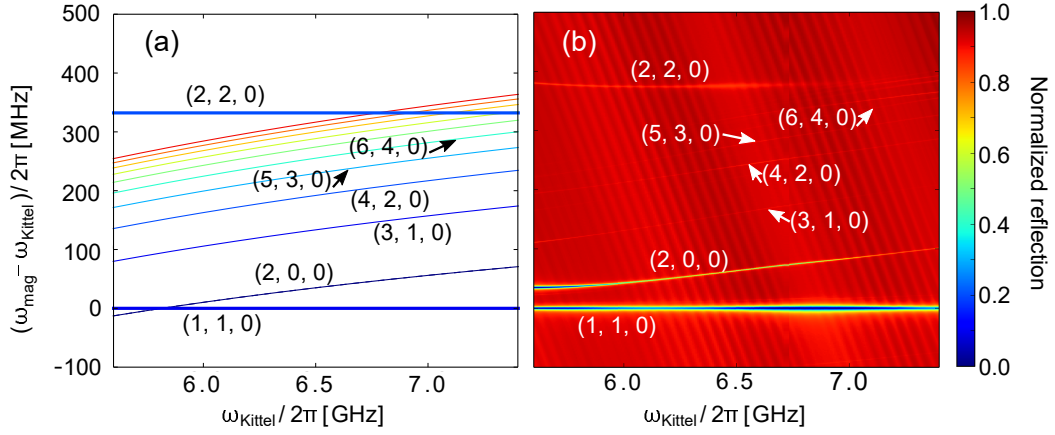
Figure 6.5: (a) Theoretical values of the Walker-mode frequencies relative to the Kittel or $(1, 1, 0)$ mode. Only the mode families of $(m, m, 0)$ (bold solid) and $(m + 2, m, 0)$ (thin solid) are plotted, where the color from blue to red are assigned in the order from small to large m. (b) Experimentally observed microwave reflection spectra with the variable magnetic field, i.e., the variable Kittel-mode frequency.

which proves the relevance of the consideration given in Sec. 5.3 and eliminates the simple proportionality to the WGM spectra.

6.3 Brillouin scattering by Walker modes

Now that the properties of the Brillouin scattering by the Kittel mode is successfully reproduced by the different coupling scheme to the WGMs, and we proceed to the next topic, that is, the Brillouin scattering caused by the nonuniform Walker modes. Before we proceed, the FMR spectra of the Walker modes should be checked in order to assign mode indices. Since the inhomogeneity of the magnetic field often results in slight of the frequencies of the Walker modes, we should identify them every time we change the configuration of the magnets. By now we apply the magnetic field around 0.26 T which gives the Kittel-mode frequency of 7.3 GHz, without applying electric current to an electromagnetic coil attached to the magnetic circuit. By applying the variable electric current to it, we can get the FMR spectra of the Walker modes as shown in Fig. 6.5. The observed modes are identified by the comparison with the
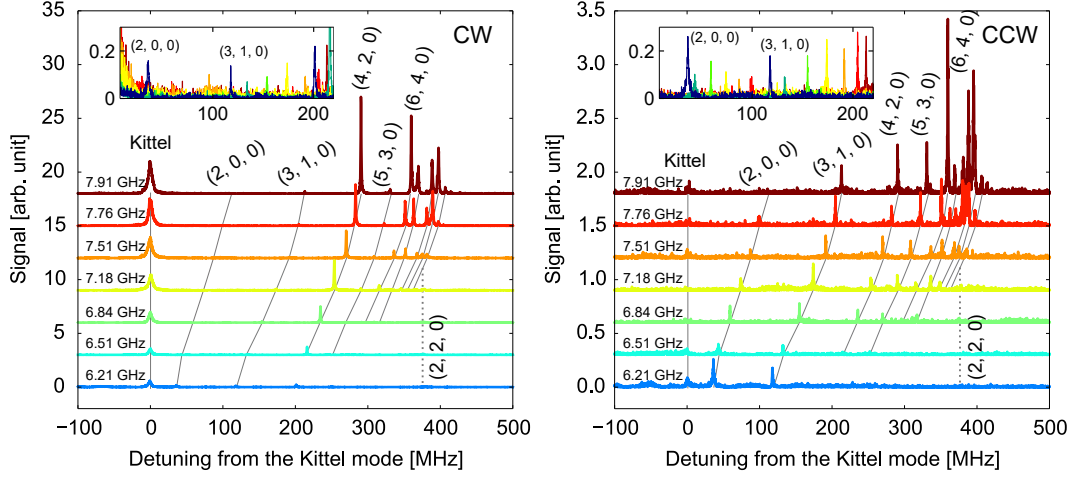
Figure 6.6: Brillouin scattering signals obtained for the cases of the CW (left) and the CCW (right) WGMs. The Kittel-mode frequencies are shown on the left of the plots. The assigned mode indices are also shown and indicated by the gray lines. Insets show the expanded plots including $(2, 0, 0)$ and $(3, 1, 0)$ modes without the vertical offsets. Note that the vertical scales are different between the two panels.

theory. It should be noted again that the $(2, 2, 0)$ mode and the higher-order ones of the $(m + 2, m, 0)$ family exhibit a number of normal mode splittings as well as the Kittel mode and the $(2, 2, 0)$ mode. The overall shift of the frequencies of the Walker modes are also reproduced. The difference from Fig. 3.9 is the configuration of the sphere, where in Fig. 6.5 the rod attached to the sphere is placed as indicated in the inset of Fig. 6.1. In Fig. 3.9 the configuration is the same as shown in Fig. 3.3.

These identifications of the Walker modes allow us to investigate the behavior of the Brillouin scattering caused by the Walker modes. The signals of the Brillouin scattering obtained for the various values of the magnetic field are plotted in Fig. 6.6. The frequency presented on the left of each plot stands for the Kittel-mode frequency. In varying the magnetic field and thus the Kittel-mode frequency, we always set the Kittel-mode frequency as a reference and consider the detuning from it as a horizontal axis. Note that the plots are shifted in the vertical axis. Gray lines indicate the positions of the modes with the mode indices assigned. The position of the $(2, 2, 0)$ mode, whose scattering signal is almost invisible, is also shown by a gray dashed line.

The left (right) panel of the Fig. 6.6 shows the obtained signals for the CW (CCW)
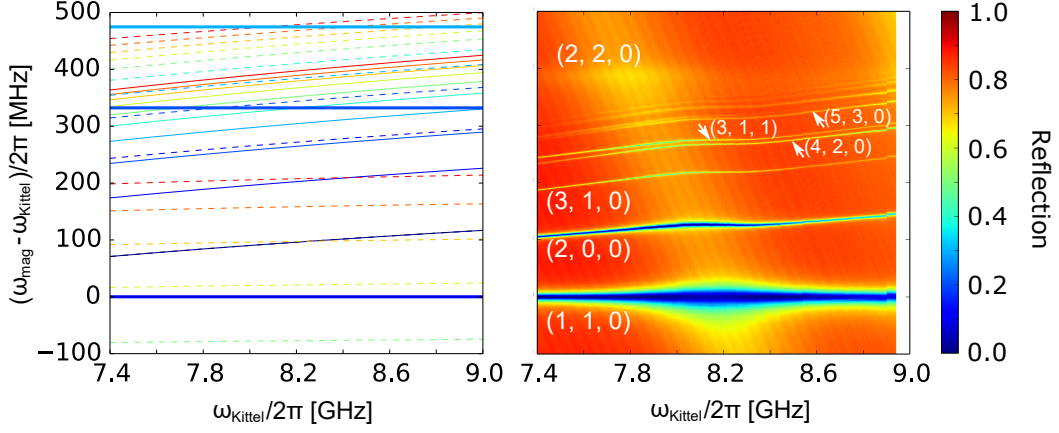
83

Figure 6.7: (a) Theoretical values of the Walker-mode frequencies relative to the Kittel or $(1, 1, 0)$ mode. Only the mode families of $(m, m, 0)$ (bold solid) and $(m + 2, m, 0)$ (thin solid) are plotted, where the color from blue to red are assigned in the order from small to large m. (b) Experimentally observed microwave reflection spectra with the variable magnetic field, i.e., the variable Kittel-mode frequency.

WGM. Be aware that the vertical scales are different between these two panels. There we observed again the pronounced nonreciprocity of the signal by the Kittel mode. Note that those such as the Kittel and the $(4, 2, 0)$ modes give the larger scattering signals in the CW case, while for the $(2, 0, 0)$ mode, the CCW case exhibits the larger signal.

We can see the growth of the signal by the Kittel mode in the CW case as the Kittel-mode frequency gets large. This behavior is later analyzed in terms of the resonant enhancement of the scattering by the WGM. Another noticeable point is that for the Kittel-mode frequency around 5.8 GHz, where the Kittel mode and the $(2, 0, 0)$ mode exhibit a normal-mode splitting, the signal of the Brillouin scattering by the $(2, 0, 0)$ mode becomes visible in the spectrum in the CW case. It can be also seen that for the Kittel-mode frequency higher than 7.1 GHz, the signals caused by the $(6, 4, 0)$ and even higher-order modes rapidly grows up.

We tried another pair of permanent magnets for applying the static magnetic field, which gives the magnetic field of around 0.3 T (8.6 GHz in terms of the Kittel-mode frequency). The spectrum of the Walker mode and the signals of the Brillouin
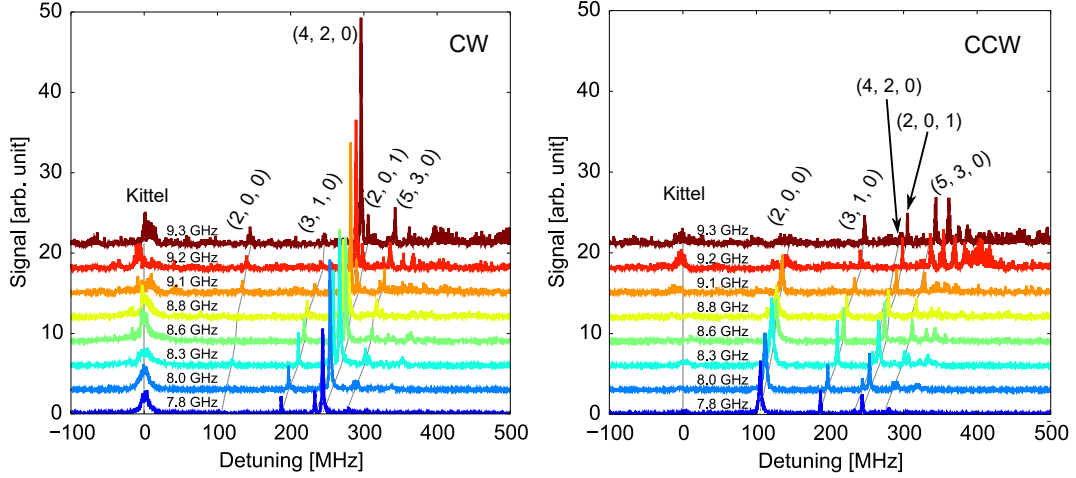
Figure 6.8: Brillouin scattering signals obtained for the cases of the CW (left) and the CCW (right) WGMs. The Kittel-mode frequencies are shown on the plots. The assigned mode indices are also shown and indicated by the gray lines.

scattering are given in Figs. 6.7 and 6.8, in the same manners as Figs. 6.5 and 6.6. In this case the signal of the Brillouin scattering by the Kittel mode shows the Fano-like interference with the signal by the higher-order Walker modes intersecting the Kittel mode. This behavior will also be discussed later together. Again, the signals by those such as the Kittel mode and the $(4, 2, 0)$ mode are larger in the case of the CW WGM, whereas the ones by the $(2, 0, 0)$ mode are superior for the CCW WGM case.

In short, our observation tells us that the behavior of the Brillouin scattering is strongly affected by the involved Walker modes and how the individual Walker mode couples to each other. Below we focus on the following two points: the reason of the larger Brillouin scattering strength by the $(2, 0, 0)$ mode for CCW WGM and the dependence of the scattering strength by the Kittel mode on the magnetic field.

6.3.1 Brillouin scattering by the $(2, 0, 0)$ mode

Here we intend to understand the reason why the Brillouin scattering by the $(2, 0, 0)$ mode has larger signal in the case of the CCW WGM than in the case of the CW WGM, in contrast to the Kittel mode. With the orbital angular momentum of $m = -1$ for the $(2, 0, 0)$ mode, we see that the orbital angular momentum conservation (4.5) and (4.9) leads to $m_{\mathrm{TM}} = m_{\mathrm{TE}}$ in terms of the WGM indices. This condition does
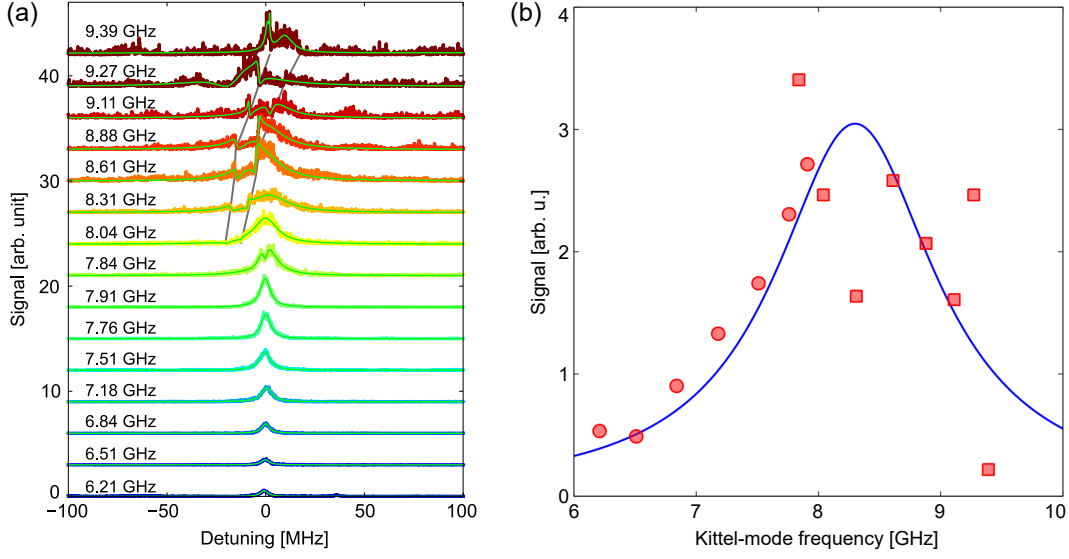
Figure 6.9: Dependence of the scattering signal by the Kittel mode on the magnetic field. In (a), the fitting results are shown by the green lines (see the main text). The observable higher-order modes are fitted and their positions are indicated by the gray lines. (b) The results of the fittings for the scattering strengths (peak values) by the Kittel mode. The blue curve is the fitting for data. See the main text for the detail.

not depend on the inner or the outer polarization, so that the scattering strengths with the CW and the CCW WGMs do not make any difference in theory. In other words, the Brillouin scattering by the $(2, 0, 0)$ mode is expected to be lack of the nonreciprocity if we only consider the orbital angular momentum conservation.

One thing that should be incorporated is the difference of the transition strengths between $\tilde{\sigma}^+$- and $\tilde{\sigma}^-$-polarized light. From the preceding Chapter, we saw that the transition strength of the $\tilde{\sigma}^-$-polarized light is 10 dB larger than that of the $\tilde{\sigma}^+$- polarized one. For the case of the CW (CCW) WGM, the inner (outer) polarization is $\tilde{\sigma}^-$-polarized (see Table 4.3.3), so that we expect that the CW & inner (CCW & outer) case gives the dominant signal. However, this does not change the situation because the orbital angular momentum conservation reads the same for both of the CW & inner and the CCW & outer cases. In other words, there is nothing that makes difference between the Brillouin scattering of the CW and the CCW WGMs.

Another thing we may assume is the suppression of the Brillouin scattering involving the outer polarization, that is, the scattering accompanied to the outer po-

larization is suppressed by two orders of magnitude. This can be deduced from the fact that the experimentally obtained optomagnonical coupling coefficient is 10 times smaller than the theory, which is discussed in the Sec. 5.6. The suppression of the Brillouin scattering by the outer polarization may occur, since the polishing processes can drastically change the crystalline structure only in the very vicinity of the surface. Given this being the case, we have the Brillouin scattering by the inner polarization of the CCW WGM unaffected but that of the outer polarization of the CW WGM suppressed by a factor of around 100. For the Brillouin scattering by the $(2, 0, 0)$ mode, this makes the signal with the CCW WGM superior to the one with the CW WGM. Thus, if we admit the above assumption, the experimental observation of the inversion of the nonreciprocity with the $(2, 0, 0)$ mode can be explained.

6.3.2 Dependence on the magnetic field

The signals of the Brillouin scattering by the Kittel mode seen in Figs. 6.6 and 6.8 are combined and displayed in Fig. 6.9(a). We analyze the dependence of the Brillouin scattering strength on the magnetic field strength shown in the figure. The height of the signal by the Kittel mode is extracted at each Kittel-mode frequency by the curve fitting with Lorentzian function (green curves). Note that some higher-order Walker modes apparently give rise to the Fano-like interference above the Kittel-mode frequency of around 8 GHz, whose positions are indicated by the gray lines. Here the Fano-like interference is referred to as an interference of scattering processes which occurs when a narrow resonance couples to continuum or a broad resonance [54, 55]. Each of the observable two relatively narrow signals coming across the Kittel mode is fitted together with the Kittel mode by a function

$$A \frac{[\omega - \omega_0 + q(\Gamma/2)]^2}{(\omega - \omega_0)^2 + (\Gamma/2)^2}$$

with the magnitude A, the position ω_0, the full-width-half-maximum Γ and the coupling parameter q being the fitting parameters. The results are plotted in Fig. 6.9(b), where circular (square) dots indicate the data taken from Fig. 6.6 (Fig. 6.8). Lorentzian fit for these two kinds of data is shown by the blue curve in Fig. 6.9(b), where the only free parameter is its height. The position of 8.3 GHz is given by the difference of the frequencies between the TE and the TM WGMs, and the width of 1.6 GHz

is that of the WGM. From this, we see a certain agreement with the theoretical prediction that the Brillouin scattering is strongest when the Kittel-mode frequency and the frequency difference between the relevant input and output WGMs (8.3 GHz) coincide.

To close this Chapter, we shall calculate the resonantly enhanced microwave-to-optical photon conversion efficiency through the Brillouin scattering with the aid of the formulae (4.20). This is compared with the conversion efficiency obtained in Ref. [8], where the propagating optical beam is used. In terms of the WGM-assisted enhancement of the Brillouin scattering, the signal obtained in Fig. 5.11 was suppressed due to the mismatch of the condition $\Omega_{\mathrm{TE}} - \Omega_{\mathrm{TM}} = \Omega_{\mathrm{m}}$. If this condition is satisfied, that is, if the resonant enhancement is realized as done in Fig. 6.9, the conversion efficiency of 7×10^{-14} evaluated from Fig. 5.11 gains a factor of 700. On the other hand, the microwave-to-optical conversion efficiency evaluated with the propagating optical beam is around 10^{-10} with the input optical power of 15 mW [8]. If the optical power is increased from 0.3 μW to 15 mW in our system, another factor of 50 is multiplied to the conversion efficiency. Combining these two improvements together, the conversion efficiency is estimated to be 2×10^{-9}, which is roughly 20 times larger than that of Ref. [8]. In the comparison between the case of using WGMs and the propagating optical beam, we suppose that the enhancement by the optical cavity can be interpreted into the elongation of the sample length. The effective sample length using the WGM of the quality factor of around 10^5 is 20 times longer than that in Ref. [8]. Therefore the conversion efficiency using the WGMs is expected to be 20 times larger than that with the propagating optical beam, which is indeed the case as is shown above[2].

---

[2]There is still a discussion on this consistency, because the estimation given here does not take into account the suppression of the Brillouin scattering involving the outer component of the WGMs. If the experimentally obtained conversion efficiency of 2×10^{-9} is resulted in by such an suppression effect, the "true" conversion efficiency, which overcame the suppression, might be two-orders-of-magnitude larger.

Chapter 7

Conclusion and Outlook

We implemented a system of cavity optomagnonics by a sphere made of single-crystal YIG which is a ferrimagnetic material transparent for 1.5 μm-wavelength light. We first observed the WGMs in YIG spheres in Chapter 2. The FSR and the frequency difference between the TM and the TE modes with the same mode index can be considered to be consistent with the theoretical predictions. We tried two coupling methods using a prism and a tapered optical nanofiber, whose merits and demerits were mentioned in terms of the coupling to the WGMs and the determination of the polarizations. Next in Chapter 3, the Walker modes were examined and identified with some configurations of the applied static magnetic field with or without the inhomogeneity. We observed the significant couplings among the Walker modes, which result mainly from the inhomogeneity of the magnetic field. The spin and the orbital angular momenta of the WGMs and the Walker modes were theoretically analyzed in these Chapters.

We constructed the theory of the Brillouin scattering of the WGM light by the Walker modes in Chapter 4. Our theory involves the spin and the orbital angular momentum conservations, which play important roles in the Brillouin scattering. The interaction Hamiltonian and the resultant Heisenberg equations of motion were analyzed in the framework of the input-output theory.

In Chapter 5, the Brillouin scattering of light in the WGMs by the Kittel mode was then experimentally investigated using a tapered optical nanofiber. The Brillouin scattering showed the unique features of the nonreciprocity and the Stokes/anti-Stokes

scattering asymmetry, which are the consequences of the spin and the orbital angular momentum conservation. The dependence of the signal strength on the frequency of the input laser was investigated and the spectral shift by the Kittel-mode frequency for the two input polarizations was observed, which can also be explained by the theory. The quantitative agreement with the theory was obtained by additionally taking into account the transition strengths for the two circular polarizations and the suppression of the scattering with the outer polarization component. Switching to the prism coupling, we further investigated the Brillouin scattering of the WGM light by the Walker modes in Chapter 6. The coupling among the Walker modes resulted in the rich behavior such as the significant enhancement of the Brillouin scattering in the coupling region for some modes. The dependence of the Brillouin scattering strength by the Kittel mode on the magnetic field was observed and the resonant enhancement by the WGM was realized.

In Sec. 5.6, the microwave-to-optical photon conversion efficiency through the Kittel mode was evaluated and the possible improvements were considered. However, the unity efficiency cannot be achieved even by using the thin YIG disk resonator with absorption-limited quality factor of the WGMs. To further enhance the conversion efficiency, it will be interesting to replace the Kittel mode by other higher-order Walker mode. It was seen in Figs. 6.6 and 6.8 (Sec. 6.3) that some Walker modes such as the $(4, 2, 0)$ mode gives the larger Brillouin scattering strengths than that of the Kittel mode. This is thought to be resulting from an order-of-magnitude larger quality factor of those modes and the mixing of the orbital angular momenta due to the coupling among modes. Another possible reason is inferred from the expression of Eq. 4.14, that is, the optomagnonical coupling coefficient $g^{(\text{theory})}$ is inversely proportional to the square root of the volume of the Walker mode.[1] For the general Walker modes with vanishing mode profile at the center (see Fig. 3.2), the effective mode volume is smaller than the sample volume, so that the coupling coefficient gains another factor. Since the mode profile is also affected by the coupling among Walker modes, it will be of certain interest to systematically study the influence of the inhomogeneity of the magnetic field on the Walker mode spectra and the Brillouin scattering strengths,

---

[1]For the Kittel mode, the mode profile is uniform and the volume of the mode coincides with the volume of the sample.

in the scope of the magnon engineering and the accompanying enhancement of the Brillouin scattering.

Another possibility is the use of the surface modes of the spin wave (see e.g. [49]), which have significantly smaller mode volumes compared to the bulk spin wave modes. For simplicity, we assume that the mode volume of the surface spin wave mode is comparable to that of the WGMs[2], namely the spatial mode matching between the optical and spin wave mode is maximized. In such a situation, a naive estimation shows that the mode volume of the surface mode is roughly $2\,000$ times smaller than the sample volume. This results in the enhancement of the Brillouin scattering strength by that factor since the scattering strength is proportional to $(g^{(\mathrm{theory})})^2 \propto 1/V_{\mathrm{eff}}$ where V_{eff} denotes the effective mode volume of the surface mode. If the surface spin wave is considered, its wavevector can be comparable to the optical wavevector, or the orbital angular momentum. The Brillouin scattering will manifest itself as the backscattering of the WGMs when the orbital angular momentum of the surface wave roughly doubles that of the WGMs, as mentioned in the Appendix A.

The system of the cavity optomagnonics that we investigated in this dissertation serves as a novel method to manipulate the macroscopic spin excitations by optical means and may potentially provide the strong coupling between light and magnons. During the time line of our research, we realized that Yale and Cambridge groups also investigated the optomagnonic systems along the same line [42, 56, 57]. Together with those, our work also stimulated the theoretical works [58, 59], which aim at the strong coupling between light and the Kittel mode. Exploring further into this system will find interesting applications in between quantum optics and spintronics, such as the efficient optical reading and writing of the spin current via a ferromagnetic material and the construction of an optically-mediated network of spintronics devices.

---

[2]Here the dimension of the WGM in a 1 mm-diameter sphere is assumed to be a prolate torus with the major radius of 500 μm. The elliptic cross-section assumes its "major" and "minor" radii of 10 μm and 3 μm, respectively.

Appendix A

Treatment of polarization components of WGMs in Brillouin scattering

In Chapter 4, the analysis of the Brillouin scattering of light in WGM by Walker modes is done in the way that both the WGMs and the Walker modes are expressed as operators in the second quantized form. Here, however, we introduce a slightly different expression of them, that is, the Walker-mode magnon is still an operator while the WGM photon is represented by state vector. Since the light in WGMs is characterized by its orbital and spin angular momenta as done in the Chapter 2, we adopt an uncommon but comprehensive notation for the WGM photon which is written as $|m, \tilde{\sigma}\rangle$. In this expression the first and the second indices stand respectively for the orbital and the spin angular momentum states. As we saw in the Secs. 2.2 and 4.2, the inner and outer polarization components always coexist with the different "centers of gravity" (see Fig. 2.6), so that the TM WGM photon $|\text{TM}_{\text{CW}}^m\rangle$, in CW orbit with mode index m for simplicity, possesses the $\tilde{\sigma}^+$-polarized component in the inner region and $\tilde{\sigma}^-$-polarized one in the outer region. This situation is summarized in the following form:

$$|\text{TM}_{\text{CW}}^m\rangle = \sqrt{F_{\text{in}}(r)}|m-1, \tilde{\sigma}^+\rangle + \sqrt{F_{\text{out}}(r)}|m+1, \tilde{\sigma}^-\rangle \qquad \text{(A.1)}$$
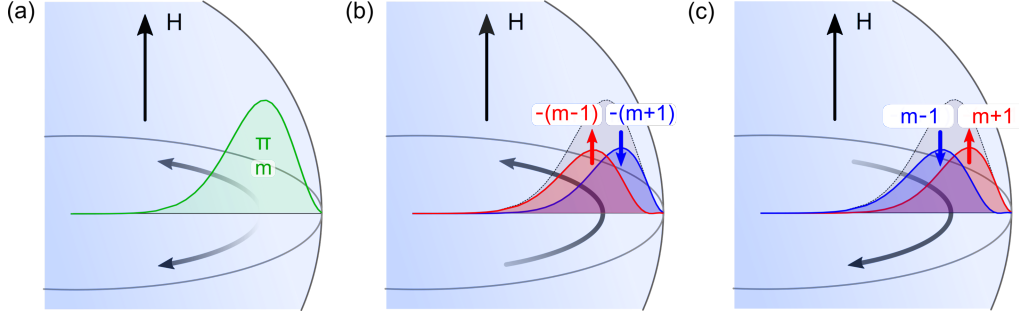
93

Figure A.1: Spin and orbital angular momenta of the WGMs. (a) The TE mode has π-polarized component every where regardless of the circulation direction. (b), (c) The TM mode is the superposition of $\tilde{\sigma}^{+}$- and $\tilde{\sigma}^{-}$-polarized components, which have different "centers of gravity" in the radial direction. Note that for the WGM in the (b) CCW and the (c) CW orbits, the spin and the orbital angular momenta of the inner and outer components are reversed.

where the fact is used that the orbital angular momenta for the inner and outer polarizations[1] are different from each other and $F_{\text{in}}(r)$ and $F_{\text{out}}(r)$ are the intensity distributions for the inner and outer components. For the WGM photon in the CCW orbit $|\text{TM}_{\text{CCW}}^{m}\rangle$, the orbital and spin angular momenta are both inverted so that

$$|\text{TM}_{\text{CCW}}^{m}\rangle = \sqrt{F_{\text{in}}(r)}|-(m-1),\tilde{\sigma}^{-}\rangle + \sqrt{F_{\text{out}}(r)}|-(m+1),\tilde{\sigma}^{+}\rangle \qquad (\text{A.2})$$

The TE mode with the mode index m is π-polarized everywhere with the orbital angular momentum of m:

$$|\text{TE}_{\text{CW}}^{m}\rangle = \sqrt{F_0(r)}|m,\pi\rangle \qquad (\text{A.3})$$

$$|\text{TE}_{\text{CCW}}^{m}\rangle = \sqrt{F_0(r)}|-m,\pi\rangle \qquad (\text{A.4})$$

where $F_0(r)$ denotes the total intensity distribution. The situations of TE and TM WGMs are summarized in Fig. A.1.

Next, we consider the magnon operator b for the Walker mode. The Brillouin scattering process can be interpreted as the one that the orbital and spin angular momenta of the WGM photon are changed by the magnon (see Chapter 4). Therefore the magnon operator of the walker mode with orbital angular momentum m is

---

[1]Here the sign of the orbital angular momentum is defined to be positive for CW WGM.

supposed to be written in the form

$$b_m = b_0(r)(L^+)^m \tilde{s}^+ \quad \text{or} \quad b^\dagger = b_0^*(r)(L^-)^m \tilde{s}^-. \tag{A.5}$$

Here the $L^\pm$ are the raising and lowering operators of the orbital angular momentum in a standard sense. The spin raising and lowering operators $\tilde{s}^\pm$ are defined so that the π-polarized state is operated to result in $\tilde{\sigma}^\pm$-polarized states, respectively. Above expression means that the creation (annihilation) of a magnon removes (adds) the orbital angular momentum of m from (to) the WGM photon, with accompanied transfer of the spin angular momentum. In the Hamiltonian, the magnon operator appears in the form of $b_{m_{\text{mag}}} + b_{m_{\text{mag}}}^\dagger$. Thus the straightforward calculation of terms such as $\langle \text{TE}_{\text{CW}}^{m_{\text{TE}}} | (b_{m_{\text{mag}}} + b_{m_{\text{mag}}}^\dagger) | \text{TM}_{\text{CW}}^{m_{\text{TM}}} \rangle$ give us the information about which process is relevant in the Brillouin scattering. Let us calculate this for instance. The first term yields, with the aid of Eqs. (A.1) and (A.3),

$$\langle \text{TE}_{\text{CW}}^{m_{\text{TE}}} | b_{m_{\text{mag}}} | \text{TM}_{\text{CW}}^{m_{\text{TM}}} \rangle$$
$$= \int dr b_0(r) \langle \text{TE}_{\text{CW}}^{m_{\text{TE}}} | \left[\sqrt{F_{\text{in}}(r)} (L^+)^{m_{\text{mag}}} \tilde{s}^+ | m_{\text{TM}} - 1, \tilde{\sigma}^+ \rangle \right.$$
$$\left. + \sqrt{F_{\text{out}}(r)} (L^+)^{m_{\text{mag}}} \tilde{s}^+ | m_{\text{TM}} + 1, \tilde{\sigma}^- \rangle \right]$$
$$= \int dr b_0(r) \sqrt{F_{\text{out}}(r)} \langle \text{TE}_{\text{CW}}^{m_{\text{TE}}} | m_{\text{TM}} + m_{\text{mag}} + 1, \pi \rangle$$
$$= \int dr b_0(r) \sqrt{F_{\text{out}}(r) F_0^*(r)} \langle m_{\text{TE}}, \pi | m_{\text{TM}} + m_{\text{mag}} + 1, \pi \rangle$$
$$= \int dr b_0(r) \sqrt{F_{\text{out}}(r) F_0^*(r)} \delta_{m_{\text{TE}} - (m_{\text{TM}} + 1) - m_{\text{mag}}, 0}$$
$$\equiv \eta_{\text{out}} \delta_{m_{\text{TE}} - (m_{\text{TM}} + 1) - m_{\text{mag}}, 0}.$$

The coefficients arising in the angular momentum operations are omitted here, since it is of no importance in the present analysis. The factor η_{out} stands for the integral in the radial direction[2]

$$\eta_{\text{out}} \equiv \int dr b_0(r) \sqrt{F_{\text{out}}(r) F_0^*(r)}.$$

---

[2]We here assume the fundamental modes of WGMs to be involved in the Brillouin scattering, so that the θ-dependence, which is expressed by the associated Legendre polynomial, just gives a factor by the θ-integral.

The second term can be evaluated in just the same way leading to

$$\langle \text{TE}_{\text{CW}}^{m_{\text{TE}}} | b_{m_{\text{mag}}}^{\dagger} | \text{TM}_{\text{CW}}^{m_{\text{TM}}} \rangle$$

$$= \int dr b_0^*(r) \langle \text{TE}_{\text{CW}}^{m_{\text{TE}}} | \left[\sqrt{F_{\text{in}}(r)} (L^-)^{m_{\text{mag}}} \tilde{s}^- | m_{\text{TM}} - 1, \tilde{\sigma}^+ \rangle \right.$$

$$\left. + \sqrt{F_{\text{out}}(r)} (L^-)^{m_{\text{mag}}} \tilde{s}^- | m_{\text{TM}} + 1, \tilde{\sigma}^- \rangle \right]$$

$$= \int dr b_0^*(r) \sqrt{F_{\text{in}}(r)} \langle \text{TE}_{\text{CW}}^{m_{\text{TE}}} | m_{\text{TM}} - m_{\text{mag}} - 1, \pi \rangle$$

$$= \int dr b_0^*(r) \sqrt{F_{\text{in}}(r) F_0^*(r)} \langle m_{\text{TE}}, \pi | m_{\text{TM}} - m_{\text{mag}} - 1, \pi \rangle$$

$$= \int dr b_0^*(r) \sqrt{F_{\text{in}}(r) F_0^*(r)} \delta_{m_{\text{TE}} - (m_{\text{TM}} - 1) + m_{\text{mag}}, 0}$$

$$\equiv \eta_{\text{in}}^* \delta_{m_{\text{TE}} - (m_{\text{TM}} - 1) + m_{\text{mag}}, 0}.$$

where the factor η_{in}^* are defined as

$$\eta_{\text{in}}^* \equiv \int dr b_0^*(r) \sqrt{F_{\text{in}}(r) F_0^*(r)}.$$

Thus, one of the matrix elements of the interaction Hamiltonian $\langle \text{TE}_{\text{CW}}^{m_{\text{TE}}} | \mathcal{H}_{\text{int}} | \text{TM}_{\text{CW}}^{m_{\text{TM}}} \rangle$ is obtained here as being proportional to the sum of above two results. It can be seen that the elements such as $\langle \text{TE}_{\text{CW}}^{m_{\text{TE}}} | \mathcal{H}_{\text{int}} | \text{TE}_{\text{CW}}^{m_{\text{TE}}'} \rangle$ and $\langle \text{TM}_{\text{CW}}^{m_{\text{TM}}} | \mathcal{H}_{\text{int}} | \text{TM}_{\text{CW}}^{m_{\text{TM}}'} \rangle$ vanish due to the spin angular momentum conservation. The only surviving terms are $\langle \text{TE}_{\text{CW}}^{m_{\text{TE}}} | \mathcal{H}_{\text{int}} | \text{TM}_{\text{CW}}^{m_{\text{TM}}} \rangle$ and $\langle \text{TM}_{\text{CW}}^{m_{\text{TM}}} | \mathcal{H}_{\text{int}} | \text{TE}_{\text{CW}}^{m_{\text{TE}}} \rangle = (\langle \text{TE}_{\text{CW}}^{m_{\text{TE}}} | \mathcal{H}_{\text{int}} | \text{TM}_{\text{CW}}^{m_{\text{TM}}} \rangle)^*$, which are summarized as

$$A := (\eta_{\text{out}} + \eta_{\text{out}}^*) \delta_{m_{\text{TE}} - (m_{\text{TM}} + 1) - m_{\text{mag}}, 0} + (\eta_{\text{in}} + \eta_{\text{in}}^*) \delta_{m_{\text{TE}} - (m_{\text{TM}} - 1) + m_{\text{mag}}, 0}$$

The first (second) term results from the outer (inner) polarization component of the CW WGM. In the Kronecker's delta we see that the orbital angular momentum conservation for the outer and inner polarizations are derived again. If the time dependences are explicitly shown, the energy conservation $\omega_{\text{TE}} - \omega_{\text{TM}} \mp \omega_{\text{mag}} = 0$ are respectively obtained for the outer and inner polarizations. According to the Fermi's golden rule, the scattering rate is described by the product of A^2 with the delta function indicating the energy conservation and the density of states of the output state, namely the output WGM. Thanks to the presence of the Kronecker's delta, the factor A^2 reads the sum of the square of each term in A. Therefore, the contributions of the inner and outer components can be completely separately evaluated from the

96

energy and orbital angular momentum conservation for each case, where the orbital angular momentum conservation actually determines the relevant output WGM in the process as analyzed in Secs. 5.4 and 6.3.1.

Above consideration does not deal with the process interconnecting the CW and the CCW WGM photons, such as $\langle \mathrm{TE}_{\mathrm{CCW}}^{m_{\mathrm{TE}}} | \mathcal{H}_{\mathrm{int}} | \mathrm{TM}_{\mathrm{CW}}^{m_{\mathrm{TM}}} \rangle$. After some calculations we see that this kind of processes occur when the orbital angular momentum of the magnon is roughly twice the one of the WGM photon, which means that the WGM photon is backscattered by the magnon. Therefore such a kind of process is negligible in our analysis with the magnetostatic modes where the orbital angular momenta are small. However, by using the surface spin wave [49] it becomes feasible. This may result in a brand-new physics and the novel spintronic or magnetic devices in the future.

Bibliography

[1] S. Haroche. "Nobel Lecture: Controlling photons in a box and exploring the quantum to classical boundary" *Rev. Mod. Phys.* **85**, 1083 (2013).

[2] R. Miller, T. E. Northup, K. M. Birnbaum, A. Boca, A. D. Boozer, and H. J. Kimble. "Trapped atoms in cavity QED: coupling quantized light and matter" *J. Phys. B: Mol. Opt. Phys.* **38**(9), S551 (2005).

[3] A. A. Clerk, M. H. Devoret, S. M. Girvin, F. Marquardt, and R. J. Scheolkopf. "Introduction to quantum noise, measurement, and amplification" *Rev. Mod. Phys.* **82**, 1155 (2010).

[4] M. Aspelmeyer, T. J. Kippenberg, and F. Marquardt. "Cavity optomechanics" *Rev. Mod. Phys.* **86**, 1391 (2014).

[5] Y. Tabuchi, S. Ishino, A. Noguchi, T. Ishikawa, R. Yamazaki, K. Usami, and Y. Nakamura. "Coherent coupling between a ferromagnetic magnon and a superconducting qubit" *Science* **349**, 405 (2015).

[6] T. Satoh , Y. Terui , R. Moriya , B. A. Ivanov , K. Ando , E. Saitoh , T. Shimura and K. Kuroda. "Directional control of spin-wave emission by spatially shaped light" *Nat. Photon.* **6**, 662 (2012).

[7] T. Satoh, R. Iida, T. Higuchi, M. Fiebig, and T. Shimura. "Writing and reading of an arbitrary optical polarization state in an antiferromagnet" *Nat. Photon.* **9**, 25 (2015).

[8] R. Hisatomi, A. Osada, Y. Tabuchi, T. Ishikawa, A. Noguchi, R. Yamazaki, K, Usami, and Y. Nakamura, "Bidirectional conversion between microwave and light via ferromagnetic magnons" *Phys. Rev. B* **93**, 174427 (2016).

[9] S. O. Demokritov, V. E. Demidov, O. Dzyapko, G. A. Melkov, A. A. Serga, B. Hillebrands, and A. N. Slavin. "Bose-Einstein condensation of quasi-equilibrium magnons at room temperature under pumping" *Nature* **443**, 430 (2006).

[10] Y. Tserkovnyak, A. Brataas, and G. E. Bauer. "Enhanced Gilbert Damping in Thin Ferromagnetic Films" *Phys. Rev. Lett.* **88**, 117601 (2002).

[11] A. L. Schawlow and C. H. Townes. "Infrared and Optical Masers" *Phys. Rev.* **112**, 1940 (1958).

[12] T. H. Maiman. "Stimulated Optical Radiation in Ruby" *Nature* **187**, 493 (1960).

[13] D. L. Mills. "*Nonlinear Optics - Basic Concepts (Second, Enlarged Edition)*" (Springer-Verlag Berlin, Heidelberg, 1998).

[14] K. Hennessy, A. Badolato, M. Winger, D.=Gerace, M. Atatüre, S. Gulde, S. Fält, E. L. Hu, and A. Imamoglu. "Vacuum Rabi Spectra of a Single Quantum Emitter" *Phys. Rev. Lett.* **114**, 143603 (2015).

[15] Y. Nakamura, Y. A. Pashkin, and J. S. Tsai. "Coherent control of macroscopic quantum states in a single-Cooper-pair box" *Nature* **398**, 786 (1999).

[16] A. Blais, R.-S. Huang, A. Wallraff, S. M. Girvin and R. J. Schoelkopf. "Cavity quantum electrodynamics for superconducting electrical circuits: An architechture for quantum computation" *Phys. Rev. A* **69**, 063230 (2004).

[17] Eds. M. Aspelmeyer, T. J. Kippenberg, and F. Marquardt. "*Cavity Optomechanics - Nano- and Micromechanical Resonators Interacting with Light*" (Springer-Verlag Berlin, Heidelberg, 2014).

[18] J. Chan, T. P. Mayer Alegre, A. H. Safavi-Naeini, J. T. Hill, A. Krause, S. Gröblacher, M. Aspelmeyer and O. Painter. "Laser cooling of a nano mechanical oscillator into its quantum ground state" *Nature* **478**, 89 (2011).

[19] J. D. Teufel, T. Donner, D. Li, J. W. Harlow, M. S. Allman, K. Cicak, A. J. Sirois, J. D. Whittaker, K. W. Lehnert, and R. W. Simmonds. "Sideband cooling of micro mechanical motion to the quantum ground state" *Nature* **475**, 359 (2011).

[20] C. F. Bohren, and D. R. Huffman. "*Absorption and Scattering of Light by Small Particles*" (WILEY-VCH, Weinheim, 1998).

[21] M. Oxborrow. "Tracable 2-D finite-element simulation of the whispering-gallery modes of axisymmtric electromagnetic resonators" *IEEE TRANSACTIONS ON MICROWAVE THEORY AND TECHNIQUES* **55** 1209 (2007).

[22] I. S. Grudinin and N. Yu. "Finite element modeling of coupled optical micro disk resonators for displacement sensing" *J. Otp. Soc. Am. B* **29** 3010 (2012).

[23] S. Schiller and R. L. Byer. "High-resolution spectroscopy of whispering gallery modes in large dielectric spheres" *Opt. Lett.* **16**, 1138 (1991).

[24] C. C. Lam, P. T. Leung, and K. Young. "Explicit asymptotic formulas for the positions, widths, and strengths of resonances in Mie scattering" *J. Opt. Soc. Am. B* **9**, 1585 (1992).

[25] S. Schiller. "Asymptotic expansion of morphological resonance frequencies in Mie scattering" *Appl. Opt.* **32**, 2181 (1993).

[26] D. L. Wood and J. P. Remeika. "Effect of Impurities on the Optical Properties of Yttrium Iron Garnet" *J. Appl. Phys.* **38**, 1038 (1967).

[27] L. Allen, M. W. Beijersbergen, R. J. C. Spreeuw, and J. P. Woerdman. "Orbital angular momentum of light and the transformation of Laguerre-Gaussian laser modes" *Phys. Rev. A* **45**, 8185 (1992).

[28] S. J. van Enk and G. Nienhuis. "Spin and Orbital Angular Momentum of Photons" *EPL* **25**, 497 (1994).

[29] R. P. Cameron, F. C. Speirits, C. R. Gilson, L. Allen, and S. M. Barnett. "The azimuthal component of Poynting's vector and the angular momentum of light" *J. Opt.* **17**, 125610 (2015).

[30] R. Y. Chiao, and Y.-S. Wu. "Manifestation of Berry's Topological Phase for the Photon" *Phys. Rev. Lett.* **57**, 933 (1986).

[31] M. Onoda, S. Murakami, and N. Nagaosa. "Hall Effect of Light" *Phys. Rev. Lett.* **93**, 083901 (2004).

[32] K. Y. Bliokh, D. Smirnova, and F. Nori. "Quantum spin Hall effect of light" Science **348**, 6242 (2015).

[33] K. Y. Bliokh, and V. D. Freilikher. "Topological spin transport of photons: Magnetic monopole gauge field in Maxwell's equations and polarization splitting of rays in periodically inhomogeneous media" *Phys. Rev. B* **72**, 035108 (2005).

[34] K. Y. Bliokh, M. A. Alonso, E. A. Ostrovskaya, and A. Aiello. "Angular momenta and spin-orbit interaction of non paraxial light in free space" *Phys. Rev. A* **82**, 063825 (2010).

[35] A. Berard, and H. Mohrbach. "Spin Hall effect and Berry phase of spinning particles" *Phys. Lett. A* **352**, 190 (2006).

[36] K. Vahala. "Optical microcavities" *Nature* **424**, 839 (2003).

[37] T. J. Kippenberg. "Nonlinear Optics in Ultra-high-Q Whispering-Gallery Optical Microwavities" Ph.D thesis in California Institute of Technology (2004).

[38] V. B. Braginsky, M. L. Gorodetsky, and V. S. Ilchenko. "Quality-factor and nonlinear properties of optical whispering-gallery modes" *Phys. Lett. A* **137**, 393 (1989).

[39] T. Aoki. "Fabrication of Ultralow-Loss Tapered Optical Fibers and Microtoroidal Resonators" *Jpn. J. Appl. Phys.* **49**, 118001 (2010).

[40] R. V. Pisarev, I. G. Sinii, N. N. Kolpakova, Y. M. Yakovlev. "Magnetic Birefringence of Light in Iron Garnets" *Sov. Phys. JETP* **33**, 1175 (1971).

[41] D. F. Walls and G. J. Milburn. "*Quantum Optics*" (Springer-Verlag, Berlin Heidelberg, 2008).

[42] X. Zhang, N. Zhu, C.-L. Zou, and H. X. Tang. "Optomagnonic Whispering Gallery Microresonators" *Phys. Rev. Lett.* **117**, 123605 (2016).

[43] L. R. Walker. "Magnetostatic Modes in Ferromagnetic Resonance" *Phys. Rev.* **105**, 390 (1957).

[44] P. Fletcher, I. H. Solt, and R. Bell. "Identification of the Magnetotatic Modes of Ferromagnetic Resonant Spheres" *Phys. Rev.* **114**, 739 (1959).

[45] P. C. Fletcher and R. O. Bell. "Ferrimagnetic Resonance Modes in Spheres" *J. Appl. Phys.* **30**, 687 (1959).

[46] Y. Tabuchi, S. Ishino, T. Ishikawa, R. Yamazaki, K. Usami, and Y. Nakamura. "Hybridizing Ferromagnetic Magnons and Microwave Photons in the Quantum Limit" *Phys. Rev. Lett.* **113**, 083603 (2014).

[47] P. Yan, A. Kamra, Y. Cao, G. E. Bauer. "Angulat and linear momentum of excited ferromagnets" *Phys. Rev. B* **88**, 144413 (2013).

[48] A. G. Gurevich and G. A. Melkov. "*Magnetization Oscillations and Waves*" (CRC Press, Boca Raton, Florida, 1996).

[49] D. D. Stancil and A. Prabhakar. "*Spin Waves: Theory and Applications*" (Springer, 2009).

[50] D. C. Meeker. Finite Element Method Magnetics, Verison 4.2 (12Jan2016 Build), http://www.femm.info

[51] K. Momma and F. Izumi. "An integrated three-dimensional visualization system VESTA using wxWidgets" *Comm. Crystallogr. Comput. IUCr Newsl* **7**, 106 (2006).

[52] A. K. Zvezdin and V. A. Kotov. "*Modern Magnetooptics and Magnetooptical Materials*" (CRC Press, 1997).

[53] Eds. S. Sugano and N. Kojima. "*Magneto-Optics*", (Springer Series in Solid-State Sciences, 1999).

[54] U. Fano. "Effects of Configuration Interaction in Intensities and Phase Shifts" *Phys. Rev.* **124**, 1866 (1961).

[55] Y. S. Joe, A. M. Satanin, and C. S. Kim. "Classical analogy of Fano resonances" *Phys. Scr.* **74**, 259 (2006).

[56] J. A. Haigh, S. Langenfeld, N. J. Lambert, J. J. Baumberg, A. J. Ramsay, A. Nunnenkamp, and A. J. Ferguson. "Magneto-optical coupling in whispering-gallery-mode resonators" *Phys. Rev. A* **92**, 063845 (2015).

[57] J. A. Haigh, A. Nunnenkamp, A. J. Ramsay, and A. J. Ferguson. "Triple-Resonant Brillouin Light Scattering in Magneto-Optical Cavities" *Phys. Rev. Lett.* **117**, 133602 (2016).

[58] S. V. Kusminskiy, H. X. Tang, and F. Marquardt. "Coupled spin-light dynamics in cavity optomagnonics" *Phys. Rev. A* **94**, 033821 (2016).

[59] T. Liu, X. Zhang, H. X. Tang, and M. E. Flatte "Optomagnonics in magnetic solids" *Phys. Rev. B* **94**, 060405(R) (2016).

ACKNOWLEDGEMENTS